THERMAL SHOCK AND THERMAL STRESS PREDICTION ON A HIGHLY LOADED TURBINE NOZZLE GUIDE VANE BASED ON AN AERODYNAMIC AND THERMAL ANALYSIS

by

Krzysztof Kulik

Dissertation submitted in fulfilment of the academic requirements for the degree of Master of Science in Mechanical Engineering.

University of KwaZulu-Natal

Durban

March 2005

ABSTRACT

A 2-D plain strain CFD/FEM model to simulate thermal shocks and stresses in a turbine blade has been set up using the commercially available software FLUENT and NASTRAN. The model was validated against the experimental data of Bohn et. al. and used to simulate real test cases. The steady state numerical model was set up for a single Mark II nozzle guide vane using the correct boundary conditions to resolve the flow field. A combined laminar and turbulent model was developed in FLUENT that was used to highly accurately predict the pressure, temperature and heat transfer coefficient distribution on the blade surface as well as the temperature distribution on the cooling holes inside the blade. The resulting temperature profiles on the blade and cooling holes were used as boundary conditions for the FEM analysis to resolve the internal temperature and stress profiles.

The pressure, temperature and heat transfer distribution on the blade, from FLUENT, were compared to those from Bohn et. al. The predicted pressure distribution was exact with the experimental results and the predicted temperature distribution had an average over-prediction of 1.4 % on both the pressure and suction side. The internal temperature profile predicted by NASTRAN was correctly predicted with an average over-prediction of 2 %. The stress contours were accurately predicted with the stress magnitude varying by 17 % to that of Bohn et. al. The reason for the difference between the MSC.NASTRAN and Bohn et. al. stress results is believed to be purely solver related. Bohn et al. used a FEM package called MSC.MARC/Mentat.

With the steady state model validated, transient test cases were simulated that represent typical operational data. The mission profile was obtained for the T-56 engine found on the C130 cargo plane. The model was used to simulate the test case where the turbine inlet temperature (TIT) varied with time. The simulation results showed that stress was proportional to TIT, where changes in the TIT were seen later in the stress curve, due to conduction in the blade. Steep TIT changes, such as shock loads affected stress later than gentler TIT changes. Thus, the FLUENT / NASTRAN model was successfully validated, and used to simulate a flight mission profile. The goal to calculate quality unsteady stress profiles was achieved and forms the boundary conditions for thermal fatigue calculations.

PREFACE

The author hereby states that this entire thesis, unless specifically indicated to the contrary, is his own work, and has not been submitted in part or in whole to any other University. This dissertation records the work completed by the author at the Department of Mechanical Engineering at the University of Natal between April 2003 and December 2003 and, at the Department of Mechanical Engineering at the University of KwaZulu Natal between January 2004 and December 2004. This project was supervised by Prof. S Govender and forms part of an ongoing study in the field of turbine blade heat transfer and thermal stress prediction.

"Only two things are infinite, the universe and human stupidity, and I'm not sure about the former."

- Albert Einstein

ACKNOWLEDGEMENTS

The work that I have been fortunate enough to spend the last 21 months on would not have been possible without a great number of people, to all of whom I am very grateful.

Firstly, I would like to thank my supervisor Professor S. Govender, for his friendly supervision and, along with Professor J. Visser for giving me this opportunity to perform research in the field of Gas Turbine Technology.

Danie de Kock at the University of Pretoria for his assistance with many dilemmas encountered with the simulations.

Montresor Morris at the University of Pretoria for the P-4 that made convergence a lot quicker.

Hennie van Rensburg, Pieter Ferreira and the rest of the ARMSCOR crew for their generous financial assistance.

Graham, Vaughan and Justin for the distractions and detour (especially indoor office cricket) from work at times when we all needed a break.

Damien, Steve (Kla-Man) and Donavan (a.k.a The Chinarators), Nick, Lj, Michael, Serguei, Colin and Ross for all the friendship and jols, wah!

My parents and sister for all their love and support over the past two years, and for putting up with and understanding all my 'issues' caused by work stress.

Yvette, for her constant love, support and encouragement. Baie dankie my liefie.

TABLE OF CONTENTS

LIST OF FIGURES

CHAPTER 5

CHAPTER 6

APPENDIX A

APPENDIX E

APPENDIX F

APPENDIX G

APPENDIX H

APPENDIX I

LIST OF TABLES

NOMENCLATURE

Symbols

a	GAMBIT meshing parameter – first cell height
GR	GAMBIT meshing parameter – cell growth rate
Rows	GAMBIT meshing parameter – number of rows inside the boundary layer mesh
T	Temperature
t	time
x/L	Dimensionless axial chord length
s/arc	Dimensionless circumferential chord length
x	x-coordinate direction
y	y-coordinate direction
z	z-coordinate direction
y^+	Dimensionless wall distance
Re	Reynold's number
Re_x	Reynold's number based on axial chord
Re_y	Turbulent Reynold's number
M	Mach number
Mexit	Exit Mach number
Cp	Specific heat coefficient
k	Turbulent kinetic energy
k	Thermal conductivity
P	Pressure
E	Young's Modulus
Tu	Turbulence intensity
T_u	Average vane surface temperature

Greek Symbols

ν	Poisson's ratio
ρ	Density
σ	Stress
γ	Specific heat ratio
γ	Thermal diffusivity coefficient

μ	Viscosity
ε	Strain
α	Volumetric Expansion Coefficient

Acronyms

AMG	Algebraic Multigrid Method
ASME	The American Society of Mechanical Engineers
CFD	Computational Fluid Dynamics
CMD	Computational Mesh Dynamics
CSD	Computational Structural Dynamics
CSIR	Council for Scientific and Industrial Research
FACE	Fatigue and Air Combat Evaluation
FAS	Full Approximation Storage
FEM	Finite Element Analysis
GPA	Gas Path Analysis
GSP	Gas Turbine Simulation Program
HRN	High Reynold's Number
LER	Leading Edge Radius
NGV	Nozzle Guide Vane
PS	Pressure Side
RANS	Reynold's Averaged Navier-Stokes
SAAF	South African Air Force
SS	Suction Side
TIT	Turbine Inlet Temperature
TSR	Thermal Shock Resistance
UL	Updated Lagrangian

Subscripts

e	equivalent
x	x-coordinate direction
y	y-coordinate direction
z	z-coordinate direction
op	operating pressure

CHAPTER 1

INTRODUCTION

The first recorded evidence of jet propulsion was in approximately 100 BC. The Greek mathematician/inventor, Hero of Alexandria, invented a device called the aeolipile, shown in Figure 1.1. Hero mounted a sphere on top of a water kettle, a fire below the kettle converted the water into steam, and the gas travelled through the pipes to the sphere. Two L-shaped tubes on opposite sides of the sphere allowed the gas to escape, and in doing so, gave a thrust to the sphere that caused it to rotate.

Figure 1-1: Schematic of an aeolipile, reproduced from the About Inventors website.

In 1791, John Barber received the first patent for a basic turbine engine. Barber's design was planned to be used as a method of propelling a carriage. It incorporated many of the same elements of a modern gas turbine but used a reciprocating compressor. There are many more early examples of turbine engines designed by various inventors, but none were considered to be true gas turbines as they incorporated steam at some point in the process.

In 1930, Sir Frank Whittle an English aviation engineer and pilot patented a design for a gas turbine for jet propulsion. At the age of 22, Frank Whittle first thought to use a gas turbine engine to power an aircraft. Although Frank Whittle could not gain any financial support for the research, Whittle persisted on his own initiative and with private financial support began constructing the first engine in 1935. This engine, which had a single-stage centrifugal compressor coupled to a single-stage turbine, was successfully bench tested in 1937.

Whittle's engine, known as the W1, powered the aircraft known as Gloster E2, which made its first flight in 1941. This gas turbine powered aircraft reached a speed of just over 600 kilometres per hour and developed 1,100 pounds of thrust. Only sixty years later, aircrafts powered by gas turbine engines are flying at speeds exceeding 3,000 kilometres per hour and developing 35,000 pounds of thrust.

Figure 1.2 shows a detailed picture of a gas turbine engine highlighting the main building blocks of the engine and Figure 1.3 shows the schematic of the engine. The gas turbine engine operates on the principal of the Brayton cycle, where compressed air is mixed with fuel and burned in the combustion chamber under near-constant pressure. The resulting high temperature, high pressure gas is expanded through the turbine, forcing the turbine to rotate and power the compressor through the connecting shaft. The Brayton cycle describes the ideal performance of a gas turbine engine and, like any engine cycle, the higher the maximum temperature the higher the overall efficiency. Appendix A shows the derivation of the simple Brayton cycle.

The enormous growth in air travel and firm competition between engine manufactures have resulted in major contributions to the advances in gas turbine performance, that provide an ongoing need to improve power output, reliability and fuel efficiency. These current demands for an increase in higher performance, while still maintaining affordability and engine durability, can primarily be achieved through higher combustion temperatures.

The need for higher combustion temperatures is limited mainly by the first set of stator blades in the turbine, also known as nozzle guide vanes (NGV), which are directly downstream of the combustion chamber. At start-up, the turbine inlet temperature (TIT) is increased from ambient to anything above a thousand degrees Celsius. This causes a severe temperature increase in the blades and while the flight operation changes due to manoeuvring of the aircraft, so the TIT continually changes.

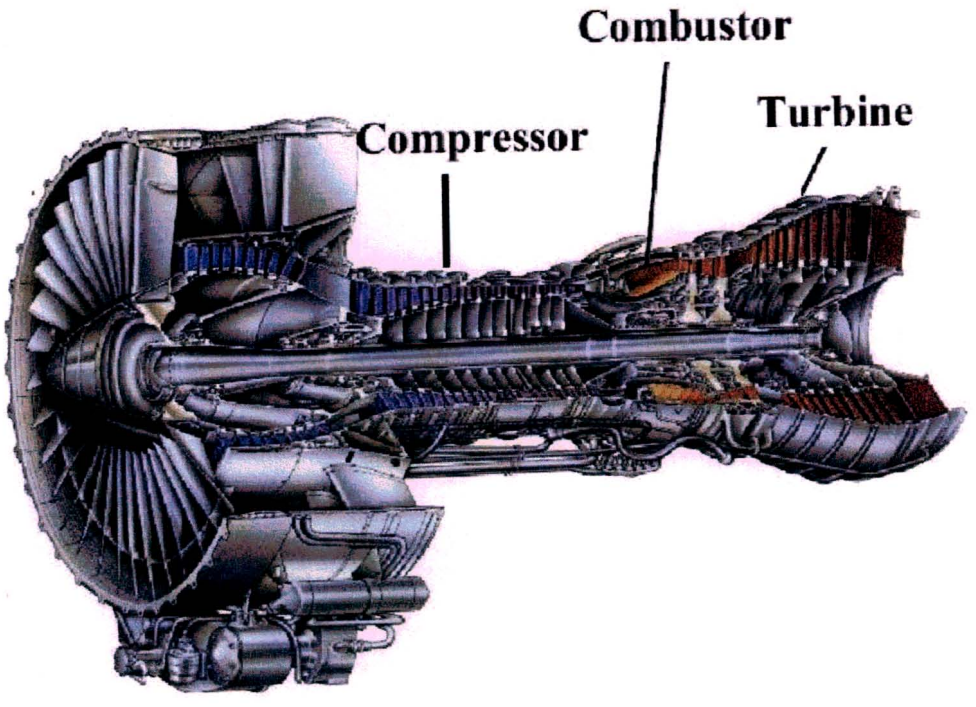

Figure 1-2: Layout of the components of a gas turbine engine.

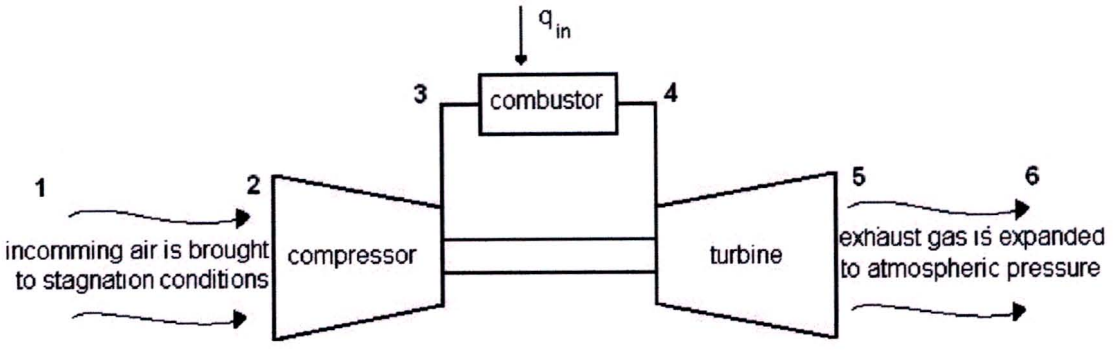

Figure 1-3: Schematic layout of a gas turbine engine

The harsh thermal conditions cause severe thermal stresses in the NGV and, due to the unsteady nature of the TIT, one can expect the thermal stresses within the blade to also be unsteady. This can cause the formation of thermal fatigue cracks and eventually result in structural failure of the blade. The ability to run a gas turbine engine at an increasingly high gas temperature has resulted from a combination of material improvements and the development of more sophisticated arrangements for internal and external cooling of the blades.

Metallurgical advances in materials have seen the development of alloys with higher melting points to allow for a higher TIT. Internally cooled blades use cold air that is bled from the compressor and flows through passages inside the blade, creating a temperature gradient within the blade to conduct the heat away from the surface. External or film cooling builds onto internal cooling where the cold air inside the blade is ejected into the hot gas stream from inside the blade. This creates a layer of cooler air around the blade.

Assessing the life and improving the thermal design of a blade play major roles in all fields where gas turbine engines are utilized. In the aircraft industry regular inspections are made while an aircraft is grounded, this leads to great undesirable expenses. If the mechanical life of a blade could be predicted then the frequency of inspections could be reduced. If one can quantify the thermal fatigue life of the blades in terms of TIT then monitoring the TIT will allow engine users to asses the extent of fatigue cracks without having to ground the aircraft. Thermal fatigue data can be obtained from experimentation or by thermal fatigue life calculations. Thermal fatigue calculations can only be accurate if the thermal stresses used in the calculations quantitatively represent the actual thermal stress that would be found in the blades.

Analysing the thermal design of a blade begins with understanding the complex flow field around the blade. Predicting highly accurately the blade surface heat load created by the hot gas stream moving over the blade is essential to predicting the corresponding thermal stresses inside the blade. The problems associated with predicting heat transfer to the blades is coupled with: turbine blade aerodynamics; free stream turbulence; boundary layer transition; separation and reattachment; shock waves and main flow acceleration and deceleration. These are just a few of the phenomena associated with the three-dimensional unsteady flow.

Numerical codes predicting the flow and heat transfer have been developed over the past 30 years, mainly due to the experimental community. It has advanced to the point where time resolved 3-D heat transfer data for vanes and blades are obtained routinely by those operating full rotating rigs. The quality of experimental data produced has been used to validate the numerical codes. This dissertation is aimed at developing a CFD model using a commercially available numerical code to resolve the flow field and heat load to the blade. Coupled to this is the finite element method (FEM) model that was developed using a commercially available numerical code to simulate thermal stresses in the turbine blade.

The aerodynamic analysis was performed using the code FLUENT, the CFD model was developed using the geometry of the stationary nozzle guide vane known as the Mark II. FLUENT was used to resolve the flow field and heat transfer to the blade. The data from the aerodynamic analysis was then used as the boundary conditions for the thermal analysis that was performed using the code NASTRAN. The code was used to solve the internal blade temperatures and the corresponding thermal stresses. Experimental data on the Mark II was available from literature and was used to validate the steady state aerodynamic and thermal analysis.

With the steady state model validated, transient test cases were simulated that represent typical operational data. The mission profile with TIT that varied with time was acquired for the T56 engine found on the C130 cargo plane. The maximum equivalent stress that occurred in the blade was plotted against time, together with the TIT profile for the cycle. The results of the transient analyses showed the behaviour of the stress as a result of the changing TIT. The resulting stress variation gives quality data, which can be used in thermal fatigue calculations to ultimately predict the mechanical life of a turbine blade.

CHAPTER 2

LITERATURE SURVEY

2.1 Introduction

With the vast amount of literature available on turbine blade heat transfer and related topics, finding the optimum starting point can prove to be a tricky task. The research discussed in this dissertation was supported by ARMSCOR, the results obtained from this research will be used for gas turbine maintenance and life assessment. The best starting point therefore was to examine the current research into gas turbine life models. This then also provides a platform from which to research the problem in a systematic manner and to narrow down the topics in order to focus primarily on the development of the computer model.

2.2 Overview of Lifing Models

Two very useful papers Ibrahim (2000) and Singh (1999), give an introduction to gas turbine life assessment and engine monitoring research. Ibrahim (2000) gives an overview into gas turbine engine failure prediction and emphasises that the underlying cause of gas turbine blade failure is often an aerodynamic phenomena. Singh (1999) gives a detailed outline of the gas turbine life assessment called Gas Path Analysis (GPA) that has been developed at Cranfield University in the United Kingdom.

Operating a propulsion gas turbine engine is extremely expensive, and the user aims to minimise the engine maintenance downtime and more importantly avoid catastrophic failure of any of the hot-gas-path components. Engine health monitoring and life assessment plays an important role in determining the degree of degradation and wear in an engine and assists users in strategically planning maintenance action. The strategy of GPA is to assess the condition of an engine and its components through dependant measurable parameters such as pressures and temperatures, and independent non-measurable parameters such as efficiencies, flow rate and thrust.

This kind of assessment is only possible if it is known, a prior, what effect the different kinds of degradation will have on the measurable and non-measurable parameters, not only for the entire

engine but also on a component level. Quantifying the effect of degradation in terms of measurable and non-measurable parameters within a component, (the turbine blades for example), is the first step. The analysis can then expand to the component and finally, the entire engine. A study performed by Tinga et. al. (2000) relates directly to the work in this dissertation. Tinga developed an analysis tool that predicts engine component (or part) life based on the analysis of engine performance.

2.2.1 Integrated Lifing Analysis for Gas Turbine Components

Tinga's model ranges from the measurement of operational engine data by the FACE system to ultimately predicting the life consumption of various components during the analysed mission. An overview of the sequence is given in Figure 2.1. Tinga's sequential model comprises of the following five tools:

- FACE - Fatigue and Air Combat Evaluation (FACE) system for monitoring flight and engine data;
- GSP - Gas Turbine Simulation Program (GSP) for calculating engine system performance data;
- CFD - Computational Fluid Dynamics (CFD) model for calculating the heat transfer to hot section components;
- FE - Finite Element (FE) model for calculating thermal and mechanical stress in hot section components;
- Lifing model - For deriving component life consumption data from the stress history data.

The model presented by Tinga offers a way to attempt to reduce maintenance costs and improve safety by applying usage monitoring to predict operational component condition and thereby facilitating on-condition required maintenance. Here after follows a description of the five tools that make up the model, of particular interest to this dissertation are the CFD and FE tools, as they correlate specifically to the research presented by the author.

2.2.1.1 FACE

The FACE system used to measure flight data consists of both on-board and ground-based hardware. Two electronic boxes are installed in the aircraft, the flight-monitoring unit and the data-recording unit. The ground-based hardware is relevant for maintenance purposes. The flight-monitoring unit is programmable and determines which signals are to be stored by the

data-recording unit. The relevant signals stored fully describe engine usage and include: fuel-flow to the gas generator and the afterburner, exhaust nozzle position and flight conditions such as Mach, altitude and air temperature. These parameters, as a function of time, are used as input conditions for the GSP model, which is the next tool in the sequence.

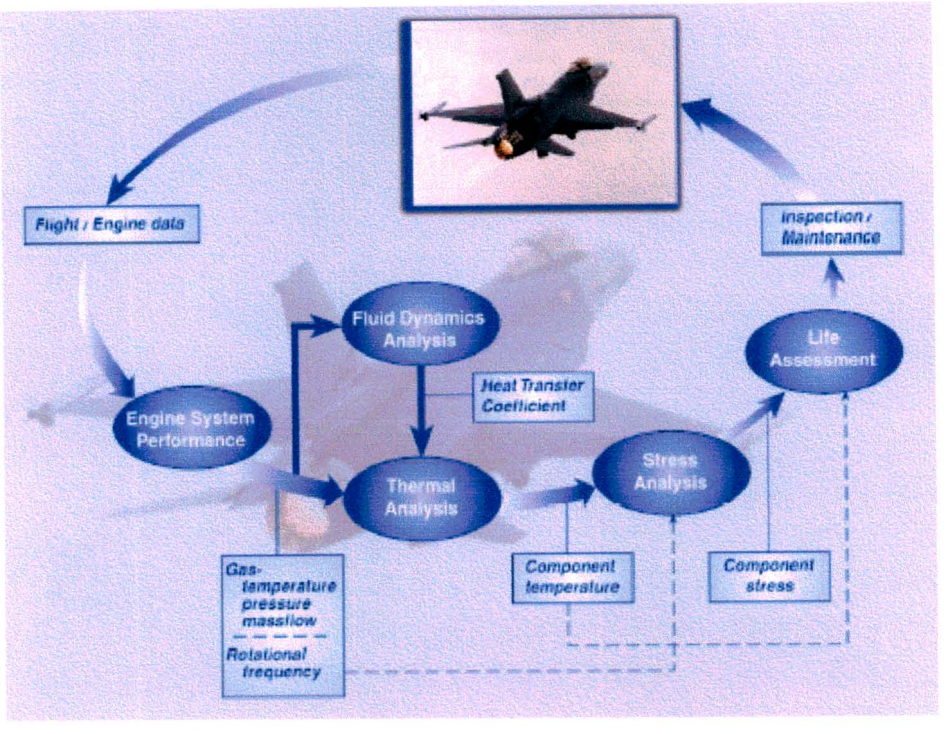

Figure 2.1: Overview of Tinga's integrated analysis tool, reproduced from Tinga et. al. (2000).

2.2.1.2 GSP

The GSP program is a tool for gas turbine engine performance analysis. This program enables both steady state and transient simulations for any kind of gas turbine configuration. A specific gas turbine configuration can be created by arranging different predefined components (like fans, compressors and combustors) in a configuration similar to the gas turbine type to be simulated.

The simulation is based on one-dimensional modelling of the processes in the different gas turbine components with thermodynamic relations and steady-state characteristics. The program calculates gas temperatures, pressures, velocities and composition at relevant engine stations, particularly where no measured data is available (such as the critical high pressure TIT). The entire engine transient can be calculated with an integrated step size small enough to accurately calculate the critical effects such as typical acceleration / deceleration temperature

transients in the hot section. The output data from GSP is used for further processing by the CFD and FE models.

2.2.1.3 CFD

The CFD model is used to accurately calculate the heat transfer from the hot gas stream to the component. For this calculation it is important to have detailed information on the geometry of both the flow channel and the different components that disturb the flow (such as vanes and blades). From the CFD analysis of the gas flow through the gas turbine, values for the heat transfer coefficients or the temperatures are obtained at specific locations in the component. The heat transfer coefficients and temperatures vary significantly along the flow path, due to variations in the flow. The results from the CFD analysis are used as input boundary conditions for the FE model.

2.2.1.4 FE

The FE model consists of two interrelated models - the thermal model and the mechanical model. The thermal model calculates the temperature distribution in the component, based on the heat input from the hot gas stream calculated from the CFD analysis. The mechanical model calculates the stresses in the component, caused by the varying temperature distribution (calculated from the thermal model) and the externally applied loads. There are two sources of stress in rotating equipment: centrifugal forces due to rotation of the component and temperature gradients in the material. A transient thermal analysis can be performed for a complete flight with time varying gas temperature.

It must be noted that a limited number of CFD packages have the ability to incorporate fluid-structure interaction, in being able to calculate both the heat transfer coefficient and the stress profile. In which case the FE model would become redundant.

2.2.1.5 Lifing Model

A lifing model generally calculates either total time to failure or the number of cycles to failure for a certain component subjected to a specific load sequence. A large number of specific life prediction models have been developed over the past twenty years, where each model is appropriate for a specific application. The major division in lifing models is between total life models and crack growth models. Total life models only calculate the time to failure, not considering the way failure is reached. Crack growth models accept the presence of material

defects and aim to monitor crack growth and remove the component before the crack becomes unstable.

Crack growth models perform a local analysis, using stress profiles at very specific locations, being the location of crack initiation. The results are only valid for that location and can be affected by several different mechanisms, for example fatigue, creep or oxidation. The choice of lifing model ultimately depends on the expected failure mechanism of the component under consideration.

An important point to mention is the overall accuracy of Tingas model, the accuracy of the integrated model is obviously dependent on the accuracy of the separate tools and models. Tinga mentions that the inaccuracy of the FACE model is about 1 % and the GSP model about 2 %, provided that suitable integration steps are chosen. The accuracy of the temperatures calculated by the thermal FE model, is mainly determined by the accuracy of the heat transfer coefficients calculated by the CFD model. Where the inaccuracy of the CFD model is constant at 10 %.

Ganga (2002) also observed an uncertainty of over 10 % on a CFD analysis. Ganga performed an aerodynamic analysis on a 2-D turbine blade to calculate the temperature distribution on the surface of the turbine blade. The temperature distribution on the blade surface had a maximum inaccuracy of 15% on the suction side with an average inaccuracy of 11 % on the entire blade surface.

De Villiers (2002) performed a 2-D aerodynamic analysis on the SMR-95 blade. De Villiers calculated short duration heat transfer coefficients on the blade surface. The uncertainty was over 20 % when compared to experimental results. Both Ganga and de Villiers stress strongly that in order to accurately model heat transfer to a turbine blade, the complex flow problem must be fully comprehended and modelled highly accurately in the CFD model.

2.3 Turbine Blade Aerodynamics and Thermal Stress

The literature on aerodynamic and heat transfer prediction is most important, since the flow problem is far more complex than the thermal stress problem. The literature review will cover thermal stress literature first and then get into the complex world of turbine blade heat transfer prediction. Research into turbine blade heat transfer has been ongoing at the University of KwaZulu Natal for many years. The thermodynamics centre has build up a large collection of literature that accounts for a great portion of the literature review presented in this dissertation.

A thermal fatigue analysis, for cases of engine acceleration and deceleration on a turbine blade was performed by Maya et. al. (1978). This early research is of particular interest as it describes a study on turbine blade thermal stress analysis. Maya obtained unsteady thermal stress profiles by firstly performing a FEM prediction, on a 2-D steady and unsteady internal blade temperature profile. The boundary condition for the FEM simulation was of a convection type, requiring a surface heat transfer coefficient distribution and a free stream temperature.

Maya made numerous assumptions, such as, the free stream temperature, which was assumed to be the TIT profile for the acceleration and deceleration case. Maya also estimated that the thermal conductivity of the blade metal was constant regardless of temperature and, that the heat transfer coefficient along the blade surface was always equal to its initial value and stayed constant throughout the analysis.

The calculated internal blade temperature distribution was used as the boundary condition for the 3-D FEM prediction of unsteady thermal stresses. The temperature distribution was assumed to be constant in the spanwise direction. Maya showed that thermal stresses were as a result of the chordwise blade temperature distribution, which showed to be six to seven times greater than the thickness direction. The maximum stress was determined to be at the leading edge, and was taken as the stress component in the z-coordinate direction, which was ten times larger than the other two components.

The unsteady stress component in the z-coordinate direction was used as the boundary condition in the thermal fatigue analysis. Maya's thermal fatigue calculations were compared to and were in fair agreement with experimental thermal fatigue test data for the blade. A more recent study, Swaminathan and Allen (1995), also performed thermal fatigue experiments on a cooled turbine. The study showed that the highest tensile stresses occur on the colder surfaces of the cooling holes, on the inside of the blade. The experimentation showed that surface cracking occurred at the rim of the cooling holes.

A numerical solution for turbine blade thermal stresses, using a combined aerodynamic and thermal analysis is given by Bohn et. al. (1995). Unlike Maya, Bohn did not simplify the problem by applying the TIT to the blade surface directly, nor did Bohn assume the material properties to be constant with change in temperature. Bohn performed a CFD analysis and showed that the surface temperature is not only different from the TIT, but is also not spatially uniform along the surface, due to the effect of aerodynamic features in the flow and boundary layer.

Bohn performed a steady state analysis on the MARK II NGV cascade. The geometric configuration for the MARK II cascade was given along with the aerodynamic boundary conditions, making it possible to reproduce the problem. Additional aerodynamic data was found in Hylton et. al. (1983) and Nealy et. al. (1984). Bohn performed a numerical analysis for the flow field, which was solved by the Navier-Stokes equations with the Baldwin-Lomax algebraic turbulence model, using a finite volume form of the governing equations. Bohn compared the CFD predictions with the experimental data of Hylton et. al. (1983). The thermal analysis solved the internal blade temperatures and the stresses using the finite element method.

The completeness of the data presented by Bohn et. al., Hylton et. al. and Nealy et. al. made it possible to validate the CFD model. This validation was previously attempted by Ganga (2002). Ganga's results for the aerodynamic analysis were well outside the accepted engineering error of 5 %. The results were therefore not accepted. The temperature prediction resulted in an over prediction of 11 % for the blade surface. The predicted surface temperature profile did not match that of Bohn's experimental trend. This directly affected the thermal analysis where the stress results had an uncertainty of over 60 % on a greater part of the blade.

From Bohn's analysis and from the heat transfer literature in general, it is clear that an accurate thermal stress prediction is only possible if the flow field is accurately resolved, to determine the temperature distribution on the blade surface. An understanding of the numerical prediction for turbine blade flows is therefore a necessity. An extremely useful paper, Dunn (2001), reviews the progress of turbine blade aerodynamics and heat transfer research run by many research organisations over the last 30 years. It documents the progress from the early days of plain cascade measurements and the predictions using the original form of the Boundary-Layer code STAN 5, to the most recent fully instrumented rotating rig experiments and predictions, using 3-D Boundary-Layer and full Navier-Stokes codes.

The literature survey will here after follow a review of turbine blade aerodynamics and heat transfer. Numerical code development and prediction are the primary focus of this literature survey, however, the experimentation that accompanies numerical work will also be discussed. Dunn (2001) contains 489 references, the relevant papers mentioned by Dunn were all acquired and investigated and, are discussed in the remainder of the literature review.

In the 1970's, it was common practice to obtain pressures by solving the bulk flow using an inviscid Navier-Stokes or Euler code. Boundary-Layer codes were used to calculate the heat transfer using the pressure and velocity fields as boundary conditions. One of the earliest subsonic flow measurements in a plane turbine cascade, was performed by Langston et. al.

(1977). The study was however more orientated on flow visualization. Brown and Burton (1978) experimentally investigated the effect of free stream turbulence intensity and velocity distribution on heat transfer to curved surfaces. The findings showed that heat transfer increased with increasing turbulence intensity for a laminar boundary region, but was unaffected in a turbulent boundary layer. The point at which transition occurred was found to be sensitive to free stream turbulence intensity, velocity distribution and Reynold's number.

Graziani et. al. (1980) performed 3-D heat transfer measurements using a large scale cascade on the endwall and airfoil surfaces. The study showed that passage secondary flows greatly influence the heat transfer to the endwall and suction surface of the airfoil, but do not affect the pressure surface heat transfer. The experimental results were compared to the mid-span results predicted by the Boundary-Layer code STAN 5, developed by Crawford and Kays (1976). The Graziani data showed good agreement with the experimental data of Blair (1974). The measured values were lower than the values predicted by STAN 5. Graziani stated that the uncertainty in the comparison was due to there being no methods of calculating the flow field accurately.

Daniels and Brown (1981) used 5 different computer programs to calculate heat transfer to gas turbine blades, where each program incorporated a different turbulence model. The results were compared to the experimental data of Daniels (1978). The five models used in the study were:

- Cebeci-Smith (1974)
- Patankar-Spalding (1970)
- Cebeci-Smith-McDonald
- Wilcox 'EDDYBL'
- Wilcox (W-T)

The Cebeci-Smith model calculated the Reynold's stress terms using a mean field turbulent model and the eddy viscosity using Prandtl's mixing length model. Patankar-Spalding is modelled in a similar way to the Cebeci-Smith program, where the mixing length and eddy viscosity models are used, but the program was modified to include an experimentally derived turbulence model. In the Cebeci-Smith-McDonald program, the Reynold's stress is calculated using the mixing length. Dissipation of turbulent kinetic energy is modelled using a dissipation length scale and, turbulent kinetic energy in the boundary layer is calculated with a one-equation model. The Wilcox 'EDDYBL' program incorporates a two-equation model of

turbulence, the two-equation model of Wilcox (1975). The Wilcox (W-T) model uses tabular values for the turbulent Prandtl number.

The predictions of all five programs showed good agreement with the experimental data of Daniels in the laminar and fully turbulent regions on the suction surface, but showed poor agreement in the transition region on the suction surface and on the entire pressure surface. The two-equation models showed no advantage over the one-equation models. The conclusion was that there was no advantage of using more complex turbulence models.

Dunn and Stoddard (1979) performed heat transfer experiments on a sector of the first stage stationary inlet nozzle guide vane. Dunn and Hause (1982) furthered that work by performing heat transfer measurements on a section of a complete stage (stationary inlet nozzle, shroud and rotor). The study showed that the heat transfer rates for the stator-only measurements were less than that for the full stage, implying that the presence of the rotor affected the heat transfer to the upstream stator. Dring et. al. (1982) further emphasised the influence the rotor has on the upstream vane heat transfer.

Dunn et. al. (1984) furthered the work performed by Dunn and Stoddard (1979) and Dunn and Hause (1982). Dunn et. al. (1984) performed heat flux measurements on a sector of a full stage and presented predictions made using STAN 5 and a code developed by TDS (Turbine Design Systems). The heat flux data were presented as Stanton number distributions and the experiments were carried out for different wall to gas temperature ratios. The TDS predictions showed satisfactory correlation for the NGV and rotor pressure surface and poor correlation on the rotor suction surface. The STAN 5 predictions were generally acceptable, but the heat flux was consistently under-predicted on the NGV and rotor.

A numerical scheme based on the compressible Navier-Stokes equations was developed by Hah (1984), for 3-D turbulent flows inside turbine blade rows. The numerical procedure was based on a fully conservative control volume formulation with an algebraic Reynold's stress model, modified for the effects of streamwise curvature. Comparisons with the experimental data of Langston et. al. (1977) were in good agreement on the pressure side of the blade but not on the suction side. The model developed by Hah, was however able to show various complex 3-D viscous flow phenomena, such as 3-D flow separation near the leading edge and formation of the horseshoe vortex.

Hodson (1985) performed a study on the boundary layer of a high-speed turbine blade. The cascade measurements were done using an array of surface-mounted, constant-temperature,

hot-film anemometers. The measurements were interpreted with the aid of inviscid and viscous prediction codes. The study showed the effects that Reynold's number, compressibility, incidence and free stream turbulence have on boundary layer flows.

The low Reynold's number version of the k-ε two-equation turbulence model of Jones and Launder (1973), was incorporated into the 2-D Boundary-Layer code STAN 5 by Wang et. al. (1985), for the prediction of flow and heat transfer around turbine airfoils. A two-zone model was used to treat the k and ε variables in the near wall region. The heat transfer predictions were done for a flat plate, the C3X blade and the Turner airfoil. The predictions were compared with the experimental data of Hylton et. al. (1983) for the C3X blade and Turner (1971) for the Turner airfoil. For the C3X blade, the heat transfer predictions using the low Reynold's number of the k-ε two-equation turbulence model were better than the mixing length turbulence treatment used by Hylton. The overall heat transfer trends were all well predicted except at the leading edge, where Wang's solution over-predicted the heat transfer.

For the flow on the flat plate, the results of the k-ε model agreed very well with experimental data. The model had the capability of simulating transitional flow over the flat plate. The heat transfer for the Turner airfoil was well predicted except at the trailing edge. It was suggested that the overall heat transfer prediction could be improved, if a better velocity field was used at the boundary layer edge in the Boundary-Layer code. The leading edge heat transfer was not over-predicted because the inlet Reynold's number for the Turner airfoil was much lower than that for C3X blade. The flow for the Turner airfoil was therefore slower than for the C3X blade, resulting in a thicker viscous sub-layer thereby explaining the better performance of the low Reynold's number turbulence number.

Rodi and Scheuerer (1989) used a low Reynold's number version of the k-ε turbulence model developed by Lam and Bremhorst (1981), to predict turbine blade heat transfer using the finite difference form of the boundary layer equations. Lam and Bremhorst established that the model was valid throughout the fully turbulent and laminar regions of the flow and, it was able to predict transition. The predictions were compared with those of Daniels and Browne (1981). The pressure surface heat transfer was well predicted and on the suction surface, the heat transfer for the fully laminar and turbulent regions was also well predicted. The transition region heat transfer was in fair agreement with the data. During this time, most researchers favoured the low Reynold's number turbulence models as they worked well to provide closure for the boundary layer equations.

CFD codes had advanced to the point were steady 3-D predictions of full stage turbine blade rows, using either viscous Navier-Stokes codes or the combined inviscid Euler and Boundary-Layer codes, were possible. Joslyn and Dring (1992 – Parts I and II) carried out an experimental aerodynamic study on a one and half stage (first stator, rotor and second stator). The study was aimed at developing an improved understanding of the 3-D nature of turbine blade flows. Cascade experiments produced data that allowed code developers to assess the prediction of fundamental flow physics, but were unable to reproduce realistic operating environments. Joslyn and Dring compared the experimental results with the 3-D, compressible, viscous, full Navier-Stokes predictions of Rai (1987) and Adamczyk et. al. (1990). The predictions were in excellent agreement with the measured data. The study produced quality, 3-D full stage experimental data and showed that full Navier-Stokes solutions for full stage and multistage turbine flows can produce excellent aerodynamic predictions.

Full stage and multistage experiments brought about improved understanding of the three dimensional nature of turbine blade flow and provided an avenue for realistic unsteady experimentation. The Navier-Stokes solutions of unsteady 3-D flows were mainly restricted by the turbulence model limitations and limited computational capability of computers.

Unsteady pressure measurements on the vane and blade of a transonic turbine stage were performed by Dunn et. al. (1992). The experimental results were compared with Rao and Delaney's (1990) predictions from an unsteady Euler and an unsteady Navier-Stokes code. The experimental results only showed reasonable agreement with the predictions for both the vane and blade. The study concluded that the main drawback of using Navier-Stokes codes was the large computational grid density required to resolve the viscous affected region.

Dunn et. al. (1994) performed heat transfer and pressure measurements on two full stages of vane-blade rows. The measurements were compared to the predictions of a version of STAN 5 (Gaugler 1981), which was modified to include the Dunham transition model and, a quasi 3-D Navier-Stokes code (Chima 1986). The Navier-Stokes code incorporated the transition model of Mayle (1991), while the boundary layer edge condition for STAN 5 was obtained using the inviscid code Tsonic.

The Navier-Stokes prediction with the Mayle transition model agreed well with the experimental data. The Stan 5 model prediction was good in the laminar region and under-predicted the data beyond the point of transition. Dunn attributed the under-prediction of the results due to the flow not becoming fully turbulent with the Dunham transition model. The difference between the Stan 5 and Navier-Stokes prediction was more definite for low

Reynold's number flows than for high Reynold's number flows. This is because for high Reynold's numbers, transition occurs closer to the leading edge, making the flow fully turbulent over most of the blade.

Adamczyk (2000) summarizes the state of 3-D CFD based models of the time-averaged flow field within axial flow multistage turbomachines. Adamczyk gives an in-depth discussion on the development of mathematical models, from the simple mean flow governing equations, through the averaged passage model and the Reynold's averaged Navier-Stokes equations, to the present full Navier-Stokes solutions. Adamczyk stresses that it is vital to have the correct blade geometry and correct inflow and outflow boundary conditions as well as a suitable grid, before a simulation can be attempted. Grid development is important, as the results of a simulation depend as heavily on the choice of grid used as they do on the choice of turbulence model employed.

It is evident from literature that proper prediction of vane and blade surface pressure distribution is essential for predicting the corresponding heat transfer distribution. The ability of codes to predict the surface pressure distribution is significantly better, than the corresponding heat-transfer distributions. Code development over the past 30 years has evolved at an intense pace, however, there is no code in existence that can completely and accurately predict the highly complex fluid mechanics and heat transfer through a gas turbine. As computers become more powerful and the resolution capability of instrumentation improves, many of the issues discussed in this literature survey will be resolved. In addition, many new issues will appear that at the present time are unknown.

CHAPTER 3

COMPUTATIONAL METHODOLOGY

3.1 Method Description

In order to increase the turbine inlet temperature, air-cooled turbine blades are employed from the viewpoint of blade metal life. Because of the unsteady thermal stress caused during flight operation, thermal fatigue is one of the possible modes of failure in air-cooled turbine blades. Temperature distribution, which causes thermal stress, is not uniform in air-cooled turbine blades, by the effect of the cooling-hole arrangement, distribution of blade thickness and distribution of heat transfer coefficients along the blade surface. The final purpose of this study is to calculate realistic unsteady thermal stresses in an air-cooled turbine blade caused during an entire mission profile.

Since research into turbine blade thermal stresses began, through even into the 90's, simulations of unsteady viscous turbomachinary flow fields were impractical as a design tool, due to the long run times required. Designers relied predominantly on steady-state simulations, but these simulations do not account for some of the important flow physics. One of the earliest investigations of turbine blade thermal stress was performed by Maya et. al. (1978). The entire study was performed using a FEM code called NASTRAN. Maya et. al. (1978) calculated unsteady thermal stresses, which were used in a thermal fatigue analysis to determine crack growth rate.

Maya et. al. (1978) made numerous simplifications and assumptions to the FEM model, in order to reduce computing time. The time varying TIT was applied as a boundary condition directly to the blade surface, and the heat transfer coefficient along the blade surface was always equal to its initial value and stayed constant through the analysis. Maya et. al. (1978) also assumed that the thermal conductivity and elastic modulus of the blade metal were constant regardless of temperature.

The procedure presented by Bohn et. al. (1995) (here after referred to as Bohn) for calculating steady state thermal stresses, shows the mutual influence of the flow field and the temperature in optimising the thermal design of a blade. This is achieved by performing a combined aerodynamic and thermal analysis. The aerodynamic analysis was done using a

finite volume (FV) code and the thermal analysis using a finite element (FEM) code. By performing a combined aerodynamic and thermal analysis, the aerodynamic effects on surface heat transfer and temperature are accounted for, thereby giving a more realistic solution for the internal blade temperature. If the governing flow equations for the aerodynamic analysis and the stress equations for the thermal analysis were to be discretized by the same formulation, then the two sets of discrete equations could be coupled via the common blade temperature.

For the steady state model, it was decided to use the commercially available FV code FLUENT 6.1 for the aerodynamic analysis. Herein the blade and flow field must be modelled. The result of the aerodynamic analysis, i.e. the temperature distribution on the blade surface, is to be used as the boundary condition for the thermal analysis. The thermal analysis was performed by the commercially available finite element (FEM) code NASTRAN 2004. In the thermal analysis only the blade is modelled to calculate the internal temperature distribution and the corresponding thermal stresses.

The procedure used by Bohn for the steady state analysis can be extended to simulations where the TIT is unsteady with respect to time. This would result in the temperature profile on the turbine blade surface varying non-linearly with respect to time and spatially along the blade surface. As a result of the unsteady surface temperature, the thermal stresses inside the blade would also vary non-linearly with respect to time.

For the transient model, an unsteady aerodynamic analysis must be performed in order to acquire the unsteady turbine blade surface temperature distribution. Applying the unsteady surface temperature boundary condition in the thermal analysis will result in the desired unsteady stress plot with respect to time.

3.2 FLUENT

Computational Fluid Dynamics (CFD) is a useful tool in the gas turbine industry. Through the process of validating a computational program with experimental data and using that program for design efforts, great advantages can be reached. The use of computational methods can save designers significant amounts of both time and money; two of the factors essential for creating a profitable product. At the start of the project, an experimental rig for the measurement of thermal stresses was proposed. The cost of the rig, instrumentation, maintenance plans and computing power was in the region of R34000. The cost associated

with achieving the results numerically was R5000. The latter consisting of license fees. Which resulted in an 80% reduction in cost.

In a CFD code, a numerical solution involves conversion of the governing differential equations into a set of discrete algebraic equations, which are solved numerically by an iterative solution technique. A finite volume code uses the control-volume-based technique to discretize the governing continuity, momentum and energy transport equations using a computational structured or unstructured grid. The governing equations are then integrated over each control volume to yield discrete equations, which are linearized and solved by a linear equation solution algorithm. Adding or removing terms determined by the specifics of a problem results in a modified form of the general transport equations, which then define the problem. The modifications result from the various numerical models that have been developed to treat the different features, such as turbulence, that may be present in the flow.

3.2.1 Governing Equations

The Navier-Stokes equations, which are derived from the principals of conservation of mass, momentum and energy, are used to describe the fluid motion. The resulting equations, given below, are termed the continuity (Eq 3-1), momentum (Eq 3-2) and energy (Eq 3-3) equations. These are given in their most general form and are modified by the addition and / or subtraction of terms determined by the inclusion of mathematical models to describe the specific behaviour of flow, such as turbulence. This results in a set of transport equations that specifically describe the flow for a given problem or class of problems.

Continuity Equation:

$$\frac{\partial \rho}{\partial t} + \nabla \cdot (\rho \vec{V}) = S_m \qquad \text{Eq 3-1}$$

Momentum Equation:

$$\frac{\partial}{\partial t}(\rho \vec{V}) + \nabla \cdot (\rho \vec{V} \vec{V}) = -\nabla p + \nabla \cdot (\bar{\bar{\tau}}) + \rho \vec{g} + \vec{F} \qquad \text{Eq 3-2}$$

Energy Equation:

$$\frac{\partial}{\partial t}(\rho E_E) + \nabla \cdot (\vec{V}(\rho E_E + p)) = \nabla \cdot [k\nabla T - \sum_j h_j \overline{J_j} + (\overline{\overline{\tau}} \cdot \vec{V})] + S_h \quad \text{Eq 3-3}$$

In the general form of the governing equations given above, $\vec{V}$ is the vector of velocity components, ρ is the fluid density, p is the fluid static pressure, $\overline{\overline{\tau}}$ is the stress tensor (described by Eq 3-4 with μ being the molecular viscosity and I the unit tensor), $\rho\vec{g}$ and $\vec{F}$ represent the gravitational and body forces respectively. For the energy equation, E_E is given by Eq 3-5 (with h being the enthalpy) and k representing the thermal conductivity. The summation term accounts for the diffusion of species j. The source terms S_m and S_h are the mass addition and volumetric or species heat source respectively.

$$\overline{\overline{\tau}} = \mu[(\nabla\vec{V} + \nabla\vec{V}^T) - \frac{2}{3}\nabla \cdot \vec{V} I] \quad \text{Eq 3-4}$$

$$E_E = h - \frac{p}{\rho} + \frac{V^2}{2} \quad \text{Eq 3-5}$$

Turbulence is always three-dimensional, unsteady, rotational and most importantly irregular. Mathematical calculation of complete irregularity is impossible, but because the continuity assumption is valid for turbulent flows, the Navier-Stokes equations are valid. One way to solve or simulate turbulent flow, is by solving directly the instantaneous Navier-Stokes equations, an approach referred to as Direct Numerical Simulation (DNS) or Reynold's averaging. In Reynold's averaging, the solution variables in the instantaneous Navier-Stokes equations are decomposed into the mean (or time-averaged) and fluctuating components. Eq 3-6 shows the velocity component of the Reynold's Averaged Navier-Stokes equation (RANS).

$$V_i = \overline{V_i} + V_x' \quad \text{Eq 3-6}$$

Where:

V_i = instantaneous velocity

$\overline{V_i}$ = mean velocity

$V_x^{'}$ = velocity fluctuation (i = 1,2,3)

3.2.2 Numerical Modelling of the Governing Equations

Two algorithms for the solution of the RANS equations are available in FLUENT, being the Segregated and the Coupled solution algorithm. Using either solution algorithm, FLUENT solves the governing integral equations for the conservation of mass, momentum, energy and other scalars such as turbulence species. In both cases a control volume based technique is used that consists of:

- Division of the domain into discrete control volumes using a computational grid.
- Integration of the governing equations on the individual control volumes to construct algebraic equations for the discrete unknown variables (such as velocity, pressure and temperature).
- Linearization of the discretized equations and solution of the resultant linear equation system to yield updated values of the unknown variables.

3.2.2.1 Discretization

For the discretization of the governing equations, the equations are integrated over an arbitrary control volume V, shown by Eq 3-7 for the transport of a scalar quantity ϕ. The discrete form of the transport of the variable ϕ is given by Eq 3-8.

$$\oint \rho\phi\overline{V}\cdot d\overline{A} = \oint \Gamma_\phi \nabla_\phi \cdot d\overline{A} + \int_V S_\phi dV \qquad \text{Eq 3-7}$$

$$\sum_f^{N_{faces}} \rho_f \overline{V_f}\phi_f \cdot \overline{A_f} = \sum_f^{N_{faces}} \Gamma_\phi (\nabla\phi)_n \cdot \overline{A_f} + S_\phi V \qquad \text{Eq 3-8}$$

In Eq 3-7 and 3-8, $\vec{A}$ is the surface area vector, Γ_ϕ is the diffusion coefficient of ϕ, S_ϕ is the source of ϕ per unit volume, where V is the cell volume. N_{faces} is the number of faces enclosing the cell. ϕ_f is the value of ϕ convected through face f and, $\rho_f \vec{V_f} \cdot \vec{A_f}$ is the mass flux through the face, where $\vec{A_f}$ is the area of the face *f*.

The discrete value is stored at the cell centre, but cell values (at the cell faces) are required for the convection terms in the discrete equations. The face values are interpolated from the cell centre values by an upwinding scheme, implying that the upstream cell centre is used to derive the face value.

The choice of upwinding schemes used for a simulation is limited by the choice of solver and linearization technique employed. The manner in which the governing equations are linearized may either be implicit or explicit with respect to the unknown variables. Where:

Implicit – For a given variable, the unknown value in each cell is computed using a relation that includes both existing and unknown values from neighbouring cells. Therefore each unknown will appear in more than one equation in the system, and these equations must be solved simultaneously to give the unknown quantities.

Explicit – For a given variable, the unknown value in each cell is computed using a relation that includes only existing values. Therefore each unknown will appear in only one equation in the system and the equations for the unknown value in each cell can be solved one at a time to give the unknown quantities.

3.2.2.2 The Segregated Solution Algorithm

The segregated solver uses a method wherein the governing equations are solved sequentially and allows only implicit linearization. A point implicit (Gauss-Seidel) linear equation solver is used in conjunction with an algebraic multigrid (AMG) method to solve the system of equations. Many iterations of the solution loop must be performed to obtain a converged solution. Each iteration loop in the segregated solver consists of the following steps:

1. Fluid properties are updated based on the current (or initialised) solution.

2. The momentum equations for each velocity component are solved using current values for pressure and face mass fluxes, in order to update the velocity field.
3. A pressure correlation is applied if the velocity, pressure and mass fluxes do not satisfy the continuity equation.
4. Equations for scalars such as turbulence are solved using the current updated values.
5. A check for convergence is made (if the convergence criteria is satisfied, then the solution process is stopped)

3.2.2.3 The Coupled Solution Algorithm

In the coupled solver there is a choice of either using an implicit or explicit linearization for the governing equations. A Coupled-Implicit solution results in a coupled system of equations for each cell. Point Implicit (Gauss-Siedel) linear equation solver in conjunction with the AMG method is used to solve the coupled equation set. A Coupled-Explicit solver uses the multistage (Runga-Kutta) solver to solve the coupled equation set. The governing equations for the additional scalars, such as turbulence, are solved sequentially, separate from the coupled set. Each iteration loop in the Coupled solver consists of the following steps:

1. Fluid properties are updated based on the current (or initialised) solution.
2. The continuity, momentum, energy and species are solved simultaneously.
3. Equations for scalars such as turbulence are solved using previously updated values of the other variables.
4. A check for convergence is made (if the convergence criteria is satisfied than the solution process is stopped).

3.2.3 Turbulence Models

FLUENT 6.1 provides the capability of choosing between several different turbulence models in order to model flow as accurately as possible. The turbulence models available in FLUENT are:

- Spalart-Allmaras model (S-A)
- k - ε models
  - Standard k - ε model

- Renormalization-group (RNG) k - ε model
- Realizable k - ε model

- k - ω models
  - Standard k - ω model
  - Shear-Stress Transport (SST) k - ω model
- Reynolds Stress Model (RSM)
- Large Eddy Simulation (LES)

3.2.3.1 The Spalart-Allmaras Turbulence Model

The Spalart-Allmaras model is a one-equation model that solves a modelled transport equation for the kinetic turbulent viscosity. In its original form, the Spalart-Allmaras model is a low-Reynold's-number model and requires that the viscous affected region be properly solved. The model was designed specifically for aerospace and turbomachinary applications involving wall-bounded flows and boundary layers subjected to adverse pressure gradients. It was for these reasons that the model was considered as one of the models for the CFD analysis.

3.2.3.2 The k - ε Turbulence Models

The three k - ε models have similar forms and essentially model the turbulent productivity k, heat and mass transfer and, all account for compressibility effects in the same way. The difference between the models lies in the values for the Prandtl numbers, the method of calculating turbulent viscosity and the way in which the dissipation rate ε is calculated.

The standard k - ε model is a two-equation model in which the solution of two separate transport equations allows the turbulent velocity and length scales to be independently determined. The standard k - ε model is a high-Reynold's number model. The RNG k - ε model was derived from a mathematical technique called Renormalization Group Theory. The model contains an additional term in the ε equation and computes the turbulent Prandtl number from an analytical formula (the standard k - ε model uses user-defined, constant values). Low-Reynold's number effects are handled by an analytically derived formula for effective viscosity. The Realizable k - ε model differs from the standard k - ε model in two

ways; it employs a new formulation for the turbulent viscosity and it employs a new transport equation for ε. The term "Realizable" means that the model satisfies the mathematical constraints on the Reynold's stresses that are consistent with the physics of turbulent flow.

The performance of the three k - ε models depend on the treatment of the viscous flow in the near-wall region. The treatments are adaptations to the main k - ε model that are designed to solve the flow near the wall, taking the viscous effects and the no slip condition at the wall into consideration. The two near-wall treatments available in FLUENT 6.1 are:

- Wall Functions
- Enhanced Wall Treatment

The wall function approach does not solve the viscous sub-layer and buffer region, but instead uses semi-empirical formulae to bridge the viscous affected region with the fully turbulent region. The near-wall model modifies the turbulence models so that the viscous affected region, including the viscous sub-layer can be resolved. Special meshing techniques must be used when choosing a turbulence model and more importantly, when applying a near-wall treatment. The specific meshing parameters will be discussed in the next chapter.

3.2.3.3 The k -ω Turbulence Models

The Standard and the SST k - ω models have similar forms, with transport equations for k and ω. The standard k - ω model is modified for low-Reynold's effects. The SST k - ω model incorporates a blending function that switches from the standard k - ω model in the near-wall region to a high-Reynold's number version of the k - ε model in the free stream. The model also incorporates a modified turbulent viscosity formulation to account for the transport effects of the principal turbulent sheer stress. The Reynold's Stress model (RSM) and the Large Eddy Simulation (LES) model were not considered as these models require extreme computational time and memory.

3.3 NASTRAN

The Finite Element Method (FEM) was first developed for the use in aerospace and nuclear industries where the safety of structures is critical, however, the growth in usage of FEM is

directly attributed to the rapid advances in computer technology. As a result, commercially available FEM packages exist, one such package - NASTRAN 2004, was chosen for the thermal analysis.

FEM is a mathematical method for solving ordinary and elliptic partial differential equations via a piecewise polynomial interpolation scheme. FEM evaluates a differential equation curve by using a number of polynomial curves to follow the shape of the underlying and more complex differential equation curve. Each polynomial in the solution can be represented by a number of points, where the FEM evaluates the solution at these points only. A linear polynomial requires 2 points, while a quadratic requires 3. The points are the nodes of the meshed geometry. There are essentially three mathematical ways that FEM can evaluate the values at the nodes, there is the non-variational Ritz method, the Galerkin residual method and the variational Rayleight-Ritz method.

NASTRAN employs the Galerkin finite element method of weighted residuals to discretize the governing equations by dividing the computational domain into discrete elements. The governing equations are then interpolated over each element with an interpolation function to produce the discrete algebraic equations, which are solved iteratively, using a linear equation solver.

The thermal analysis is used to determine the temperature distribution, heat accumulation or dissipation, and other related thermal quantities in an object. The nodal degrees of freedom (the unknown data) are the temperatures. The primary heat transfer mechanisms are conduction, convection and radiation. For the thermal analysis only conduction is considered (convection is accounted for in the CFD analysis).

Conduction is governed by Fourier's law, which is a differential equation describing the rate of heat transfer as a function of temperature gradient, material thermal capacitance and the rate of internal heat generation. This law describes the temperature within the solid body. In order to carry out an analysis using a conduction model alone, temperatures must be described as part of the boundary condition description.

$$\lambda\left(\frac{\partial^2 T}{\partial^2 x^2}+\frac{\partial^2 T}{\partial^2 y^2}+\frac{\partial^2 T}{\partial^2 z^2}\right)+\dot{Q}=\rho c\frac{\partial T}{\partial t} \qquad \text{Eq 3-9}$$

Eq 3-9 shows the heat balance in the conduction equation. The basic conduction heat equation is structured as a heat balance. Where, λ is the thermal conductivity of the material under consideration, $\dot{Q}$ is the heat stored, ρ and c are the density and specific heat, respectively.

In section 3.2 FLUENT, it was necessary to give an in-depth discussion as to the inner workings of FLUENT and the turbulence models. This is because the discussion tied-up directly to the literature survey. It is not necessary to go through all the different material characteristics available in NASTRAN. Only one type of the material and element specifics for the thermal analysis needs discussion as it only relates to one kind of analysis. The formulation of the thermal analysis problem depends on the results of the aerodynamic analysis, therefore, a thorough discussion on the FEM model formulation is presented in Chapter 5, after the discussion on the aerodynamic analysis.

CHAPTER 4

COMPUTATIONAL FLUID DYNAMICS (CFD) MODEL DEVELOPMENT

4.1 Data for the Mark II NGV

Bohn presented results for the two-dimensional steady state combined aerodynamic and thermal investigation of a convention cooled, high-pressure turbine nozzle guide vane known as the Mark II. Bohn compared the simulation results with the experimental data of Hylton et. al. (1983). The geometry configuration of the Mark II NGV and the flow field are given in Figure 4-1. The geometric coordinates for the blade are given in Appendix B, along with all the coordinates for the cooling channels. The necessary boundary conditions for the flow passage are given in Appendix C, along with the heat transfer coefficients for the ten cooling channels and the mean temperature of the cooling air. These were determined experimentally by Hylton et. al. (1983).

Bohn's CFD analysis solved the compressible RANS equations discretized using the implicit FV formulation, with the Baldwin-Lomax, algebraic, eddy-viscosity, turbulence model providing closure for the RANS equations. The Fourier heat conduction equation was solved in the solid body with the fluid and solid regions coupled via a common wall temperature. The resulting linear system of equations was solved by Gauss-Siedel point iteration. The flow passage was meshed with 11920 grid points and the blade with 3212 grid points. The boundary layer mesh at the blade surface contained 10 cells with the height of the first cell centre being at a y^+ value of 0.3

The comparisons were given as distributions of pressure, temperature and heat transfer coefficient as a function of x/L (dimensionless axial chord) for the pressure and suction surfaces of the blade. These were compared with the results of the current study. The results given in Nealy et. al. (1984), compared experimental data with predictions done using a time-dependent, transonic, inviscid, cascade code, together with a modified version of the boundary layer code STAN 5 (Crawford and Kays 1974), which features zero-order turbulence modelling. Nealy's comparison was done for three exit mach numbers, one of which, exit Mach number = 0.98, was the case that was used in Bohn's study.

Bohn's FEM simulation was done using a commercially available FEM code called MSC.MARC/Mentat. The FEM computational grid for the blade employed higher order elements and contained 2032 elements with 6743 nodes. The simulation was done as a 2-D, plain strain problem and took into account temperature dependence of thermal conductivity, thermal expansion and Young's modulus. The blade material was ASTM 310 stainless steel, usually this material is not used for turbine blades, but it was chosen by the experimentators due to its low thermal conductivity, the material properties are listed in Appendix D. The FEM solved the internal blade temperature distribution and the corresponding thermal stresses. The results of the FEM simulation were given as contours of blade temperature and equivalent stress (σ_e).

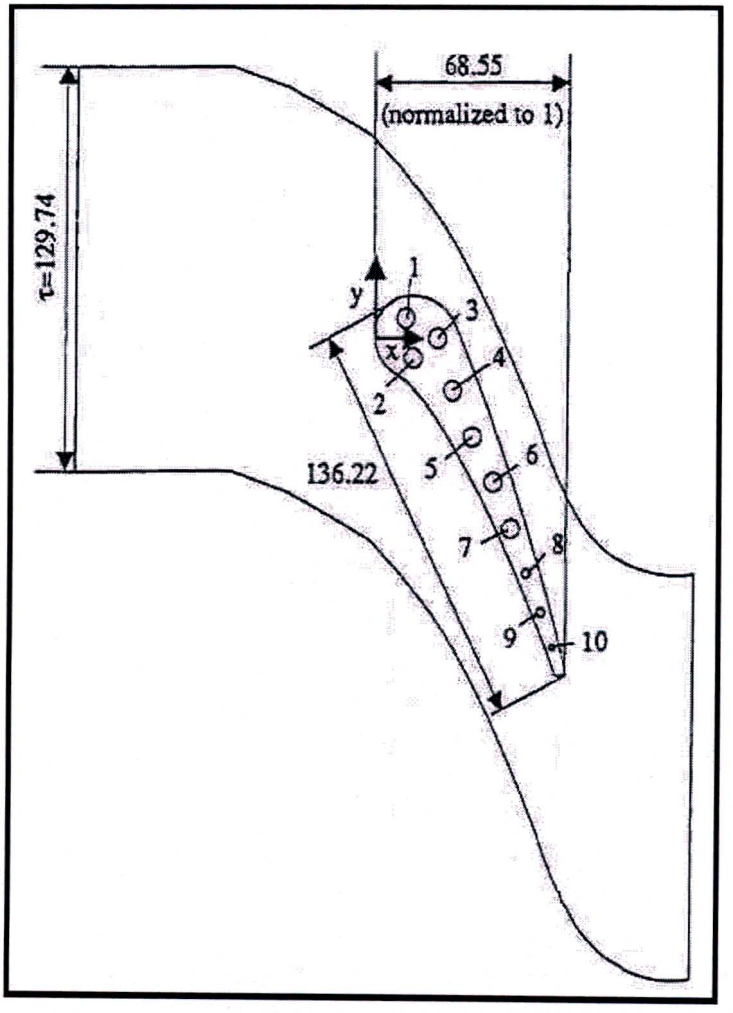

Figure 4-1: Geometric configuration for the Mark II NGV and the flow field reproduced from Bohn et. al. (1995)

4.2 Model Specification

The first step in setting up a model in FLUENT is creating the geometry of the problem. The pre-processor used by FLUENT to create the geometry is GAMBIT. The experimental results of Nealy et. al. (1984) were presented at the mid-span of the NGV. The model created in GAMBIT is therefore 2-D and is made up of vertices, edges and faces. GAMBIT is also used to mesh the geometry and select the solver used to solve the mesh. In all the cases discussed in this chapter, the solver that was used was FLUENT 6.1. This version of FLUENT allows for both unstructured and structured meshes.

For all the simulations performed in FLUENT, the Coupled implicit solver was chosen for the compressible flow solution. This solver uses 2nd order upwinding for the governing equations and 1st order upwinding for the additional turbulence scalar equations. The discrete equations are solved by Gauss-Siedel point iteration together with the AMG solver. The default Courant number for the coupled implicit solver is 5, which may be increased to speed up convergence or decreased for highly non-linear changes, such as at the start of a solution.

4.2.1 Boundary Conditions

A solution for the blade surface temperature necessitates that the Fourier heat conduction equation be solved. For this, the blade must be included in the model thereby making it necessary to not only model one blade-to-blade flow passage, but two such passages so that one blade is included in the model. The face that represents the main flow was set as a fluid continuum and the blade as a solid continuum. The GAMBIT geometry containing the flow field and blade is shown in Figure 4-2.

All the edges and faces of the GAMBIT / FLUENT model must be defined as specific boundary conditions. The blade surface and cooling holes were defined as WALL boundaries. The purpose of a WALL boundary is to impose a no-slip condition for the flow at that boundary. The surface heat transfer model is also enforced through the choice of WALL boundary heat transfer models. The heat transfer model used at the fluid-solid interface was a COUPLED thermal condition, which is used for 2-sided wall heat transfer, i.e. convection from the fluid to solid and conduction within the blade. For the cooling holes, a CONVECTION heat transfer model was enabled, using the heat transfer coefficients and the free stream temperature of the cooling air given in Table C-1.

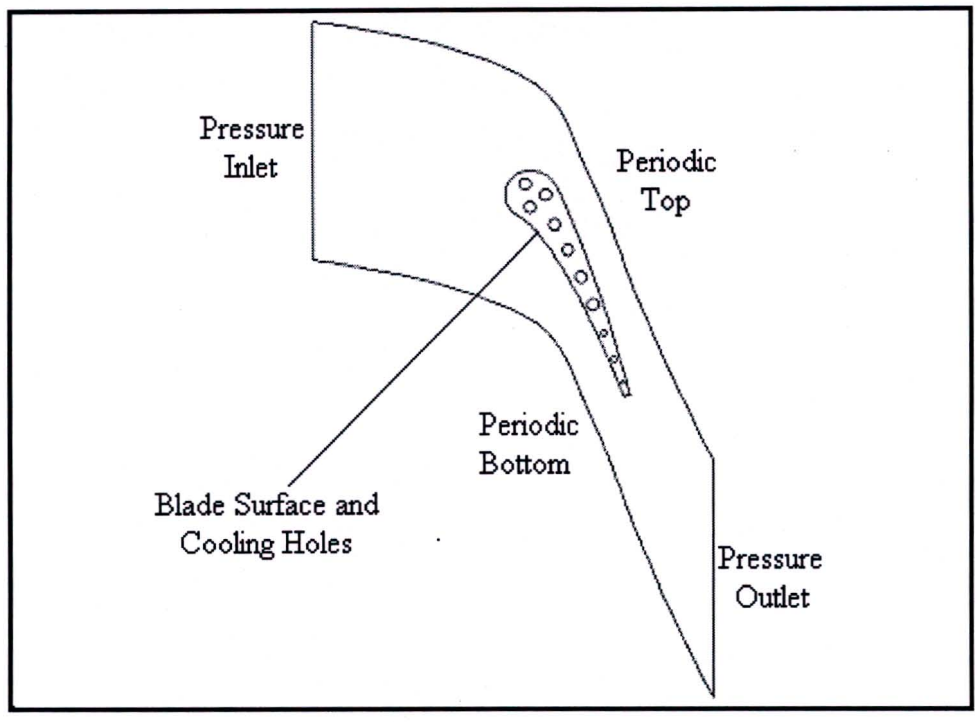

Figure 4-2: GAMBIT and FLUENT geometry for the aerodynamic analysis

Nealy et. al. (1984) performed the experiments on a seven vane cascade for the MARK II NGV. Seven vanes are used for cascade experimentation in order to be certain that the flow field around each blade is identical. To reduce the computational domain, a section of the flow field containing one blade is modelled with the section boundaries being PERIODIC.

The justification is that the flow above and below the top and bottom edges respectively, will be the same, thereby rendering them periodic. This type of Boundary definition, ensures that the flow entering / leaving the top boundary, matches the flow leaving / entering the bottom boundary respectively. The fluid inlet and outlet were defined as PRESSURE INLET and PRESSURE OUTLET respectively. These are mandatory flow inlet and outlet definitions for compressible flow with the required model inputs being total and static pressure and free stream turbulence level for the inlet, and static pressure and free stream turbulence level for the outlet.

The FLUENT input values for PRESSURE INLET and PRESSURE OUTLET are listed below in Table 4-1 and Table 4-2 respectively.

Setting	Value/Method
Gauge Total Pressure (Pa)	334000
Supersonic/Initial Gauge Pressure (Pa)	325690
Total Temperature (K)	788
Direction Specification Method	Normal to Boundary
Turbulence Specification Method	Intensity and Hydraulic Diameter
Turbulence Intensity (%)	6.5
Hydraulic Diameter (cm)	12.974

Table 4-1: PRESSURE INLET boundary conditions for the FLUENT model

Setting	Value/Method
Gauge Total Pressure (Pa)	167000
Backflow Total Temperature (K)	788
Direction Specification Method	Normal to Boundary
Turbulence Specification Method	Intensity and Hydraulic Diameter
Turbulence Intensity (%)	6.5
Hydraulic Diameter (cm)	12.974

Table 4-2: PRESSURE OUTLET boundary conditions for the FLUENT model

The setting 'Supersonic/Initial Gauge Pressure" refers to the static pressure at the inlet, while the "total temperature" refers to the total stagnation temperature at the inlet. The "Turbulence Specification Method" was set to " Intensity and Hydraulic Diameter" with the hydraulic length being set to the length of the inlet and the turbulence intensity set to 6.5 %. The turbulence intensity was determined experimentally by Nealy et. al. (1984), based on combustor-induced turbulence intensity.

4.2.2 Material Specification

The setting of the material property when analysing compressible fluid flow is extremely important. The most important factor is setting the density of the operational fluid to 'ideal-gas'. If this is not done, then the model will not be solved as a compressible flow problem. Therefore the density was given ideal-gas properties. Other material properties can also be set, such as the specific heat, thermal conductivity and viscosity. These were left at the

prescribed FLUENT default values, although various relationships can be selected such as piecewise-linear/polynomial or kinetic, which employ the temperature of the flow to derive these parameters. By prescribing ideal-gas properties to the density, the solver recognizes that the flow is compressible and automatically enables the energy equations.

The "ideal-gas" equation modelled in FLUENT is shown below by Eq 4-1.

$$\rho = \frac{p_{OP} + p}{RT} \qquad \text{Eq 4-1}$$

Where: p_{OP} - Operating Pressure [Pa]

p - Local Relative (gauge) Pressure [Pa]

R - 287 KJ/kgK = Universal Gas Constant

From Eq 4-1 it can be seen that specifying the operating pressure plays a relevant part in setting up the CFD model.

4.2.3 Operating Pressure

The operating pressure is an important factor to consider when setting up the model. The first reason is that it directly determines the density, as can be seen in Eq 4-1. It is also significant in low Mach number flows because of its role in avoiding round-off errors. Table 4-3 below shows how to set the operational pressure based on the Mach number.

Density Relationship	Mach Number Regime	Operating Pressure
Ideal-gas law	M > 0.1	0
Ideal-gas law	M < 0.1	Mean Flow Pressure

Table 4-3: Recommended settings in FLUENT for operational pressure

With the flow in the model being transonic the operating pressure was set to 0 Pascal's.

4.2.4 Initialization and Convergence Criteria

In order to begin iterating a solution, it was necessary to initialise the domain. For the first computation of each model, the entire domain was initialized to the velocity, gauge pressure and temperature values prescribed at the inlet. The turbulent kinetic energy and turbulence dissipation rate were initialized to the values representative of a turbulence intensity of 6.5%, where these values are computed by FLUENT.

By far, the most critical part of a solution is in determining whether the solution has converged. Before running a simulation, the many factors that govern the solution converged must be accurately set to suit the type of simulation. Rough convergence is acceptable if only approximate flow features are desired from a simulation, however when simulating the heat transfer to a turbine blade, deep and accurate convergence is required.

There is no universal law for judging convergence of a solution. The reason for this is due to the iterative nature of the solution procedure. Iteration is necessary to handle the non-linearity of the equations that govern fluid flow, heat transfer and other related processes. For any given conservation equation, an approximate solution is obtained at each iteration that results in a small imbalance in the conservation equation. During the course of the iterative solution algorithm, the imbalance in each cell is a small, non-zero value that decreases as the solution progresses. This imbalance is called the residual. The residual is scaled so that the residuals of different variables can be compared. Scaling factors are taken from the bulk flow of the variable through the domain.

The convergence criteria are pre-set conditions on the residuals that indicate a certain level of convergence. The FLUENT default setting requires that all the scaled residuals decrease to 10^{-3}, which indicates that the overall error in the variables is about three orders of magnitude less than the bulk value in the system. For all the simulations performed, all the scaled residuals were set to a convergence criteria of 10^{-3}, except for the energy and continuity equations for which the criteria was 10^{-5}. Each simulation was continued for 200 iterations beyond convergence to insure that the residuals continued to decrease steadily. The general idea is that as the residuals decrease so does the error in the solution. It was noticed in the simulations that the difference in the results, when compared to convergence at 10^{-3} and 10^{-5} for the energy and continuity equations, was never more than 4 %.

The second criterion that was used to check for convergence was the mass flow balance at the flow boundaries. The solution was considered be converged when the difference in the

mass flow rate through the PRESSURE INLET and PRESSURE OUTLET flow boundaries was less than 0.01 %. Only when both the convergence criteria were satisfied were the results retrieved from FLUENT.

4.2.5 Grid Independence and Adaptation

In order to insure that the correct solutions are calculated, a grid sensitivity study was necessary for each different model created. The idea was to demonstrate that the solution was insensitive to the size of the mesh. The grid insensitivity was determined by computing a solution for a specific model, refining the mesh in critical regions, and then comparing the results until changes could no longer be detected. When changes in the results no longer occur, it can be said that the model is grid independent. At such a time the simulation results can be compared to the experimental and should prove to be the same. This is the best way to judge the accuracy of a simulation. If the results differ to the experimental, then the correctness of the experimental results can be questioned or the CFD model must be redone from scratch.

Mesh generation is the first and foremost important step in creating an accurate CFD model. A vast amount of time was spent in creating and modifying the mesh to suit the type of simulation being run. Once the mesh is created in GAMBIT and a simulation is performed then, by studying the results, the mesh can be adapted in certain areas. There are two ways in which to modify a mesh. Firstly, the mesh can be modified manually in GAMBIT once the areas for adaptation have been marked. Secondly, FLUENT allows for solution-based grid adaptation. It provides the ability to adapt the grid, based on specific values or gradients of important flow characteristics such as velocity, temperature, pressure or turbulence. It also allows adaptation based on a wide range of desired wall unit values, or on specific flow boundaries.

The second approach was attempted many times, however every attempt failed as FLUENT reported fatal errors and promptly closed down. The error was reported to the FLUENT technical support. The reason for the adaptation failing was that FLUENT version 6.1.18 was simply unable to perform adaptations on a model that consisted of periodic boundaries. The only draw back of this was that the grid would have to be modified manually, this meant that time was wasted. However, very little time was spent modifying local regions of the grid. The main flow region, which can only be meshed manually, proved to be the most problematic task, and will be discussed later in the chapter.

4.3 The Aerodynamic Analysis

FLUENT 6.1 is designed to solve both unstructured and structured meshes. An unstructured mesh can contain either triangular, quadrilateral or a hybrid combination of both cell types. Quadrilateral (quad) cells are favoured to triangular (tri) cells. The FV method works on quad cells. If tri cells are employed in the model then the FV "transforms" the tri cells into quad cells for the formulation, this then leads to round-off errors.

Figure 4-2 shows the highly curved model geometry. The majority of time spent on the development of the CFD model was in generating the most suitable mesh in GAMBIT. The turbulence models that were investigated in FLUENT were the Spalart-Allmaras, k - ε and the k - ω models, along with all the near-wall treatments available.

4.3.1 Unstructured Mesh Using Only Triangular Cells (Grid 1)

It was decided that the mesh for the geometric model would be constructed slowly by starting off with a simple unstructured mesh that consisted of only tri cells. Figures 4-3 and 4-4 show the unstructured mesh. The flow field was meshed with 10315 cells and the solid region (the blade) with 3894 cells.

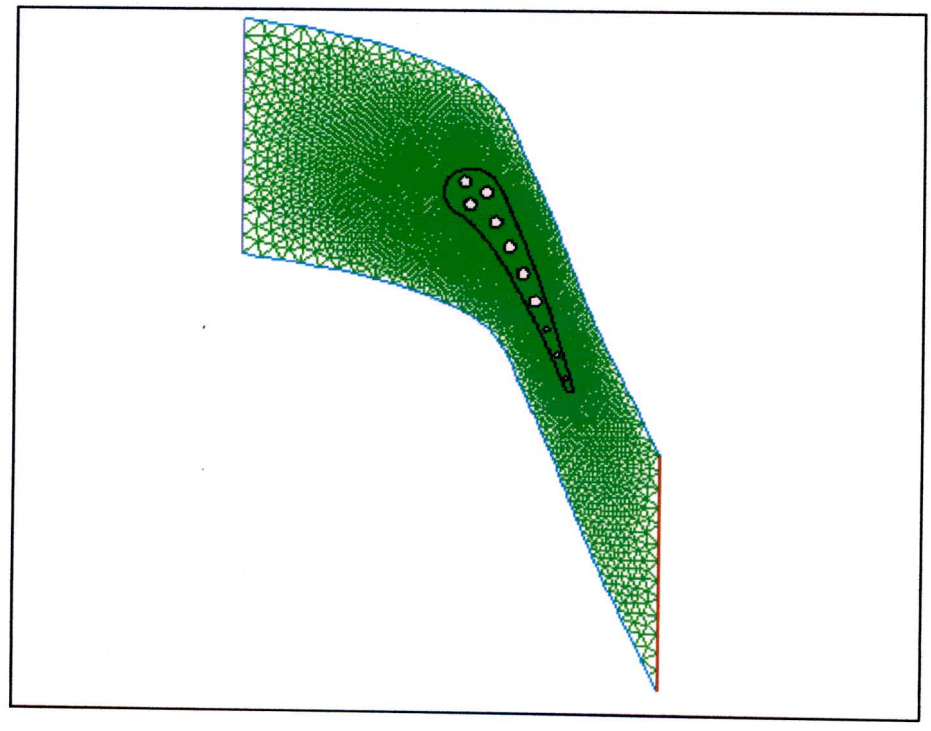

Figure 4-3: Unstructured triangular mesh (Grid 1)

High pressure, temperature and velocity gradients are expected near the blade wall, where as such gradients will not be present in the bulk flow. It follows that the grid would have to be fine near the wall and coarser in the free stream. To ensure that the mesh gradually increases away from the blade wall, a Sizing Function was employed for main flow mesh. The blade surface was discretized with elements of size = 0.1 (grid was created in cm) and the flow boundaries with elements of size = 1. The Sizing Function then ensures that the cells will linearly increase in size from the blade surface to the flow boundaries. The mesh in the solid region had a constant element size = 0.1.

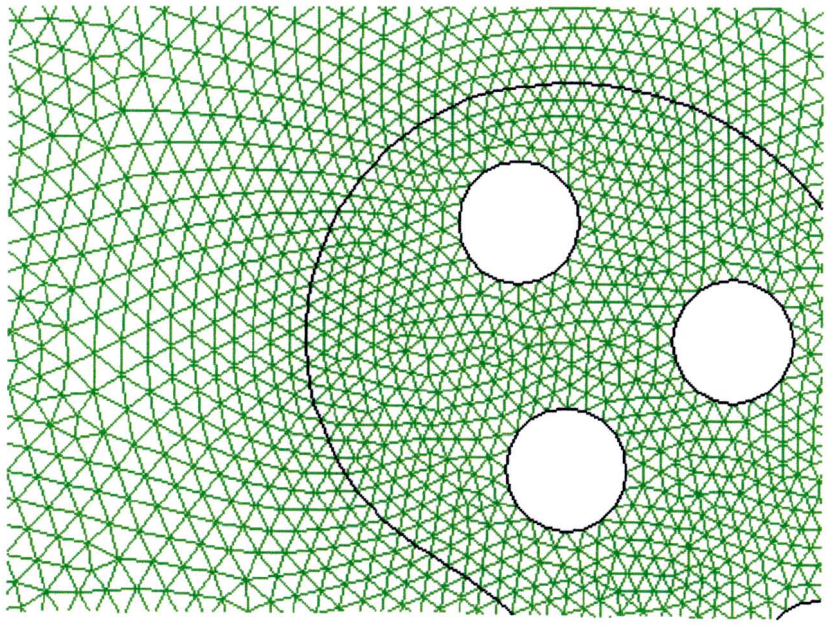

Figure 4-4: Close up of the unstructured triangular mesh (Grid 1)

Only the Spalart-Allmaras (SA) turbulence model was investigated for the unstructured mesh. The reason being that, unlike all the other turbulence models, the SA model is designed to work for small y^+ values as well as for $300 > y^+ > 30$. The y^+ values in the near-wall for the first cell were all in the order of 300. The entire boundary layer around the blade surface was housed in the first cell. As a result, no clear aerodynamic features could be seen in the near wall region. Figure 4-5 shows the pressure distribution, the SA turbulence model shows excellent agreement with the data on both the pressure and suction side of the blade. The temperature distribution (shown in Figure 4-6) however, varies significantly from the data. It is evident from figure 4-6, that the boundary layer has not been accurately modelled. As a result, a boundary layer mesh will have to be employed. Figures F-1 and F-2 show the pressure and temperature contours, respectively, for the Spalart-Allmaras turbulence model.

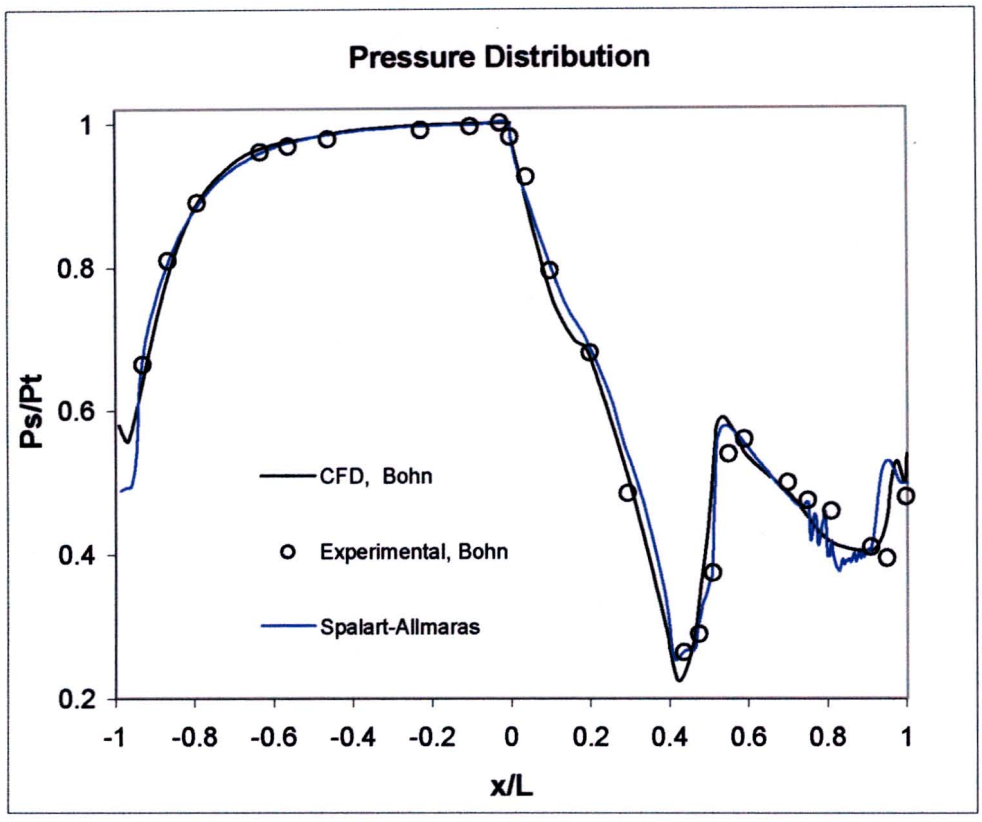

Figure 4-5: Pressure distribution from the aerodynamic analysis using the Spalart-Allmaras turbulence model for Grid 1

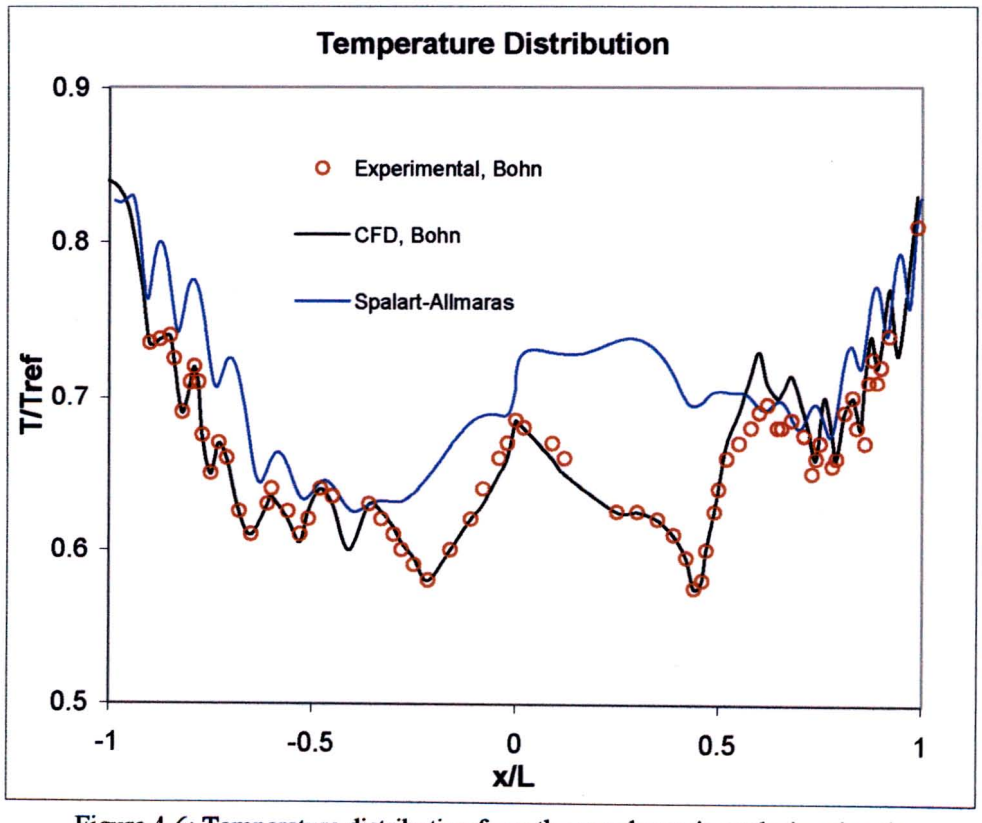

Figure 4-6: Temperature distribution from the aerodynamic analysis using the Spalart-Allmaras turbulence model for Grid 1

4.3.2 Boundary Layer Mesh on Grid 1

It is evident from the results of the first analysis that a boundary layer mesh is required. A boundary layer mesh was therefore used at the fluid-solid interface. The purpose of a boundary layer mesh is to give control over the y^+ values, which is a critical issue when solving for heat transfer in the near-wall region. Figure 4-7 below shows the general structure of a velocity boundary layer.

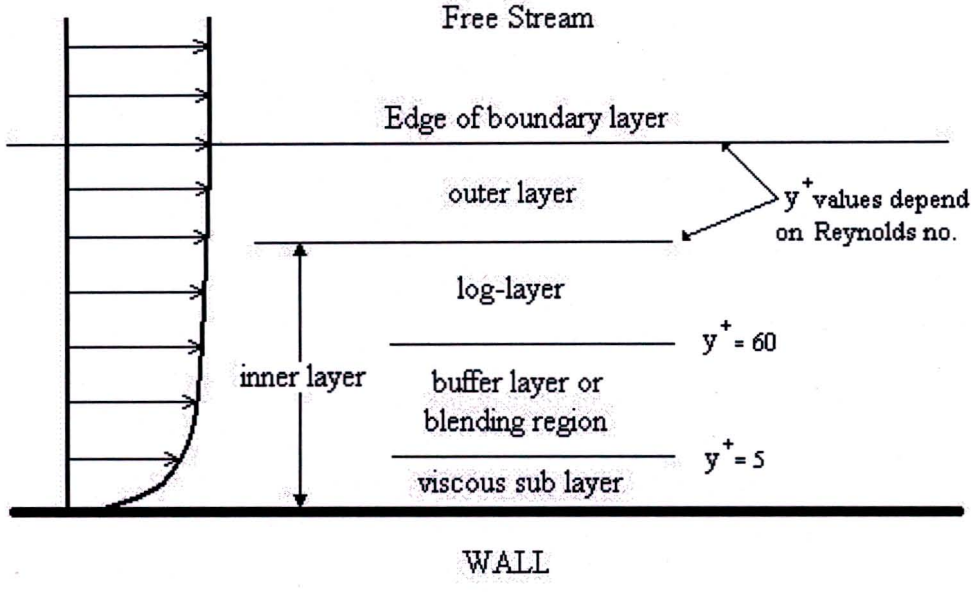

Figure 4-7: The structure of a velocity boundary layer in the near-wall region

The size of the boundary layer mesh is dependent on the type of turbulence model and near-wall treatment being employed in the simulation. For the enhanced near-wall treatment, which combines the two-layer model with the enhanced wall functions, a fine enough near-wall mesh is required to fully resolve the viscous affected region. The two-layer model uses the k - ε model for the fully turbulent region and the Wolfstein (1969) one-equation model in the viscous affected zone. The differentiation between fully turbulent and the viscous affected zone is defined by the Reynolds number based on the perpendicular distance y from the wall, as shown below in Equation 4-2.

$$\mathrm{Re}_y = \frac{\rho\sqrt{ky}}{\mu} \qquad \text{Eq 4-2}$$

Equation 4-2 defines fully turbulent main flow for which $Re_y > 200$, the boundary layer mesh should therefore only extend into the flow up to where $Re_y = 200$. The enhanced wall functions use a single-wall-law for the entire near-wall region by blending the linear and logarithmic (laminar and turbulent respectively) laws of the wall using a blending function. The blended single-wall-law ensures correct asymptotic behaviour for small and large y^+ values, and is capable of predicting the velocity profile for $3 < y^+ < 10$. For the enhanced wall treatment, FLUENT suggests a y^+ value of order 1, but not greater than 4 to 5, this keeps the first cell within the viscous affected region. Furthermore, there should be at least 10 cells within the viscous affected region, i.e. the boundary layer.

It was therefore necessary to create a boundary layer mesh with a y^+ value of 1. One way to achieve this is by arbitrarily choosing a first cell size in the near wall region and then simulating a solution. Post-processing features in FLUENT allow the user to view the y^+ values. Based on the y^+ values, the first cell size can then be increased or decreased in GAMBIT, to achieve a $y^+ = 1$. This method requires many simulations to finally achieve $y^+ = 1$. As the flow conditions for example change, with say a decrease in velocity, the boundary layer would as a result thicken, and a new first cell size would have to be used to achieve a y^+ of 1. This would again result in many simulations having to be performed.

It was thought to attempt to calculate the first cell size. The boundary layer for a flat plate can be calculated, using the flow conditions for the blade. This would give a good estimate for the first cell size. With the endless amount of literature available on flat plate theory, this choice seemed to be the most ideal starting point. Incropera and De Witt (1996) give the following equation for y^+:

$$y^+ \equiv \frac{yu_\tau}{\nu} \qquad \text{Eq 4-3}$$

Rearranging Eq 4-3 for y (which is the distance to the first cell's centroid) and substituting for the desired $y^+ = 1$, Eq 4-4 is derived:

$$y \equiv \frac{\nu}{u_\tau} \qquad \text{Eq 4-4}$$

Where:

$$u_\tau \equiv \sqrt{\frac{\tau_w}{\rho}} = U_e \sqrt{\frac{\overline{c_f}}{2}} \qquad \text{Eq 4-5}$$

Where for a flat plate the friction coefficient $\overline{c_f}$:

$$\frac{\overline{c_f}}{2} \approx 0.0037 \mathrm{Re}_L^{-\frac{1}{5}} \qquad \text{Eq 4-6}$$

Where U_e is the free stream velocity. This value was taken from the first Fluent simulation (Grid 1). The free stream velocity at the boundary layer edge was taken around the entire blade. A constant value of $1.79 \cdot 10^{-5}$ was also taken from the first simulation for the kinematic viscosity, ν. The Reynolds number, Re_L, along the blade was calculated using the exit velocity and chord-length. From the calculation, the Reynolds number at the exit was $1.89 \cdot 10^6$, which would suggest that the flow is fast and turbulent in nature. Figure 4-8 shows the distance to the wall's adjacent cell centroid for $y^+ = 1$, based on Eq 4-4.

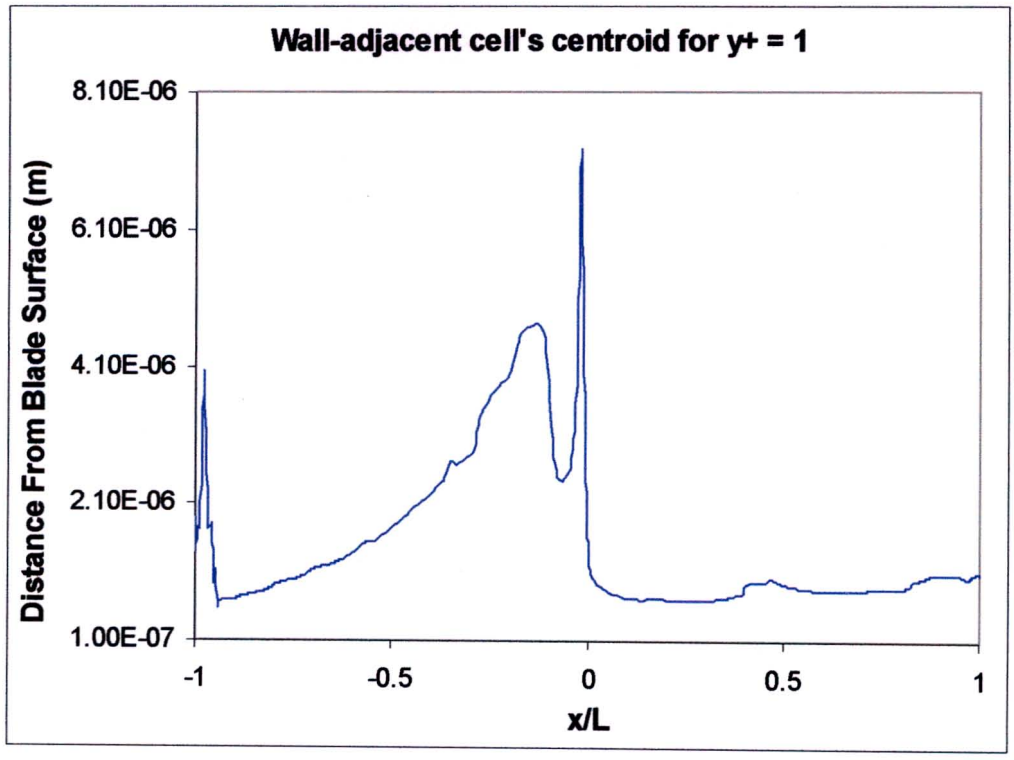

Figure 4-8: Distance from blade surface to the first cell's centroid for $y^+ = 1$, based on flat plate theory

From Figure 4-8, a first row cell size 'a' of 0.000314 (cm) was chosen for the boundary layer mesh. FLUENT recommends that adjacent cells do not differ by more than 20 % in size, therefore a growth rate (GR) of 1.2 was chosen for the boundary layer mesh, which contained 24 rows. The boundary layer mesh was attached to Grid 1, the solid mesh was unchanged with 3839 cells while the boundary layer mesh added 1318 cells to the flow field mesh that consisted of 11633 cells.

Two extremely important default settings for the boundary layer mesh must be changed in GAMBIT before creating the grid. The Use_Facet_Evals setting controls the evaluation type used in boundary layer attachment, by default (1) it uses a faceted evaluation. The setting was changed to (0), which then uses exact evaluation. The Ouick_N_Dirty setting specifies what kind of graphics representation of boundary layers is performed. The default setting (1) skips face projection in graphics presentation of boundary layer nodes to gain speed, but at the loss of accuracy. The setting was changed to (0) which then performs the projection to face according to specified evaluation type. These settings are extremely important when performing heat transfer simulations with a boundary layer mesh, as the boundary layer mesh must be attached to the "exact" geometry surface. Figure 4-9 shows a close up of the boundary layer mesh for Grid 1.

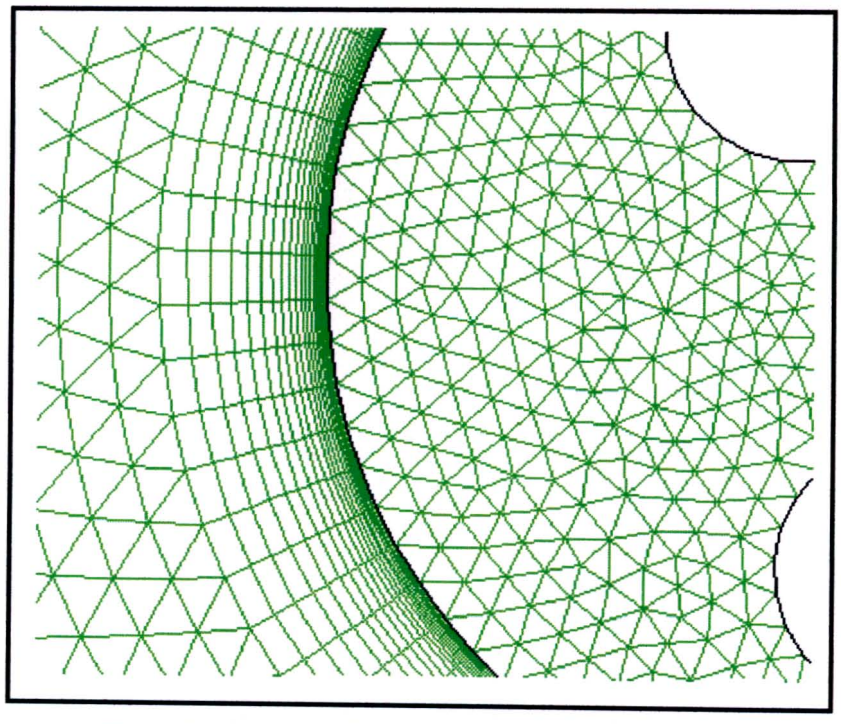

Figure 4-9: Close up of Grid 1 with a boundary layer mesh

When the simulations with the BL mesh were performed, fatal errors were immediately at the start reported by FLUENT. A grid check revealed that there were cells with a negative volume present in the grid, this occurs when meshing a highly curved geometry. The problem was with the BL mesh at the trailing edge. The problem and solution to this is shown in Appendix E.

The four turbulence models that were investigated were the Spalart-Allmaras, Standard and Realizable k - ε with enhanced wall treatment and the SST k - ω models. Three boundary layers were also investigated, the proposed BL with a first cell size of 0.000314, another one with a first cell size of 0.001, which would place the first cell in the buffer layer, and one with a first cell size of 0.00001, which equates to having over 20 cells in the viscous affected region.

Of the four turbulence models investigated, the SST k - ω model, which was supposed to be designed for these flows, performed the worst. It gave the poorest surface pressure and temperature prediction. The problem for the MARKL II is considered to be HRN problem with the $\mathrm{Re} = 1.89 \cdot 10^6$. The model's poor performance is believed to be because its formulation is designed for LRN flow in the near-wall region. The velocity profile on the blade surface is turbulent in nature over most of the blade, making the LRN viscous affected region thin. The combination of very fast moving flow and the thin LRN zone are believed to be responsible for the SST k - ω poor performance. The model was therefore discarded and the Spalart-Allmaras, Standard and Realizable k - ε models were further investigated.

The three models investigated for a first cell size of 0.000314 all had the same y^+ values at the blade surface, as shown in Figure 4-10. For the enhanced wall treatment FLUENT suggests a y^+ value of order 1, but not greater than 4 to 5, to keep the first cell within the viscous affected region. The y^+ values were all between 1 and 4, and hence the first cell size calculation for a flat plate proved to be accurate.

All three of the turbulence models predicted the pressure distribution extremely well, following the experimental data almost identically, as can be seen in Figures 4-11 to 4-13. All the models follow the data slightly better than Bohn's CDF prediction. It is evident from the graphs that a boundary layer with a = 0.001 cannot predict the steep pressure rise at 44 % axial chord on the suction side, which is as a result of a shock wave. The first cell was placed in the buffer layer as a result of the large first cell size of 0.001, and hence the crucial viscous sub-layer was not modelled. This is believed to be the reason for the models poor

performance. The boundary layer was therefore discarded all together from the investigation. The boundary layer with a = 0.00001 performed equally with the boundary layer of a = 0.000314, it is almost impossible to tell the graphs apart. From the pressure plots it can be seen that there is no advantage of using a first cell size that corresponds to a y^+ value that is smaller than 1, as is the case with a = 0.00001.

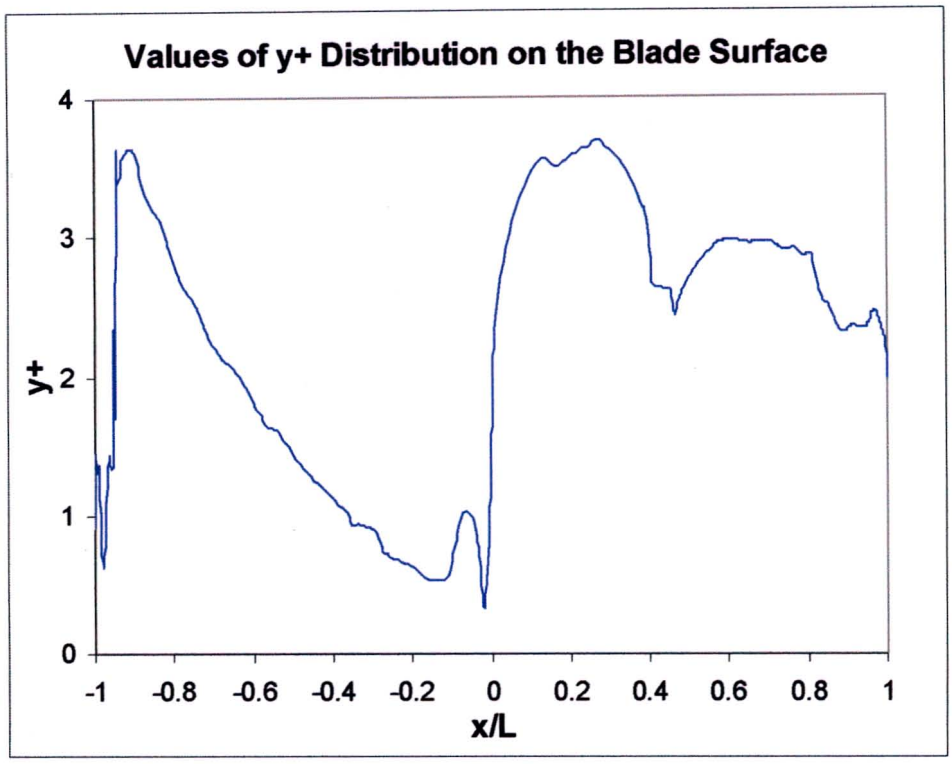

Figure 4-10: Distribution of y^+ values along the blade surface for a first cell size of 0.000314

The open literature has emphasised that correct prediction of the blade surface pressure is a necessary first step in obtaining good heat transfer prediction. Correct surface pressure prediction would be the result of the out-of-boundary-layer flow field being accurately resolved. The turbulence models investigated have all shown excellent agreement with the data for the pressure; the temperature correlation however does not share the same success.

The SA and Standard k - ε models, show better temperature prediction from 50 % to 100 % axial chord on both the pressure and suction side. This is to be expected as the two turbulence models would naturally better predict the turbulent rather than laminar flow, as is shown in Figures 4-14 and 4-15. The boundary layer with a = 0.00001 shows a slightly better prediction than that with a = 0.000314, with the difference being in the order of 1 %. The Realizable k - ε model showed equally fair temperature prediction on both the pressure and

suction surface for the last 50 % axial chord, for both boundary layers, as shown by figure 4-16. The boundary layer with a = 0.00001 over predicts the data by 12 % around the leading edge, where the bigger boundary layer (a = 0.000314) correlates better with the data. Although the data is over predicted by an unacceptable amount by the BL with a = 0.00001, this is the only model that shows the capability of predicting the steep temperature rise at 44 % axial chord on the suction surface, which is caused by a shock wave.

The temperature results so far do not warrant the model as being validated against the experimental data. Because of the poor correlation with the data, a detailed discussion on the flow features in the main flow as well as those in the boundary layer will be reserved until an acceptable temperature prediction is achieved. None of the turbulence models show any superiority so far in predicting an accurate temperature distribution. The Realizable k - ε model with enhanced wall treatment and a first cell size of a = 0.00001 is the only model so far that can resolve the transition at 44 % axial chord on the suction side. Figures E-3 to E-8 in Appendix E, shows the contours of static pressure and temperature for the models investigated

It is still uncertain as to which boundary layer size is capable of resolving the viscous affect layer better, both will be further investigated and incorporated by the Spalart-Allmaras, Standard and realizable k - ε models. The boundary layer mesh has now been fully investigated, and shows that the heat load calculated to the blade surface is highly sensitive to a varying first cell size. The main flow mesh has so far been discretized by only triangular cells. FLUENT recommends that quadrilateral cells be used rather than triangular. The next section will discuss the development of a quad grid for the main flow, keeping the current boundary layers the same.

The main criteria for choosing between triangular and quadrilateral elements is due to numerical diffusivity. Numerical diffusivity is most noticeable when a problem is convection-dominated, such as the case is the present study. Numerical diffusion is minimized when the flow is aligned with the mesh. The last mentioned point is the most relevant for the choice of applicability in this study. It is clear that if one uses a triangular mesh the flow can never be aligned with the grid. On the other hand, if one uses a quadrilateral mesh this situation might occur. The flow around a turbine nozzle guide vane is streamlined (such is the function of a nozzle guide vane), hence the use of quadrilateral elements is fully justified by this fact.

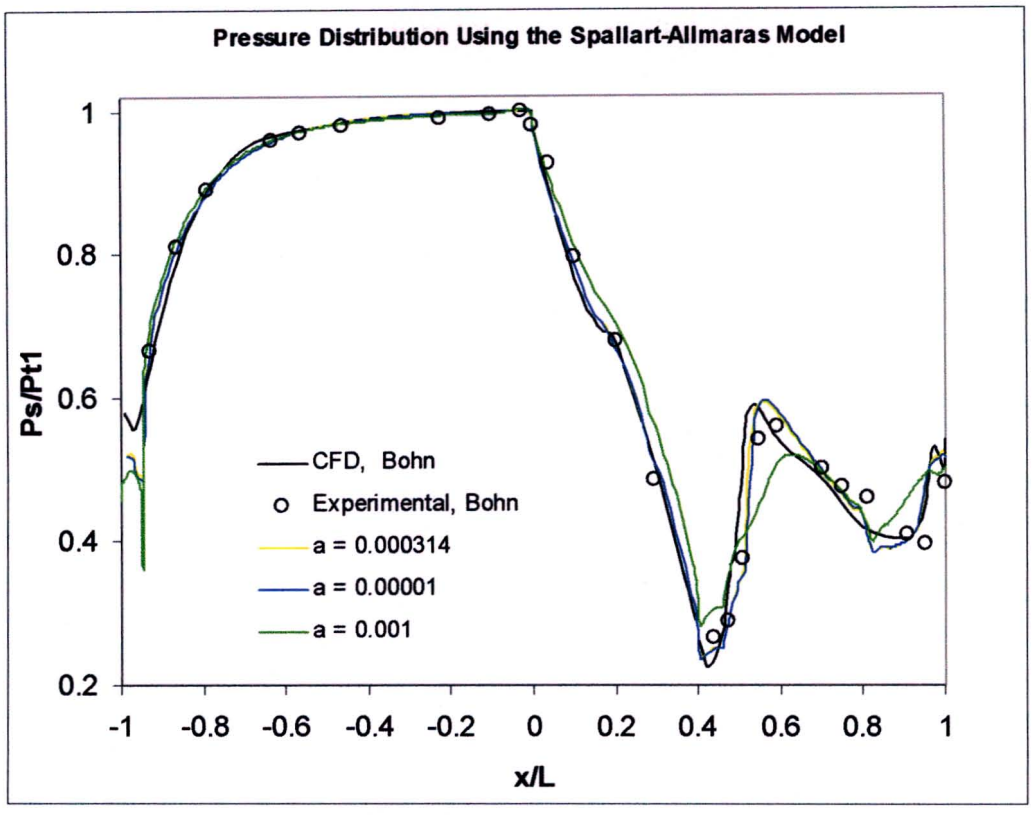

Figure 4-11: Pressure distribution from the aerodynamic analysis for a varied first cell size using the Spalart-Allmaras turbulence model

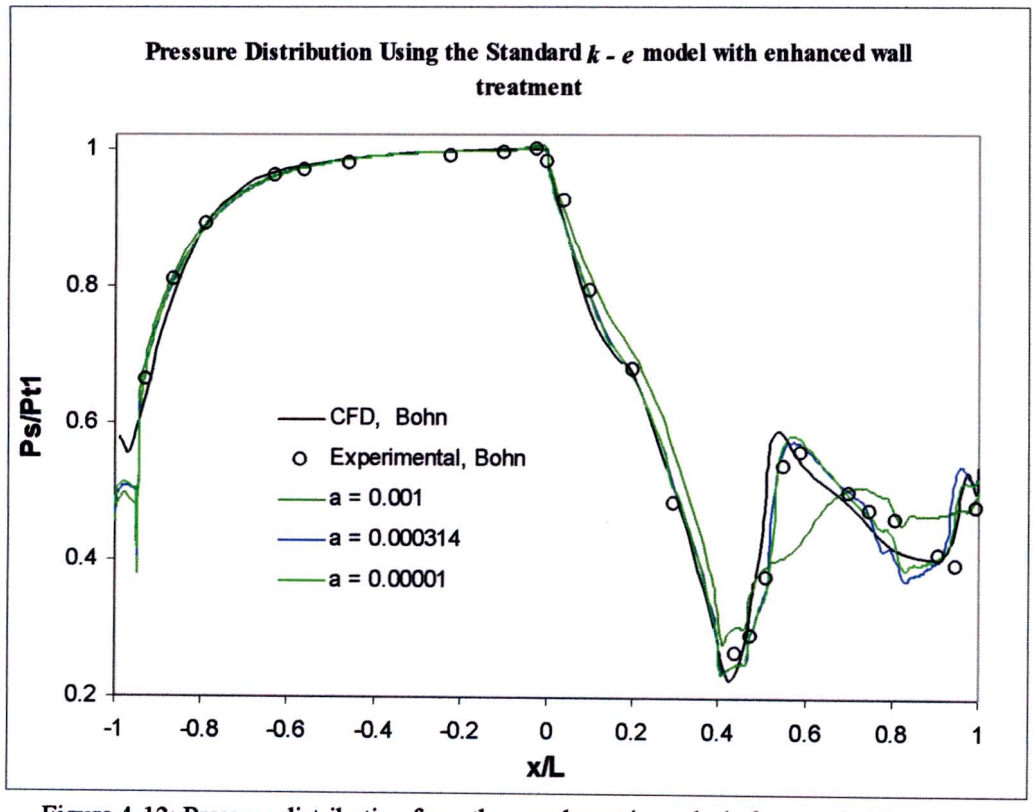

Figure 4-12: Pressure distribution from the aerodynamic analysis for a varied first cell size using the Standard $k-e$ turbulence model with enhanced wall treatment

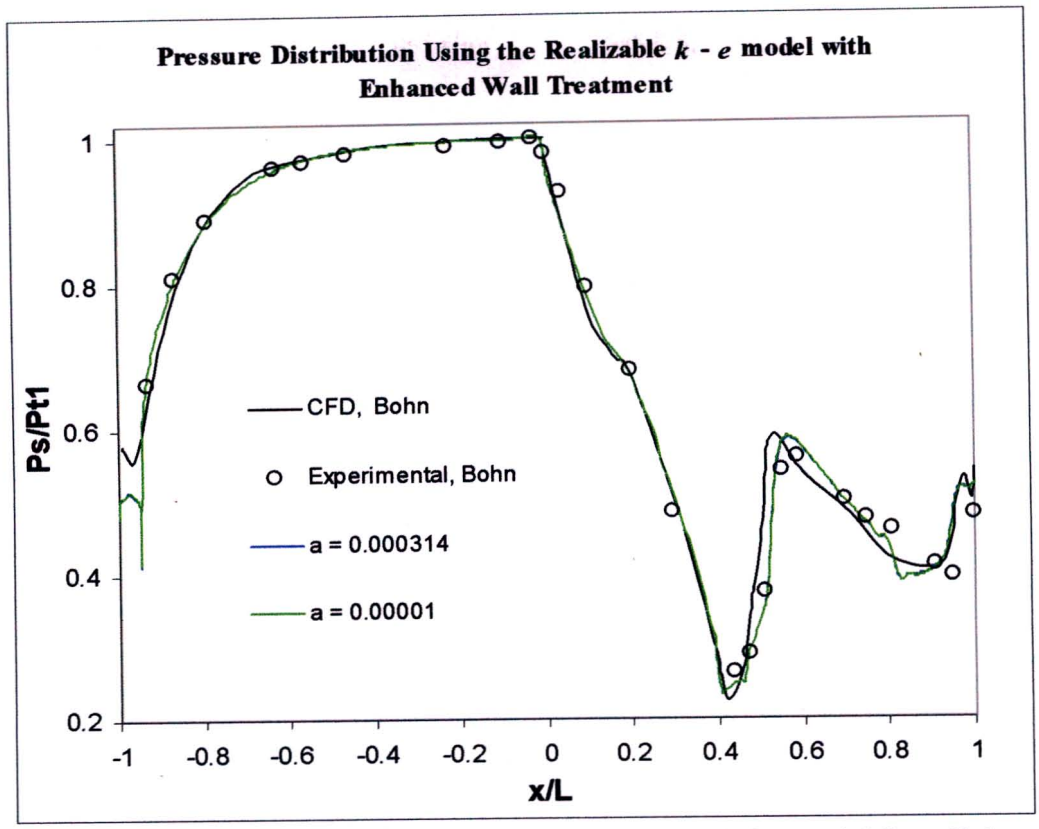

Figure 4-13: Pressure distribution from the aerodynamic analysis for a varied first cell size using the Realizable $k-e$ turbulence model with enhanced wall treatment

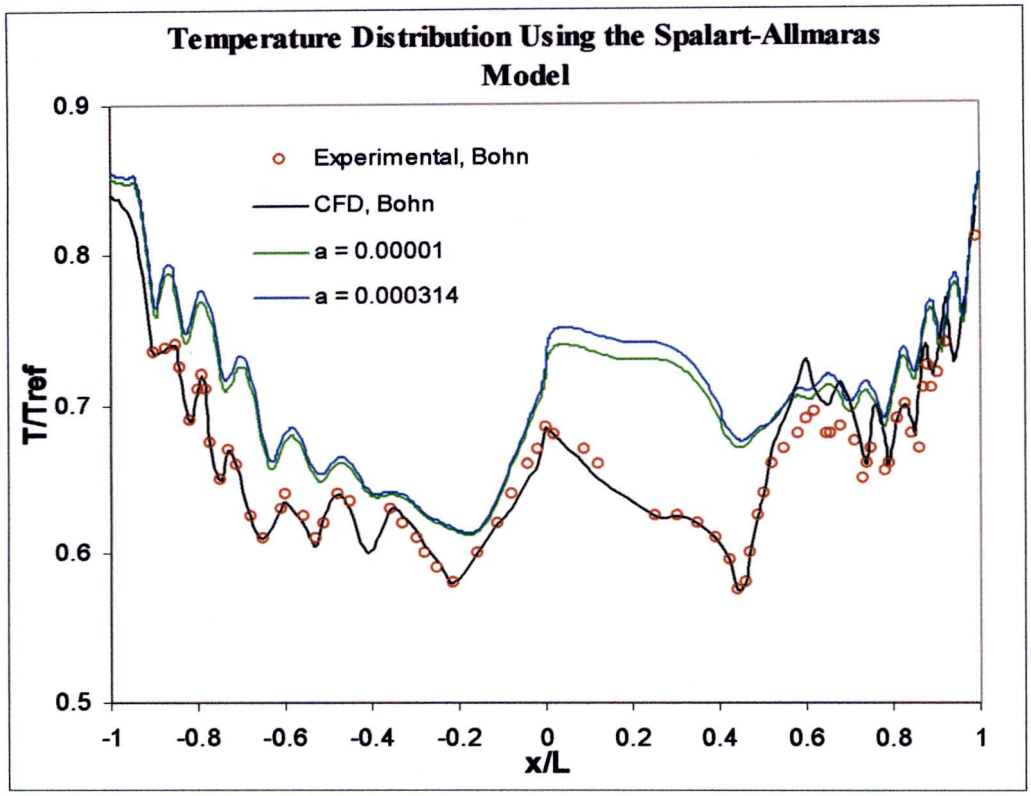

Figure 4-14: Temperature distribution from the aerodynamic analysis for a varied first cell size using the Spalart-Allmaras turbulence model

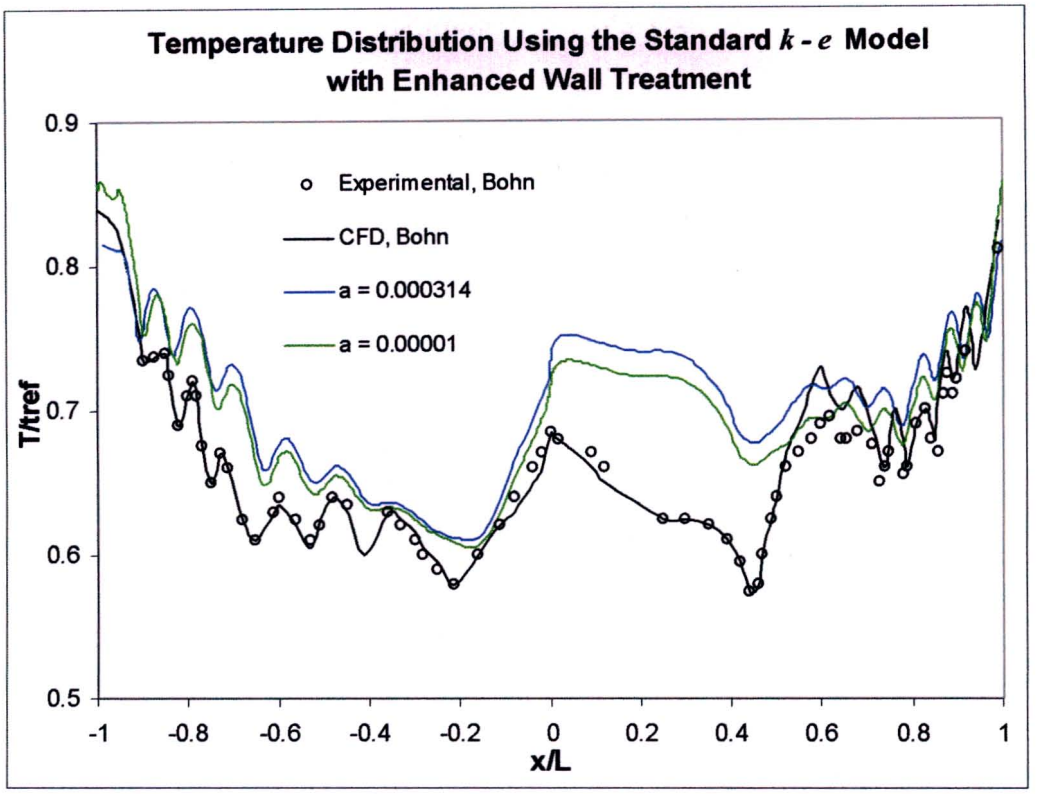

Figure 4-15: Temperature distribution from the aerodynamic analysis for a varied first cell size using the Standard $k-e$ turbulence model with enhanced wall treatment

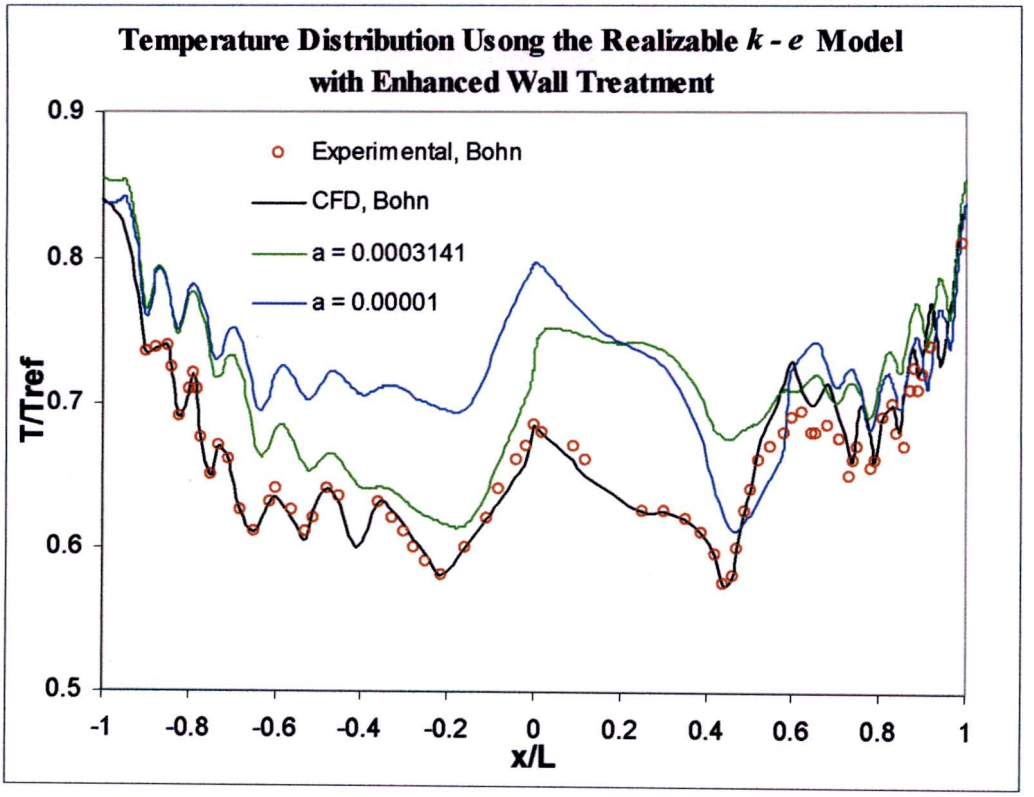

Figure 4-16: Temperature distribution from the aerodynamic analysis for a varied first cell size using the Realizable $k-e$ turbulence model with enhanced wall treatment

4.3.3 Unstructured Mesh With Quadrilateral Cells (Grid 2)

The reason for the discrepancy between the experimental data and the predicted data for the temperature was believed to be as a result of the main flow not being accurately modelled. Varied first cell sizes were employed into the boundary layer mesh, and no turbulence model was able to predict the correct temperature distribution on the blade surface. The problem was believed to lie in the flow characteristics, which were not properly resolved using the tri mesh in the main flow. As a result, the flow conditions at the boundary layer edge (which depend on the resolution of the main flow characteristics) were inaccurate.

It was therefore decided to remesh the main flow with quad cells. Due to the high curvature of the blade and the periodic boundaries, it was extremely difficult to achieve a structured orthogonal quad mesh. This problem was not encountered when a tri grid was used, because it is geometrically easier to fit triangular cells into a highly curved area. The unstructured quad mesh that was created is shown in Figure 4-17. The solid mesh was unchanged from that of the Grid 1, which contained 3894 cells, while the flow mesh consisted of 10236 quad cells. The same sizing function that was applied to grid 1 was applied to the flow field. The highly skewed cells can be seen in the figure. These cells caused great difficulty in the simulation, as the solution struggled to converge. FLUENT suggests that cells with EquiAngle skewness of 0.8 or above will not allow a solution to converge. A value of 0 represents a perfectly orthogonal quad cell.

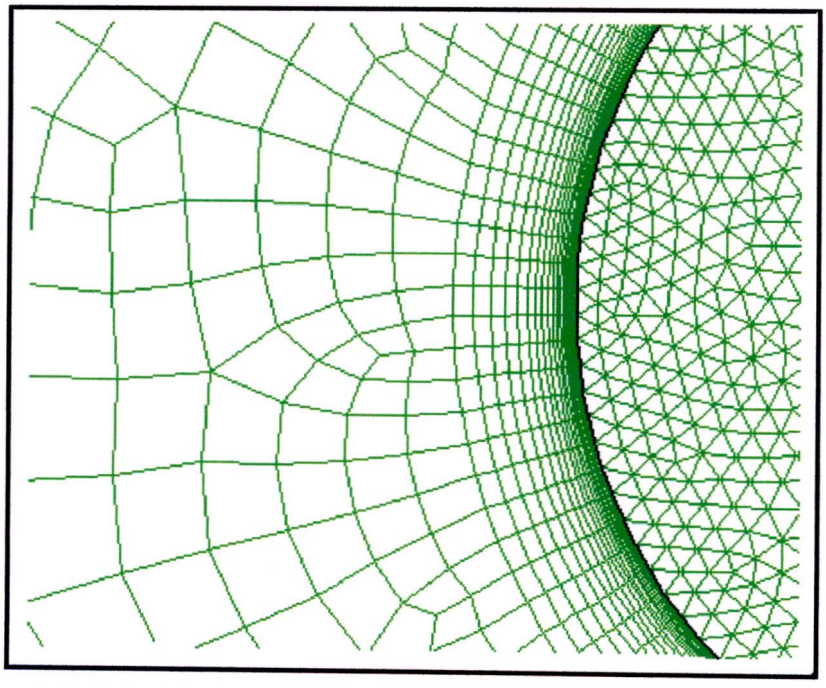

Figure 4-17: Unstructured Quad mesh with a boundary layer mesh (Grid 2)

Cells with an EquiAngle skewness of above 0.6 cause instability as well as inaccuracy in the simulation. Using the post processing tools available in GAMBIT, a grid check was performed that showed over 100 cells that had a value of between 0.6 and 0.7. One way to improve a mesh is to apply a smoothing scheme to the mesh. There are three smoothing algorithms available in GAMBIT. The Length-weighted Laplacian scheme, that uses the average edge length of the elements surrounding each node and tends to average the element edge lengths. The Centroid Area scheme, which equalizes areas of adjacent cells, and the Winslow scheme, that optimises element shapes with respect to perpendicularity.

All three smoothing meshes were applied to the quad mesh, which resulted in an improved mesh with only 7 cells above an EquiAngle skewness value of 0.6, with the worst cell at a value of 0.654. Almost 93 % of all the cells had a value below 0.5. Ideally all the cells should have a value of 0, however, this is impossible to achieve with a highly curved geometry. The problem with skew cells lies in the fact that only one extremely skew cell is required for a simulation not to converge. Figure 4-17 shows the large change in cell size from the last row of the boundary layer cells to the adjacent main flow cells. The adjacent main flow cells were up to 5 times larger, exceeding the recommended growth of 1.2.

The results of the simulation did not improve beyond the previous results. The results for the pressure follow the data extremely well, as was the case with the previous results. Figure 4-18 shows the comparison between the three turbulence models for a first cell size = 0.000314. The results for the temperature distribution for both boundary layer meshes did not improve. The prediction by the Spalart-Allmaras model worsened from the previous results (from the unstructured tri grid) by 2 %, as shown by Figure 4 -19. The Standard k - ε model with enhanced wall functions also worsened, also deviating further from the data by roughly 2 %.

The Realizable k - ε model with enhanced wall functions performed the same as it did previously for the laminar region around the leading edge. The model showed better temperature prediction on the pressure surface from 40 to 100 % axial chord. On the suction surface, the data was under predicted from 70 to 100 % axial chord. Only the results for the boundary layer with a first cell size = 0.000314 are presented, as the results for the second boundary layer show the same trends. The static pressure and temperature contour plots for the Realizable k - ε model with enhanced wall functions are shown in Figures F-7 and F-8 in Appendix F.

It can be concluded from the analysis that there is no clear advantage in using an unstructured quad mesh. The temperature prediction for the Standard and Realizable k - ε models improved slightly, but worsened slightly for the Spalart-Allmaras model. This result however is not entirely useless, as it emphasises what was mentioned before. That is, that the resolution of the boundary layer depends on the accuracy of the main flow resolution.

The boundary layers were identical for both the unstructured tri and quad main flow mesh, yet when each turbulence model was applied to a different unstructured main flow mesh, the results differed. Therefore it seems that neither the tri nor the mildly skewed quad mesh is capable of resolving the main flow mesh accurately. In order to get acceptable correlation for the temperature between the prediction and the data, a main flow mesh that consists of near-perfect orthogonal quad cells will have to be developed.

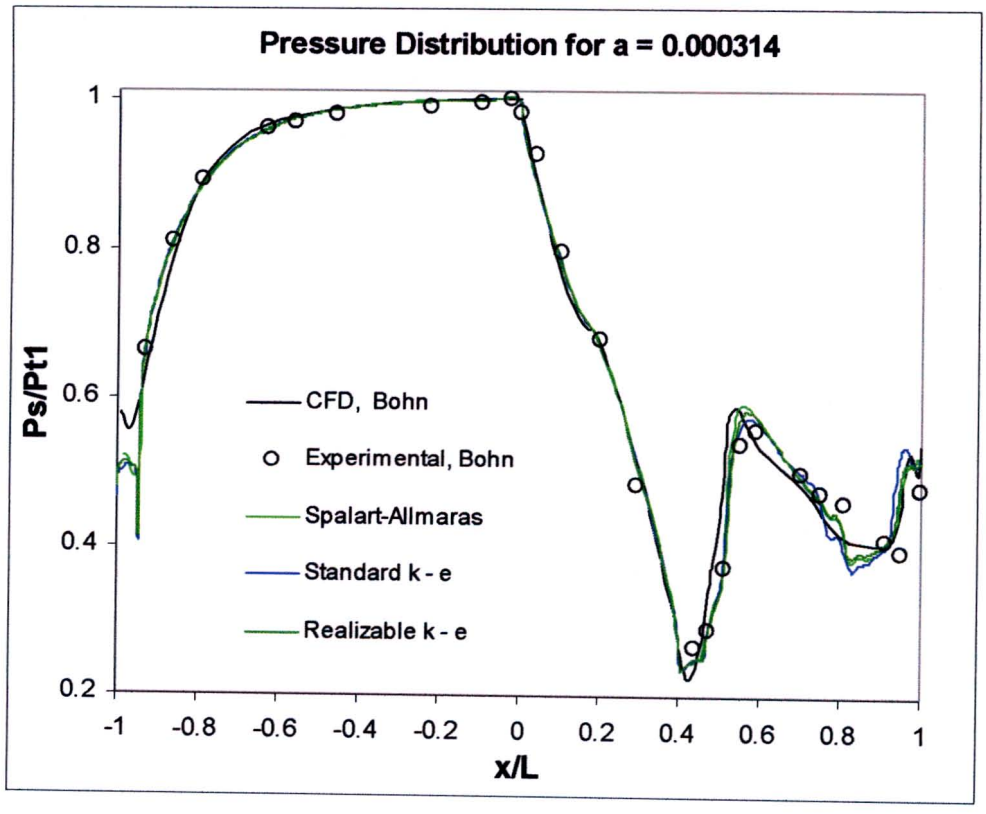

Figure 4-18: Pressure distribution from the aerodynamic analysis for a first cell size equal to 0.000314 using the Spalart-Allmaras, Realizable and Standard $k-e$ turbulence models with enhanced wall treatment

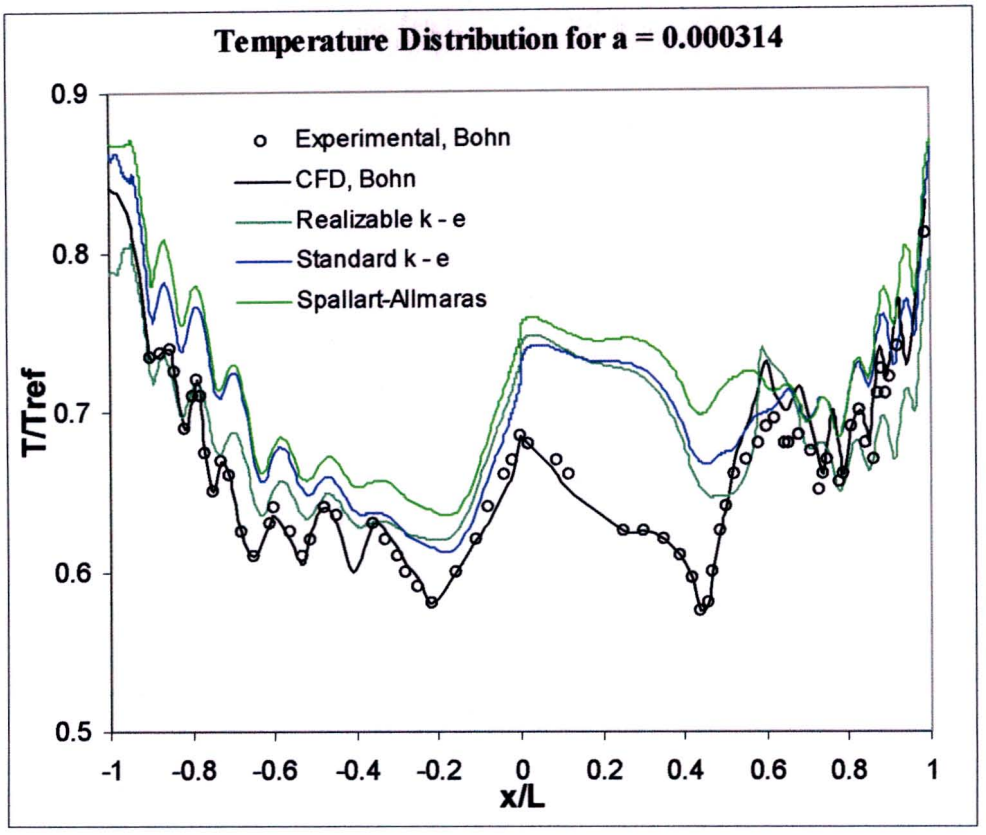

Figure 4-19: Temperature distribution from the aerodynamic analysis for a first cell size equal to 0.000314 using the Spalart-Allmaras, Realizable and Standard $k-e$ turbulence models with enhanced wall treatment

4.3.4 The Decomposed Mesh

Dorney and Davis (1992) performed a grid refinement study to investigate turbine blade heat transfer using Navier-Stokes codes. The study showed that the Baldwin-Lomax turbulence model (the same turbulence model used in Bohn's CFD analysis) could predict the heat transfer to a blade to within 2 % of the experimental data, which showed to be superior to the k - ε model.

Dorney and Davis performed a 2-D CFD study on the Langston cascade. The study showed that the best results were achieved when quad cells were used in the main flow mesh. In order to mesh the computational flow domain with quad cells, an O-ring was wrapped around the blade, this then allows controlling the mesh from the blade surface to the edge of the O-ring. This method was attempted. However, the high curvature of the blade and, more importantly, the short distance of the flow passage between the blades, made it impossible to fit a suitable O-ring around the blade.

4.3.4.1 Mesh Development

If the flow field was a perfect square or rectangle, it would be possible to create a perfectly orthogonal quad mesh, where each cell would be a much smaller representation of the flow field, and the cells would line up in straight rows and columns. The same idea can be used for the MARK II flow field. It was thought to split the flow field into many smaller faces, where each face was a carefully adjusted 4/5/6-sided region, hence making it possible to map perfect quad cells inside the regions. All the small faces will then be connected to form the entire flow field.

The first significant problem encountered was when it was attempted to split the main flow field into smaller faces at the periodic boundaries. The two periodic boundaries represent the same line in the flow field, and hence must have exactly the same node distribution and spacing. It is therefore not possible to split these boundaries. The second problem is that by having the same node distribution on the two periodic boundaries, the node spacing on the blade is then determined by the periodic boundaries. When a structured quad grid is used for the main flow mesh, the cells are built onto the boundary layer mesh and the columns are projected from the blade surface onto the periodic boundaries. Therefore, when considering the top periodic boundary (shown in Figure 4-2), the amount of nodes present on the top periodic boundary will be equal to the amount of nodes present on the suction surface of the blade (this is illustrated in Figure 4-20 below).

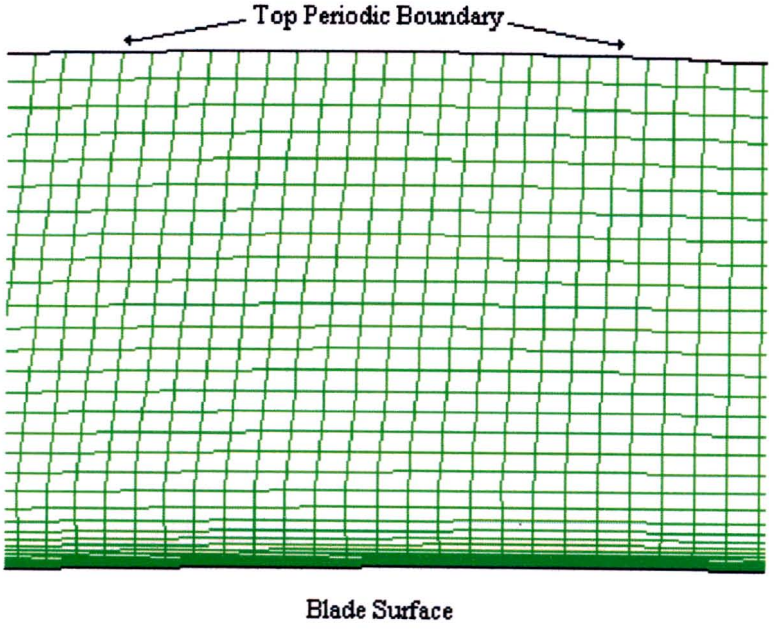

Figure 4-20: Structured Quad mesh showing that the blade surface and top periodic boundary have the same amount of nodes

This is not the problem, remembering that both the periodic boundaries have exactly the same node distribution; hence the pressure surface of the blade will have the same node distribution as the bottom periodic boundary. As a result, both the surfaces of the blade as well as both the periodic boundaries will have the same amount of nodes. The problem is that it is vital to be in control of the node spacing on the blade surface. The suction side of the blade is far longer than the pressure side and hence will require more nodes in order to achieve even node spacing around the entire blade. It is therefore impossible to achieve this if the main flow mesh is mapped from the boundary layer mesh edge to the periodic boundaries.

Mapping the main flow mesh from the boundary layer mesh edge to just before the periodic boundaries solved the problem, as shown in Figure 4-21. The thin strips next to the periodic boundaries were then meshed with an unstructured quad mesh, this then allows control of node spacing on the blade surface without having to create the same node distribution on the periodic boundaries. All the other faces in the main flow mesh had a structured quad mesh. The justification for having an unstructured quad mesh next to the periodic boundaries is that the flow in these parts is furthest away from the blade and will have very little effect on the flow conditions at the boundary layer.

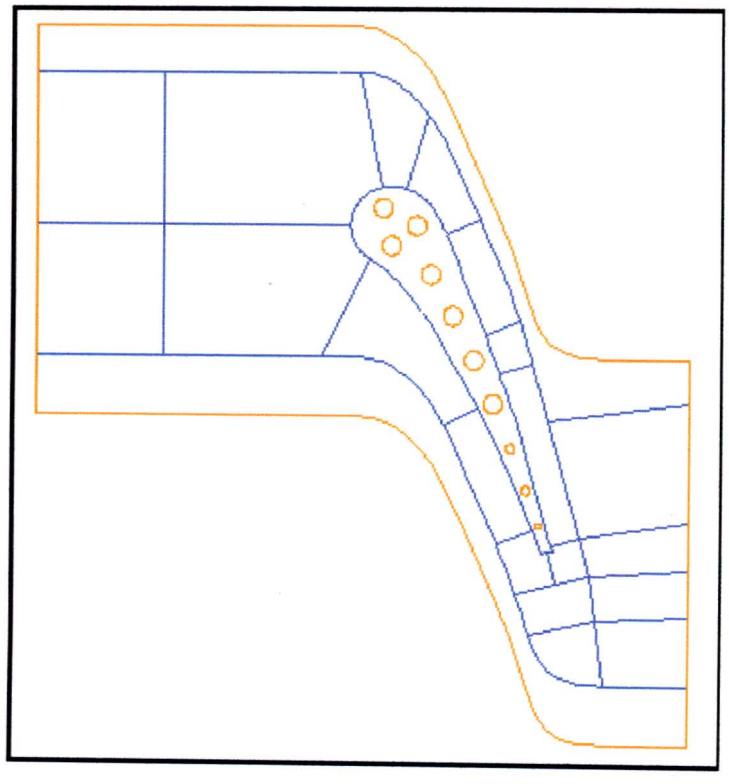

Figure 4-21: The final flow field showing the solid, and decomposed region consisting of 21 faces

The shape of the flow boundaries had to be changed from the previous shape used in all the simulations so far (Figure 4-2). This was done after several attempts to decompose the previous flow shape were made, which did not result in an overall structured quad grid. After changing the shape of the flow field numerous times, the final shape can be seen in Figure 4-21. The flow field was split into 21 smaller faces, with 19 of the faces having near perfect quad cells, the other 2 being the faces next to the periodic boundaries. The most vital part of the flow field is the area in front and around the blade. The majority of time was spent in creating the most suitable grid for this area. The mesh around the blade can be seen in the figures in Appendix G.

A grid sensitivity study was performed on the decomposed mesh, in order to achieve grid independence. Alterations to the solid mesh were also performed. Boundary layer meshing was applied inside the blade surface (shown in Appendix G in Figures G-3 to G-6) as well as on the cooling holes, this was done due to the high temperature gradients that were expected at these surfaces. The mesh was also significantly refined in the entire model. The node spacing was reduced on the entire blade surface. The finest node spacing was applied to the stagnation point on the leading edge; at 44 % axial chord on the suction surface in the vicinity of the shock wave and at 94 % axial chord on the suction surface in the vicinity of the weaker shock. These shocks are evident from the contour plots of static pressure in Appendix F.

Through all the grid refinements, grid independence was achieved when the main flow mesh consisted of 88916 cells and the solid mesh of 21098 cells, adding up to a total of 110014 cells for the entire model. Having such a large amount of cells in the computational domain caused the computational time to increase to roughly 4 hours per simulation. Figure 4-22 shows the EquiAngle values for the decomposed mesh. There are 106042 cells in the domain that have an EquiAngle value between 0 and 0.3, which accounts for 96.38 % of all the cells. These cells are considered to be near-perfect quad cells and cause no inaccuracy due to skewness. The remaining 3972 cells have an EquiAngle value between 0.3 and 0.6, where the majority of these cells lie next to the periodic boundaries and hence do not have an effect on the flow conditions around the blade. The worst cell had a value of 0.5993 and was situated near the trailing edge next to the bottom periodic boundary.

The results of the simulations for the two boundary layers investigated using the decomposed mesh differed by less than 1 %. The results presented in the next section are those for a boundary layer mesh with the first cell size = 0.00001.

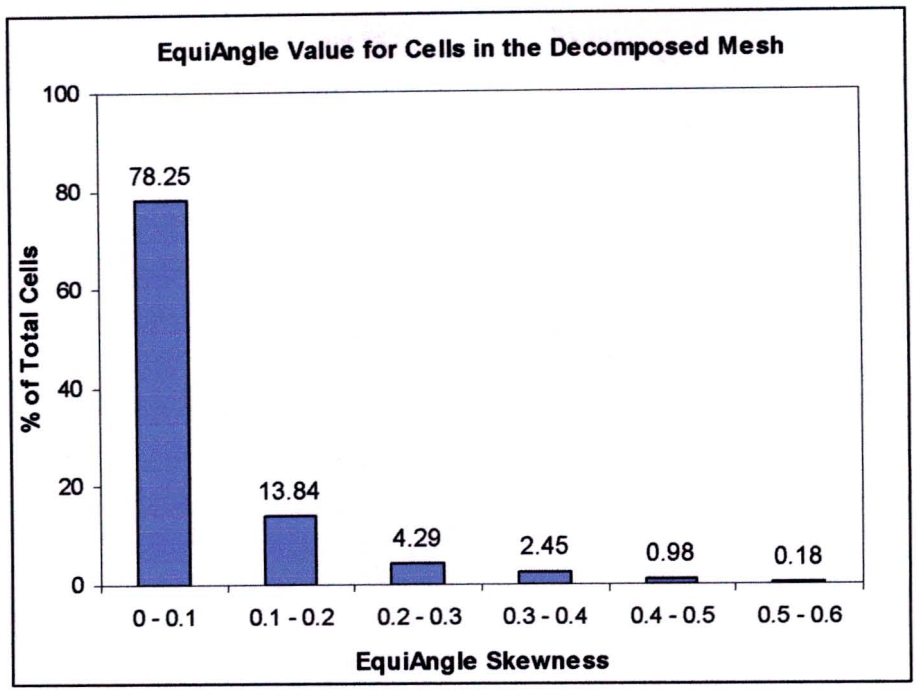

Figure 4-22: EquiAngle values for all the cells in the decomposed mesh as a % of the total cells

4.3.4.2 Pressure Results for the Decomposed Mesh (Grid 3)

The results for the pressure distribution were again exceptionally well predicted. Figure 4-23 shows the pressure results for the Spalart-Allmaras turbulence model. All three turbulence models performed equally well, it is therefore only necessary to present one of the results. On the pressure side ($-1 < x/L < 0$), the flow on the surface begins to slowly increase in velocity from the stagnation point causing the gentle drop in static pressure up to 70 % axial chord. Thereafter, the flow rapidly accelerates through the reducing blade passage throat area, causing the steep drop in pressure over the last 30 % axial chord of the blade pressure surface and the first 40 % axial chord of the suction surface. The increase in velocity on the pressure surface can clearly be seen in Figure H-1, where the velocity vectors go from dark blue (35 m/s) to light blue (141 m/s) and rapidly to dark green (493 m/s).

The suction surface pressure prediction follows the drop in pressure down to the minimum, which corresponds to the maximum velocity of 704 m/s, corresponding to $M = 1.53$ at 44 % axial chord, as shown from the velocity vectors in Figures H-2 to H-4. From the velocity vectors it is clear that no separation is predicted, yet the flow almost instantaneously decelerates from its maximum (704 m/s) supersonic velocity, to a subsonic velocity (457 m/s) in a plane normal to the blade surface. This satisfies all the criteria to be normal shock wave.

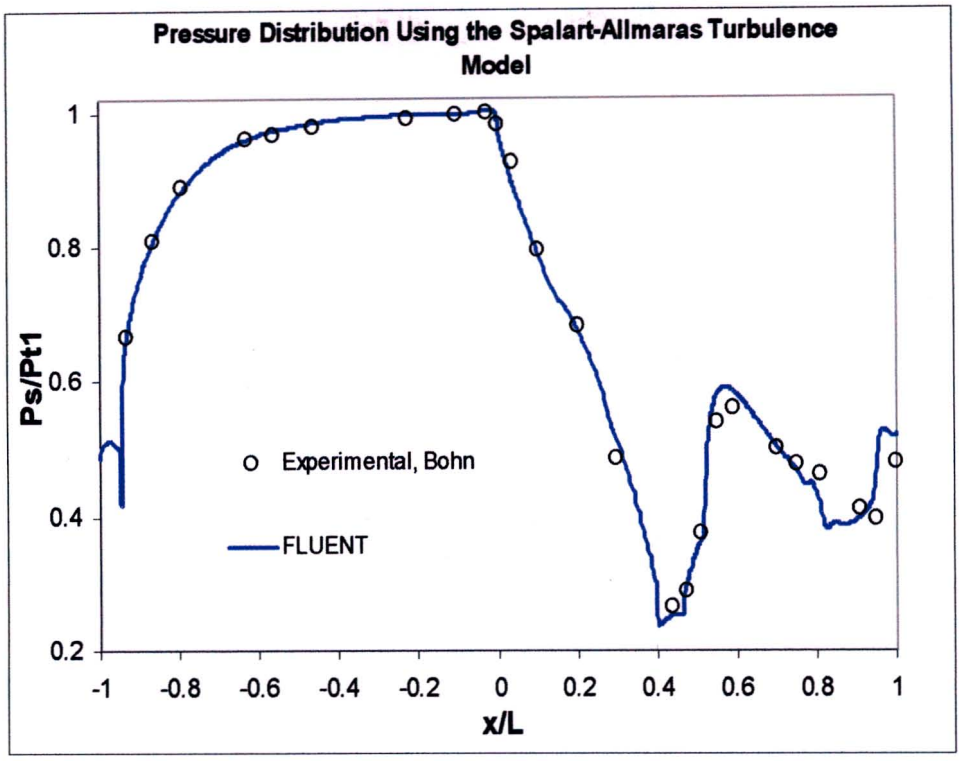

Figure 4-23: Pressure distribution from the aerodynamic analysis using the Spalart-Allmaras turbulence model for the decomposed mesh

Bohn speculated whether there was a recirculation area due to possible separation at 44 % axial chord. However, due to the limited resolution of Bohn's computational grid, no conclusion could be made. The shock in this region results in a strong increase in pressure (44 to 58 % axial chord), which is also clearly seen in Figure H-5. The flow in the boundary layer is not able to follow this increase, which usually results in a local recirculation area. Figure H-4 shows the velocity vectors in the boundary layer, which slow down to 35 m/s after the shock on the blade surface, but stay attached to the blade.

It was thought to check for separation by checking the angle of the flow of the velocity vectors on the blade surface. Figure 4-24 shows the angle of the flow around the suction surface of the blade relative to a normal Cartesian axis. Just before the shock wave, the flow on the blade surface is inclined at -70°, this position corresponds to 3.2 cm in Figure 4-24 (42 % axial chord). At the shock wave the flow changes direction and flows at an angle of -30°, while the blade is still inclined at -70°. It can be said that the flow is on the verge of separating, but manages to stay attached. Separation would occur if the flow angle were more than 90° relative to the blade surface (20° in Figure 4-24). It can therefore be concluded that no separation/recirculation occurs due to the shock wave.

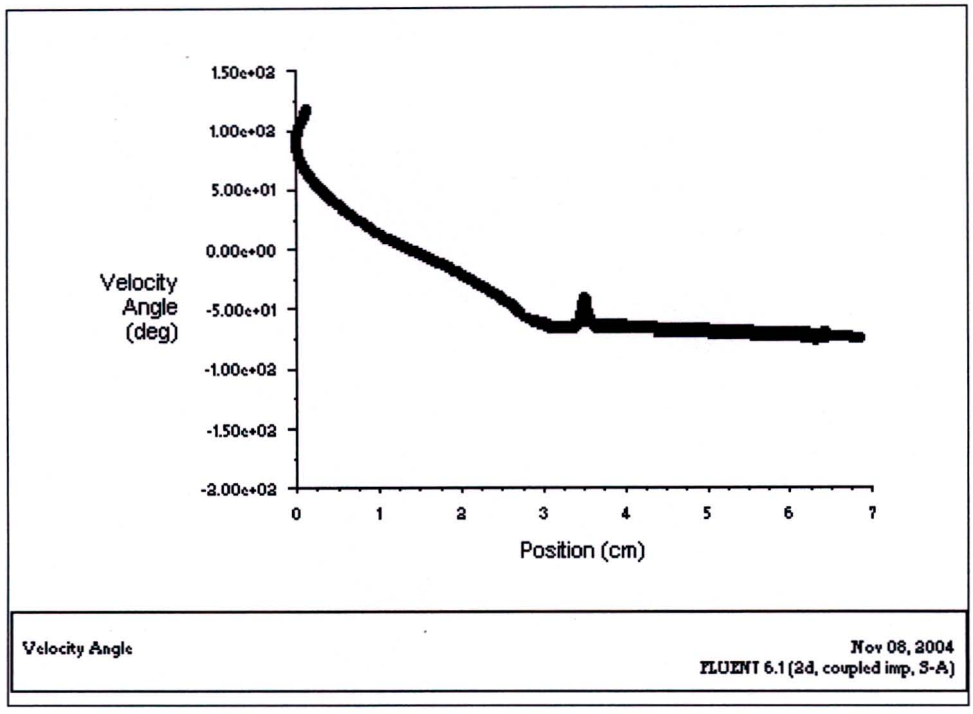

Figure 4-24: Angle of the flow around the suction surface of the blade

Between 42 and 44 % axial chord, the pressure ceases to drop but continues thereafter. The small region of no change in pressure corresponds to $Re_x \approx 4.4 - 4.8$ E 05. For a flat plate, Incropera and DeWitt (1996) give the critical Reynold's number $Re_x = 5$ E 05. It can thus be argued that the critical Reynold's number indicates transition of the boundary layer from laminar to turbulent. From 58 % axial chord after the shock wave to 90 % axial chord FLUENT predicts the decrease in pressure slightly faster than the experimental. The weak trailing edge shock wave is predicted slightly early, with the difference between the FLUENT prediction and the experimental being 5 % axial chord length. Figure H-6 shows the velocity vectors at the trailing edge shock, where the Mach number decreases from 1.22 before the shock to 0.92 after the shock.

Nealy et. al. (1984) performed pressure experiments with Mexit = 0.75 and Mexit = 1.04 for the same configuration. For completeness, the predicted FLUENT results are shown in Figures 4-25 and 4-26, respectively. For the Mexit = 0.75 case, FLUENT under predicts the minimum pressure on the suction side, but predicts the pressure recovery due to the shock very well. Identical trends discussed for the Mexit = 0.98 case are seen in the Mexit = 1.04 case. It can be concluded that all three turbulence models investigated do an excellent job in resolving the flow field. It must also be noted that a boundary layer with a first cell size relating to $y^+ \leq 1$ is necessary to correctly predict the surface pressure distribution.

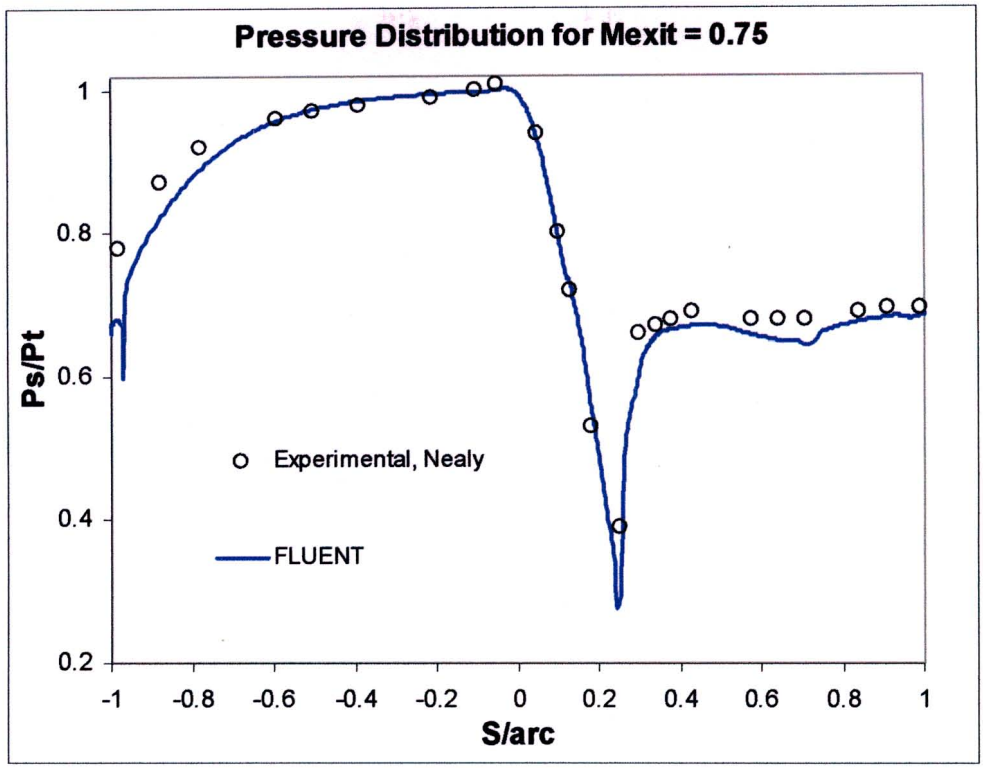

Figure 4-25: Pressure distribution from the aerodynamic analysis using the Spalart-Allmaras turbulence model for an exit Mach number = 0.75

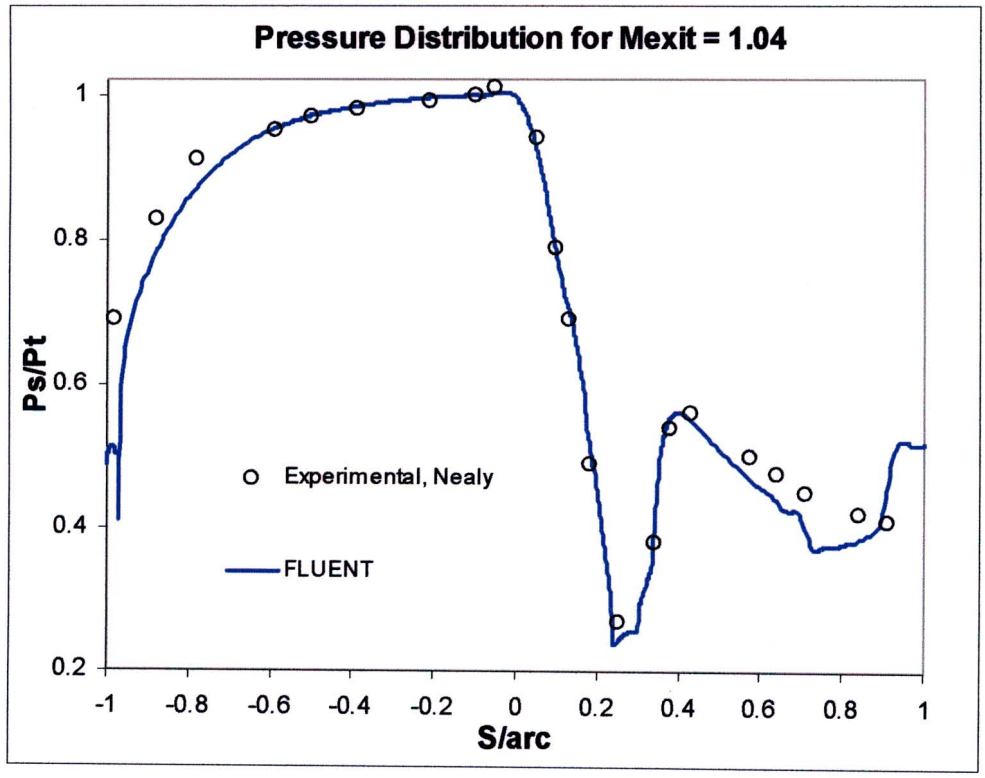

Figure 4-26: Pressure distribution from the aerodynamic analysis using the Spalart-Allmaras turbulence model for an exit Mach number = 1.04

4.3.4.3 Temperature Results for the Decomposed Mesh

The results from the three turbulence models investigated, all show a vast improvement in predicting the temperature distribution in the turbulent affected region. However, none could correctly predict the heat load in the laminar region around the leading edge. The surface temperature distribution for the Spalart-Allmaras turbulence model is shown in Figure 4-27.

On the pressure side of the blade, the temperature at the stagnation point in the laminar region is over predicted by 8 %. The over prediction decreases to zero at 18 % axial chord, where transition to turbulent flow in the boundary layer occurs at roughly 22 % axial chord, which results in a temperature increase from 22 % to 36 % axial chord. Unlike the suction side, where transition is primarily Mach number influenced due to the shock wave, the pressure side exhibits an increased tendency towards transition as the Reynold's number is elevated. From 36 % axial chord to the trailing edge, there is an increase in temperature, which is exceptionally well predicted by FLUENT, where a local maximum can always be observed in between two cooling holes and a local minimum in the vicinity of a cooling hole.

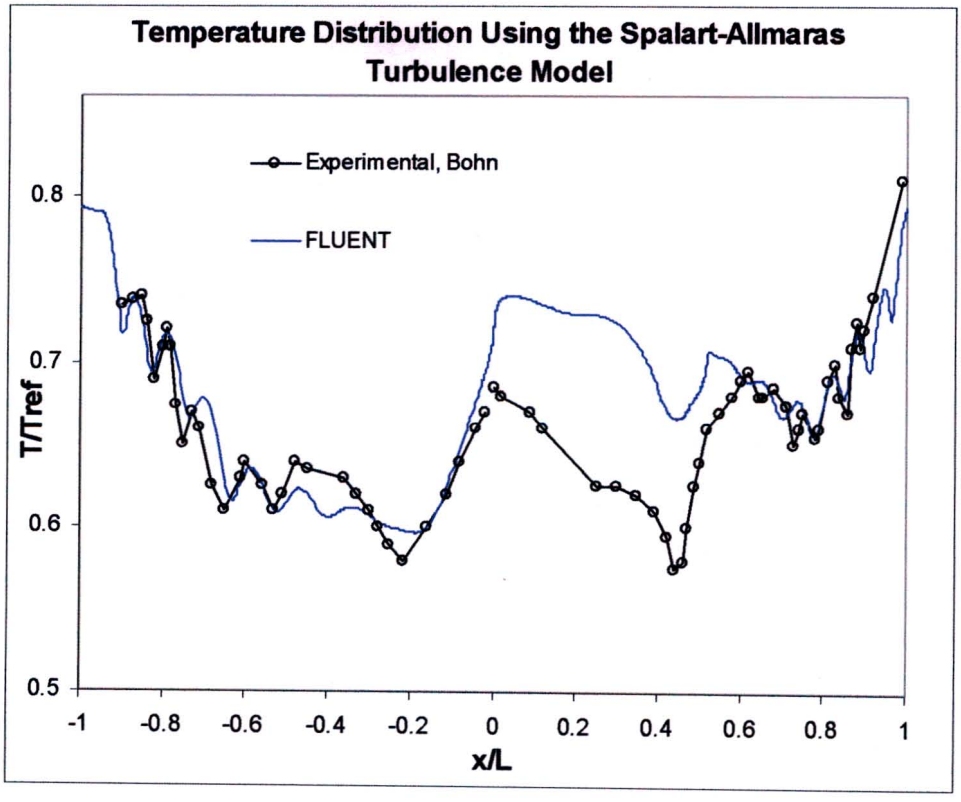

Figure 4-27: Temperature distribution from the aerodynamic analysis for the Spalart-Allmaras turbulence model using the decomposed mesh

On the suction side of the blade, from the stagnation point, there is a steady decrease in temperature to 42 % axial chord, which encompasses the entire laminar region on the suction side. The large positive pressure gradient in this area (shown in Figure 4-23) caused by the rapidly accelerating fluid due to a smaller distance of the channels from the surface, as well as the decrease in fluid temperature (shown if Figure H-7) cause the temperature to decrease in the laminar region. This effect is seen in Figure 4-27 on the suction and pressure side, where a minimum surface temperature is reached on both sides. This effect can be observed from Bohn's experimental results. The Spalart-Allmaras model shows an over prediction of 12 % on the suction side in the laminar region, with some hint of a drop in temperature prior to the shock.

At 44 % axial chord the shock leads to a steep increase in temperature, the deceleration of the flow results in a thickening of the boundary layer and, as described before, transition to turbulent flow. Due to the turbulent flow, the temperature increases to a maximum at the trailing edge. The arrangements of the cooling holes result in the local maxima and minima, as described for the pressure surface. The Spalart-Allmaras model again predicts the temperature exceptionally well in the turbulent region on the suction side.

Firstly, it must be noted that the change in computational grid for the main flow, from an unstructured quad mesh to a fully structured quad mesh, resulted in accurate temperature prediction by the Spalart-Allmaras turbulence model for the turbulent regions on the blade. The deviation from the experimental results was roughly 1 % for the turbulent regions. The model over predicted the temperature in the laminar region by an average of 10 %. It can thus be concluded that even though the Spalart-Allmaras turbulence model cannot accurately predict transition or the temperature distribution in the laminar region, it shows excellent prediction for turbulent flow.

The results predicted by the Standard $k - \varepsilon$ model with enhanced wall treatment, showed similar results to those predicted by the Spalart-Allmaras model. Again the temperature prediction showed good agreement with the data in the turbulent regions, but not in the laminar regions. The temperature prediction by the Standard $k - \varepsilon$ model can be seen in Figure 4-28, where the stagnation point temperature is over predicted by 12 %. On the pressure side the initial drop in temperature is predicted earlier than the experimental, where the minimum temperature is under predicted by 3 % at the correct location. The model under predicts the data by 5 % until 58 % axial chord, from there on the fully turbulent region is correctly predicted to the trailing edge.

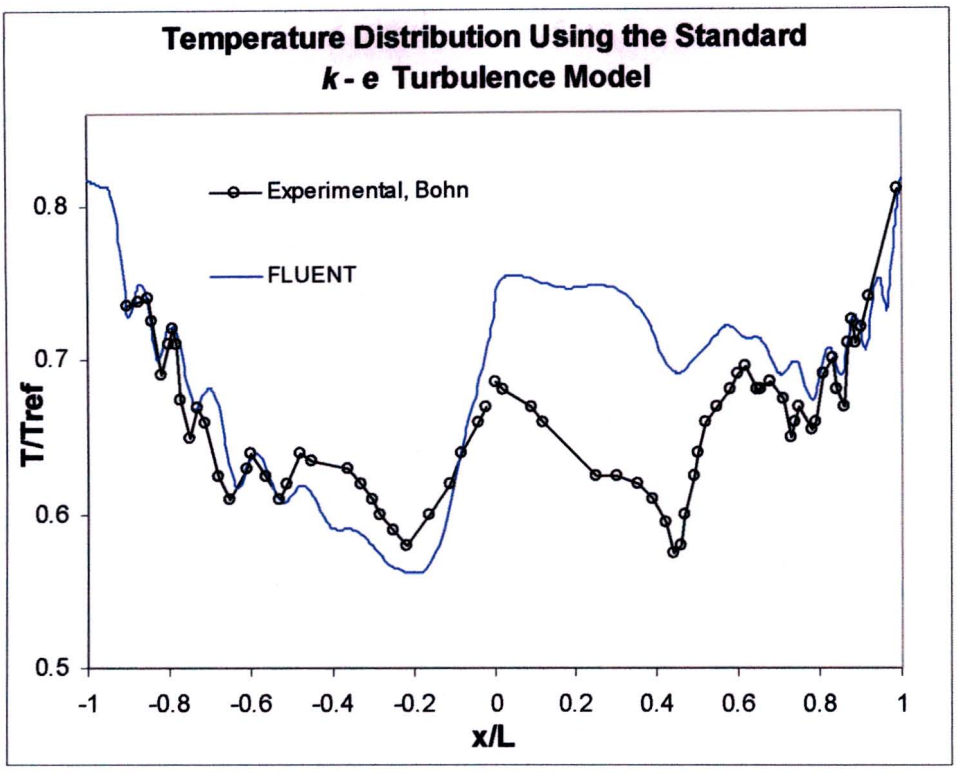

Figure 4-28: Temperature distribution from the aerodynamic analysis for the Standard k- ε turbulence model with enhanced wall treatment using the decomposed mesh

On the suction side, the model over predicts the temperature by an enormous 12 % in the laminar region. The steep increase in temperature due to the shock wave is also not properly modelled. The model does not accurately predict the temperature at the start of the turbulent region. Only once the flow is highly turbulent in nature at roughly 80 % axial chord, does the prediction correlate to the data, this trend is also seen on the pressure side of the blade.

From the results it can be argued that the Standard k – ε model with enhanced wall treatment predicts the temperature in the laminar regions slightly worse (by 2 %) than the Spalart-Allmaras model. Both models show no capability of predicting transition on the suction side due to the shock. The Standard k – ε model can only accurately predict the temperature in the fully turbulent region, where as the Spalart-Allmaras model accurately predicts the temperature from the start of the turbulent region.

The temperature distribution predicted by the Realizable k – ε model with enhanced wall treatment is shown in Figure 4-29. This is the only model that showed some potential in the previous results in predicting the transition on the suction side. At the stagnation point, the temperature is over predicted by 10 %, this trend is consistent in all three turbulence models.

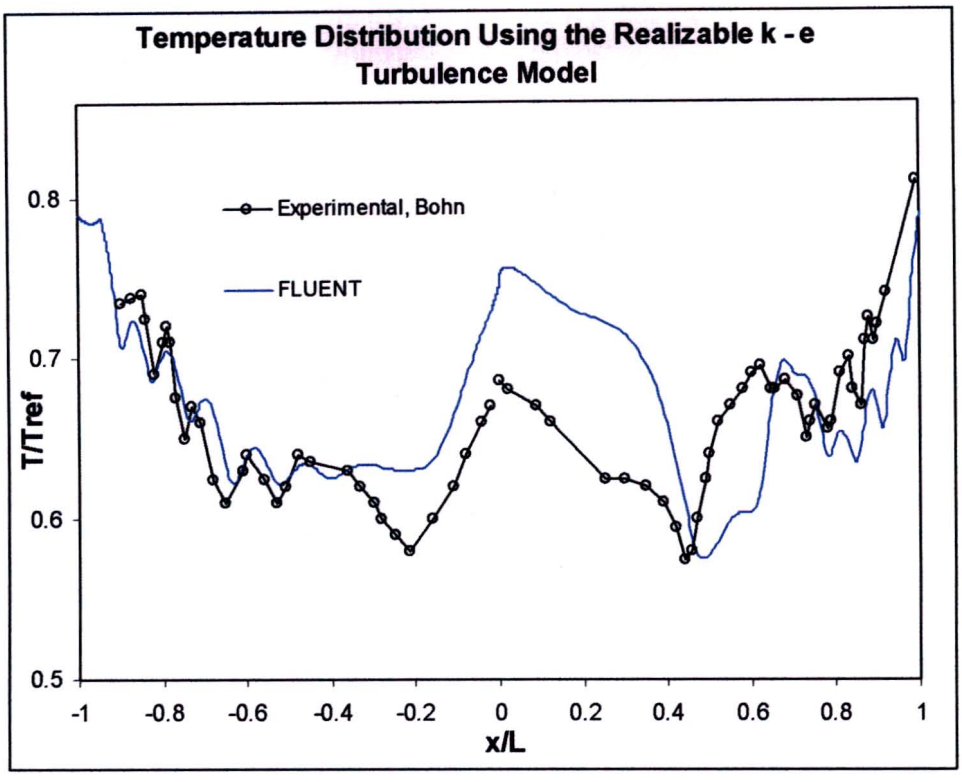

Figure 4-29: Temperature distribution from the aerodynamic analysis for the Realizable k – e turbulence model with enhanced wall treatment using the decomposed mesh

On the pressure side, from stagnation point to 38 % axial chord, the data is consistently over predicted by 8 %. This model shows the worst prediction for the laminar region on the pressure side. Thereafter the model shows excellent prediction in the turbulent region. On the suction side, the laminar region is again over predicted by 10 %, the point of transition is however fairly accurately predicted. The lowest temperature value at which transition occurs is accurately predicted, but the transition point is predicted slightly late with the difference between the FLUENT prediction and the experimental being 4 % axial chord length. The steep increase in temperature due to the shock wave is predicted but at the incorrect position. The predicted peak temperature value corresponds to the data but is out by 6 % axial chord length. The prediction for the entire turbulent region has the exact trend as the experimental, but is 'shifted' by 6 % to 8 %.

The computational grid in the vicinity of the shock wave was further refined, but the results were unchanged. Based on all the simulations performed, the Realizable k – ε model with enhanced wall treatment is the only model that shows any likelihood of predicting transition on the suction side. All three models showed inadequate prediction in the laminar region. The Spalart-Allmaras model showed the best prediction in the turbulent region and was marked as the turbulence model for the validation.

The failure of the FLUENT turbulence models to predict the correct temperature was put down to the fact that Navier-Stokes turbulence models are formulated for turbulent flows and hence assume turbulent flow over the entire blade surface. Another possibility was that the thermal boundary layer was not resolved in the laminar regions. Open literature suggests that the thermal boundary is usually about 10 % thicker than the velocity boundary layer, in which case, the thermal BL would have been resolved. Boundary layers are however very thin in laminar regions. It was therefore decided to calculate the thermal BL to find out its thickness in relation to the velocity BL. Kays (1966) defines the ratio of boundary layer thickness for a flat plate in the laminar region as:

$$\frac{\delta}{\delta_t} \approx Pr^{\frac{1}{3}} \qquad \text{Eq 4-7}$$

Where the velocity boundary layer thickness δ is known from FLUENT along with the Prandtl number, which is 0.845. Which then results to the following ratio:

$$\delta \approx 0.945\delta_t \qquad \text{Eq 4-8}$$

From the estimate it can be seen that the thermal boundary layer δ_t is slightly larger than the velocity boundary layer. It can therefore be argued that, because the velocity boundary layer was modelled, the thermal boundary layer must have therefore also been captured.

4.3.4.4 The Laminar Model

With all the immense research activity into turbulence modelling, many researchers struggle to compute the heat load to a blade in the laminar region. There is one model in FLUENT that is usually overlooked, namely the Laminar model, which, as its name suggests, is used for laminar flow.

FLUENT defines laminar flow as an organised flow, which can be streamlined, where the viscous stresses dominate over the fluid inertia stresses. For no-slip wall conditions, FLUENT uses the property of the flow adjacent to the wall/fluid boundary to predict the shear stress on the fluid at the wall. In the laminar flow model, this calculation simply depends on the velocity gradient at the wall, while in turbulent flows, approaches such as the near wall treatment are used, which solve for turbulence production and turbulent viscosity.

In the laminar flow, the wall shear stress τ_w is defined by the normal velocity gradient at the wall as:

$$\tau_w = \mu \frac{\partial u}{\partial y} \qquad \text{Eq 4-9}$$

Where y is the distance from the adjacent wall and μ the dynamic viscosity of the fluid. Fluent recommends that the grid be sufficiently fine to accurately resolve the boundary layer, this has been achieved through grid independence in Grid 3. The viscous laminar model was set up using the same boundary conditions that were used in all previous simulations. Employing the simple Laminar model significantly reduced the computational time. The results of the simulation are shown below in Figure 4-30.

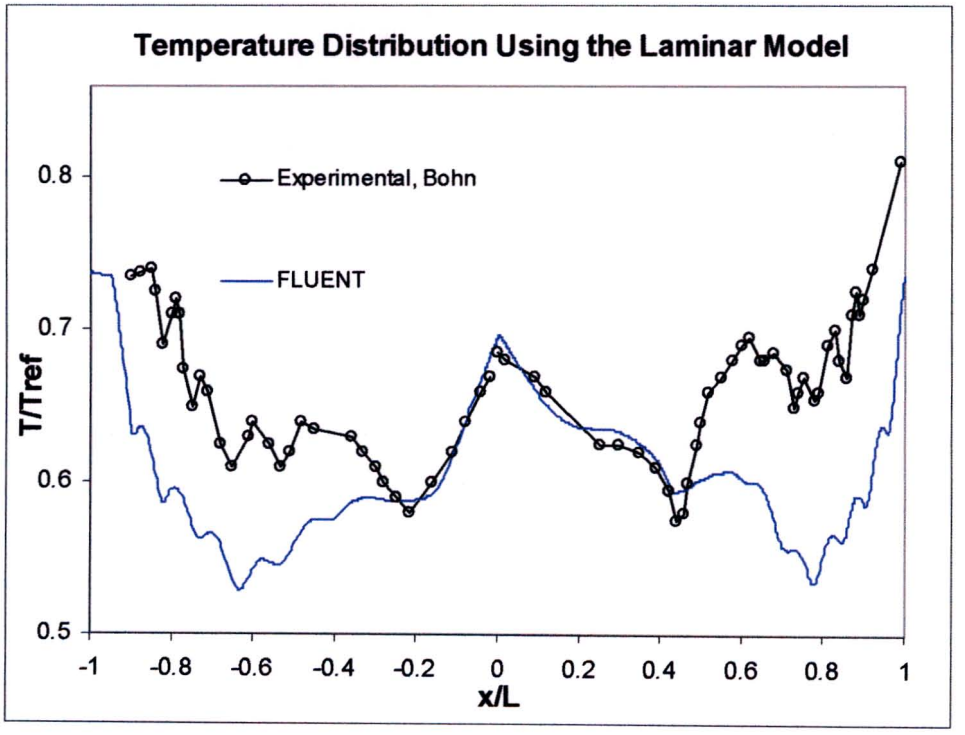

Figure 4-30: Temperature distribution from the aerodynamic analysis for the Laminar model using the decomposed mesh

The model shows excellent temperature prediction in the laminar region. The stagnation point temperature is over predicted by a mere 1 %. On the pressure side, the temperature prediction is exact with the data in the laminar region up to 17 % axial chord where transition occurs. As expected, the model thereafter under predicts the data as it assumes laminar flow and does not model turbulence, which increases heat transfer to the blade. The same trend is observed on

the suction side, where the prediction again follows the data accurately up to 44 % axial chord where transition due to the shock wave occurs. The same under prediction is then observed on the suction side in the turbulent region. The contours of static pressure and temperature for the Laminar model are shown in Figures F-11 and F-12, respectively. From the figures the under prediction for both the temperature and pressure can clearly be seen in the turbulent regions. The model also shows no capability of modelling the shock wave on the suction side.

The Laminar model and the Spalart-Allmaras turbulence model can now be combined into a single graph, where the prediction for the laminar region can be taken from the Laminar model and the prediction for the turbulent region from the Spalart-Allmaras turbulence model. Figure 4-31 shows both the models, which clearly shows where each model is capable of predicting the temperature.

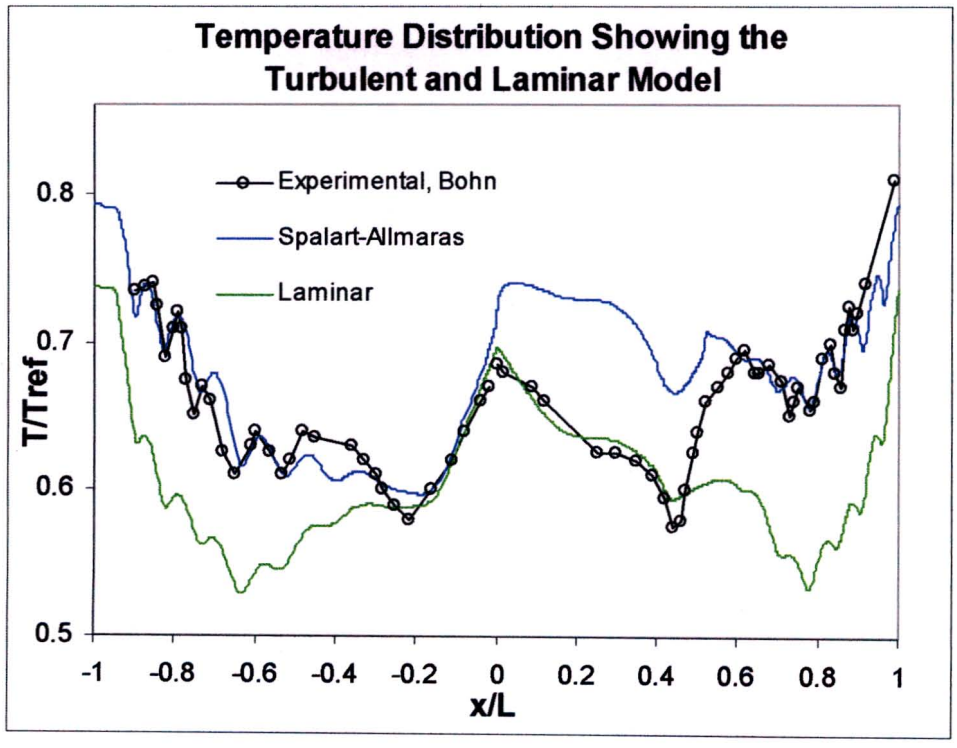

Figure 4-31: Temperature distribution from the aerodynamic analysis showing both the Spalart-Allmaras and Laminar model using the decomposed mesh

Figure 4-32 shows the product of combining the two models into one graph. On the pressure side, from the leading edge stagnation point to the transition point at 17 % axial chord, the prediction from the Laminar model is combined with the prediction from 17 % to 100 % axial chord from the Spalart-Allmaras turbulence model. On the suction side, from the stagnation

point to the transition point at 44 % axial chord, the prediction from the Laminar model is combined with the prediction from 44 % to 100 % axial chord from the Spalart-Allmaras turbulence model.

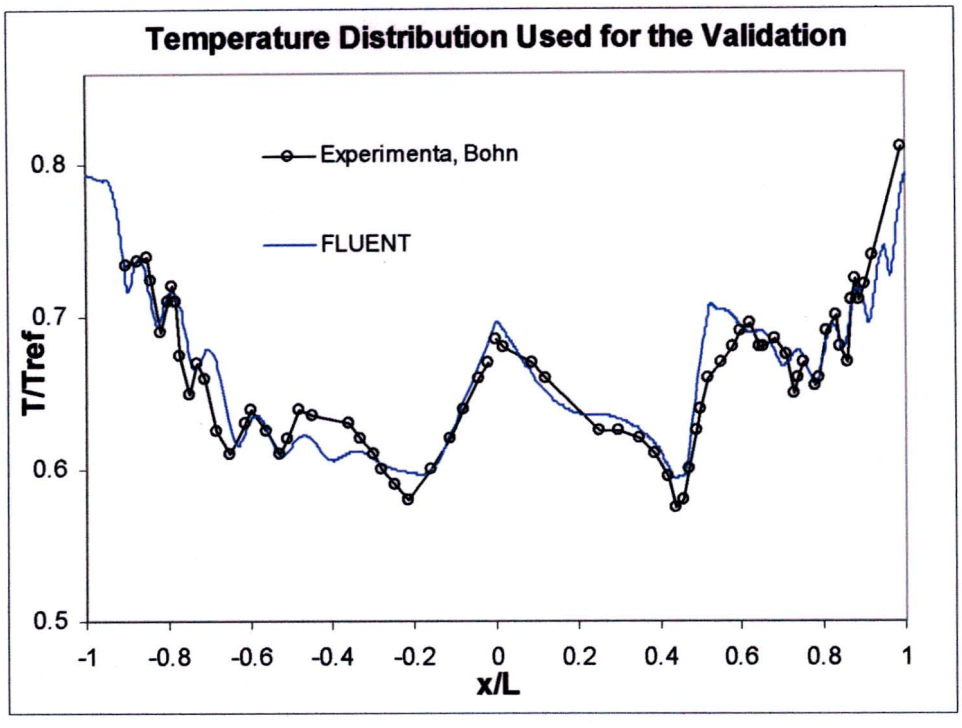

Figure 4-32: Temperature distribution from the aerodynamic analysis showing the combined Spalart-Allmaras and Laminar model using the decomposed mesh

The combined model shown in Figure 4-32 is the model that validates the data and can now be used in the thermal analysis to predict the resulting thermal stresses. Figure 4-33 shows the combination of the Standard $k - \varepsilon$ model with enhanced wall treatment and the Laminar model, while Figure 4-34 shows the combination of the Realizable $k - \varepsilon$ model with enhanced wall treatment and the Laminar model. Both the Figures show acceptable results, however, Figure 4-32 will be used to in the thermal stress calculations.

The procedure of combining the two models can be extended to any blade configuration, and is possible if the transition points on the blade are known. These can be calculated with good accuracy, as shown. Even if the approximate position can not be calculated, the turbulence models give some hint as to where transition occurs. The laminar region can be seen where the turbulence models highly over predict the experimental data, and vica versa with the Laminar model.

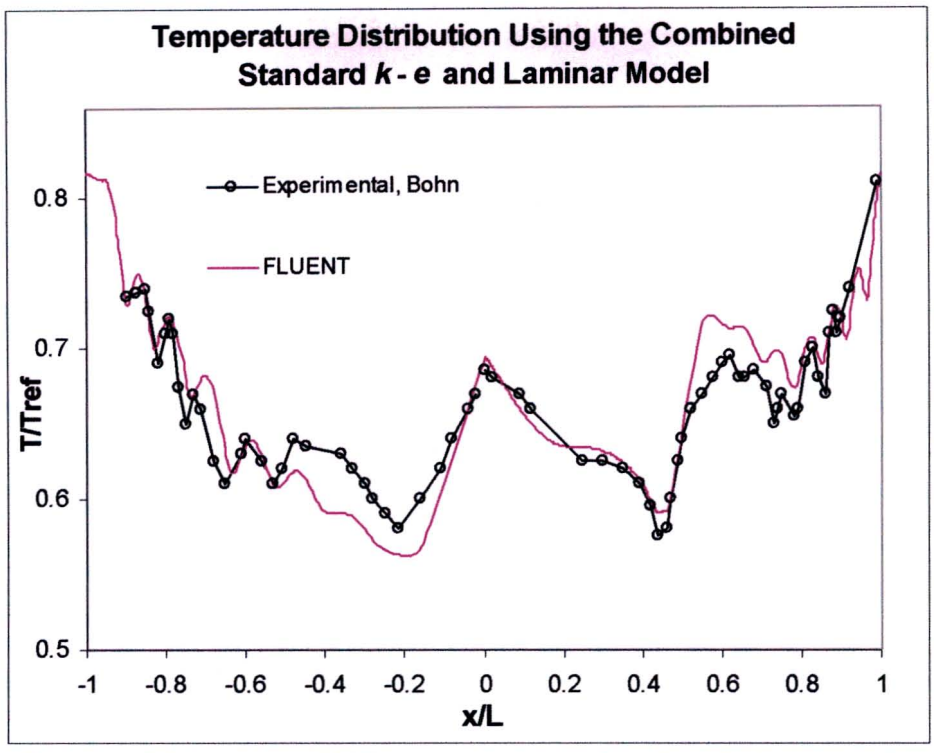

Figure 4-33: Temperature distribution from the aerodynamic analysis showing the combined Standard *k*- ε turbulence model with enhanced wall treatment and the Laminar model using the decomposed mesh

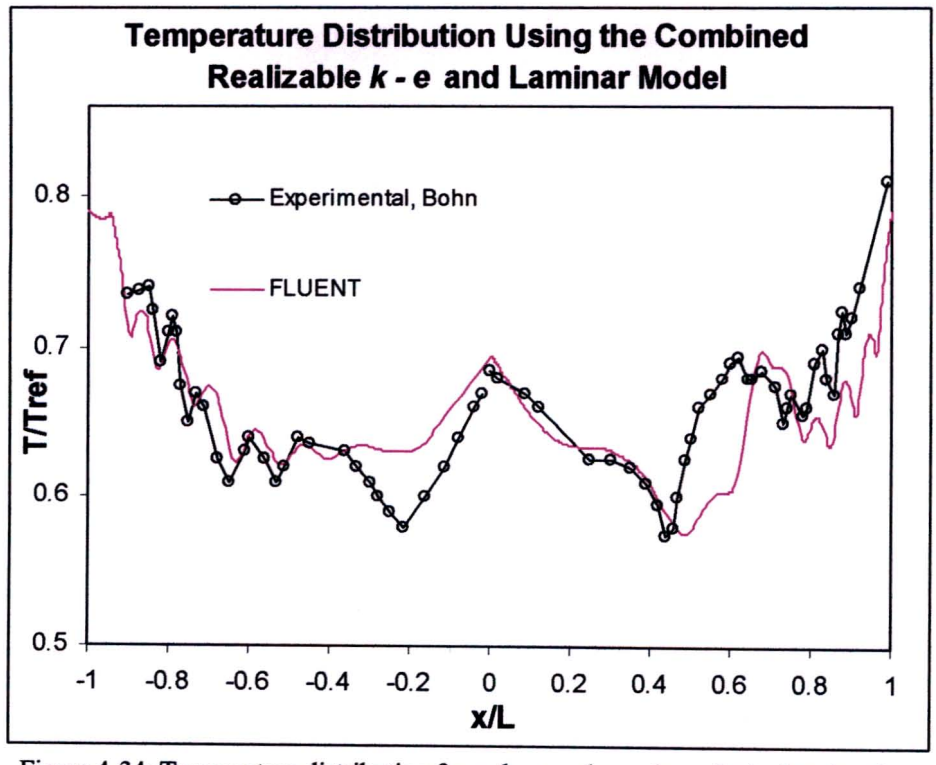

Figure 4-34: Temperature distribution from the aerodynamic analysis showing the combined Realizable *k*- ε turbulence model with enhanced wall treatment and the Laminar model using the decomposed mesh

4.3.4.5 Heat Transfer Results

Bohn did not perform heat transfer measurements on the MARK II NGV, the study was rather aimed at predicting the temperature distribution. It is also unclear as to how Bohn calculated the heat transfer, as no mention regarding the matter is made. Figure 4-35 shows Bohn's heat transfer calculation compared to that predicted by FLUENT, where Href = 1135 W/m^2K.

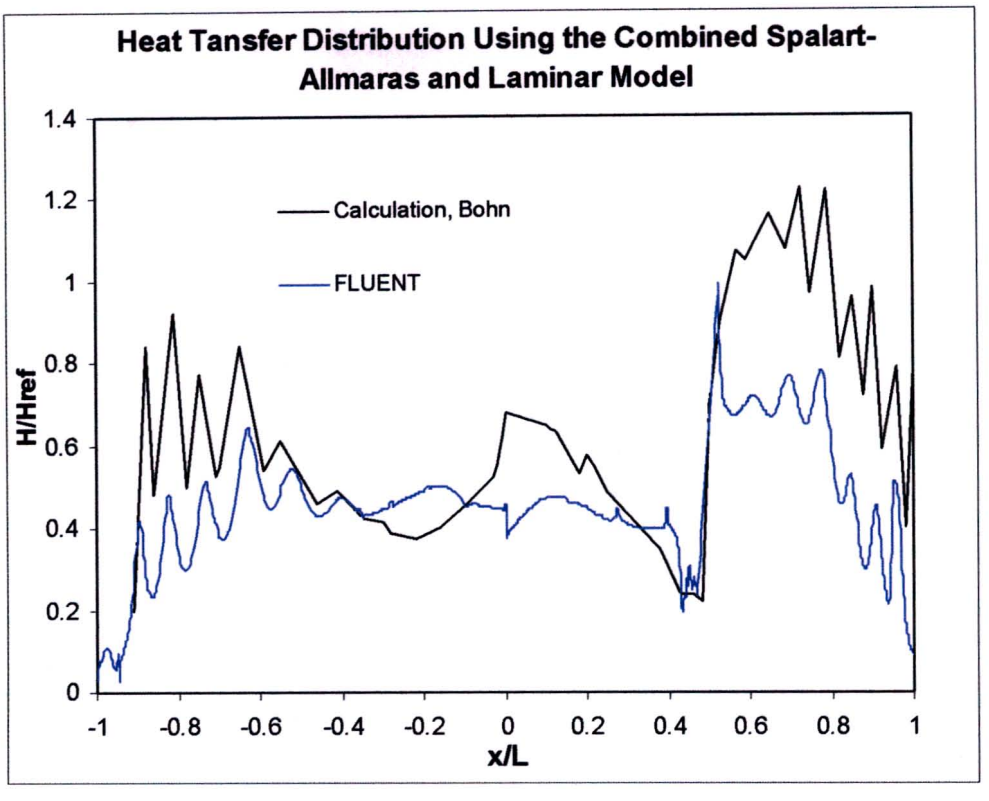

Figure 4-35: Heat transfer distribution from the aerodynamic analysis showing the combined Spalart-Allmaras and Laminar model using the decomposed mesh

The development of the heat transfer along the blade surface is analogous to that of the temperature. The heat transfer distribution predicted by FLUENT follows similar trends to Bohn's calculation. At the leading edge stagnation point, the predicted heat transfer is lower than Bohn's calculation. On the suction side up to 44 % axial chord, both graphs decrease to the same value. Bohn's graph however decreases with a steeper gradient and is considered to be more accurate in this region, as it correlates more accurately to the decrease in temperature in this region. The heat transfer spike is accurately modelled. The prediction there after

follows the same trend as Bohn's calculation, where both the data decrease to the trailing edge, the values are, however, lower. It is uncertain which trend is more accurate.

On the pressure side, from the stagnation point to the transition point at 22 % axial chord, Bohn's calculation again shows a decrease in the heat transfer, where as FLUENT predicts an area of little change in the heat transfer. Here again, Bohn's data follows the trend seen in the temperature more accurately than the FLUENT prediction. There after FLUENT predicts the decrease in the heat transfer spikes (caused by the cooling holes) where as from Bohn's calculation, the heat transfer spikes show very little decrease up to the trailing edge.

It can be argued that in the laminar region Bohn's calculation is more accurate, where the difference between the two graphs in the laminar region is 9 %. No conclusions can be drawn from the heat transfer distribution in the turbulent region. A proper analysis can only be made if there are experimental results to compare to. Comparing two codes or calculations has little validation meaning or accuracy.

CHAPTER 5

FINITE ELEMENT METHOD (FEM) MODEL DEVELOPMENT

5.1 Introduction

The aerodynamic analysis showed that the temperature distribution and temperature gradients inside the blade (which are responsible for the thermal stresses) depend on the flow conditions and characteristics. The flow in the boundary layer is influenced by the cooling of the wall and the cooling mechanism is strongly affected by the flow conditions along the blade surface. Hence, the inter-dependent relationship between the aerodynamic and thermal considerations. A coupled simulation for the fluid flow along the blade profile, the heat transfer in and through the blade wall, and the determination of the corresponding stresses must be performed in order to comprehensively evaluate and understand turbine blade operation.

With the CFD model from the aerodynamic analysis accurately validated, the resulting temperature distribution on the MARK II blade surface can now be used as the boundary condition for the thermal analysis. All the results from the aerodynamic analysis, namely the temperature, heat flux and heat transfer coefficients are shown in Appendix B.

An early investigation into FEM codes led to a program called FIDAP, which forms part of the FLUENT family of numerical codes. The program is a general purpose FEM code designed for simulating inviscid and viscous flows with heat and mass transfer. The code is equipped with Fluid-Solid-Interaction (FSI), which refers to problems where deformations and stresses in a solid body are the result of the action of a surrounding flow field. FIDAP uses FEM formulation for the governing equations of the problem where the fluid and solid equations are coupled by a common variable, this being the temperature at the common wall i.e. the blade surface.

Although FIDAP is capable of solving both flow and structural problems, it is incapable of solving supersonic and transonic flows, and flows with severe changes in density. There has also not been a new release of FIDAP since the year 2001. FLUENT technical support and users at the University of Pretoria recommend not using FIDAP as it has had little success in research areas.

Bohn performed the thermal analysis using a code called MSC.MARC/Mentat. Due to licensing problems this code could not be used by the author for the analysis. However, another code that forms part of the MSC family of FEM codes was available, namely MSC.NASTRAN 2004.

NASTRAN has capabilities that include one, two and three-dimensional conduction, free and forced convection, one-dimensional advection and allows for radiation boundary conditions. The program is also capable of simulating linear and non-linear, steady state and transient thermal problems.

5.2 Problem Definition and Boundary Conditions

The FEM analysis can be divided into two parts, the thermal analysis and the mechanical analysis. In the thermal analysis, the internal blade temperature profile is resolved. The outcome of the thermal analysis is dependent on the accuracy of the applied temperature boundary conditions generated from the aerodynamic analysis. The temperature boundary conditions are vital and consist of the temperature profile on the blade, as well as the temperature profiles inside the blade on the cooling hole surfaces. The mechanical analysis resolves the corresponding thermal stresses and is dependent on the accuracy outcome of the thermal analysis, which forms the first boundary condition. The accuracy of the resulting stresses depend heavily on the material characterisation and element property definition.

The procedure for the thermal and mechanical analysis is performed in three sequential steps and can be summarized as follows:

1. Pre-processing – the development of the finite element mesh of the geometry, application of the correct material and element properties, and boundary conditions.
2. The solution – process during which the program derives the governing matrix equations from the model and solves the temperatures/stresses.
3. Post-processing – results are obtained in the form of deformed shapes and contour plots, which help to check the validity of the solution.

Unlike FLUENT that uses GAMBIT to generate the mesh, in NASTRAN the pre-processing, solution and post-processing are all performed in the same environment.

5.2.1 The Thermal Analysis

As mentioned above, the first step in creating the FEM model is to create the blade geometry and mesh. In FLUENT, the blade surface was discretized by 708 nodes. In NASTRAN the geometry of the blade surface was therefore created from 708 nodes, where each node had a coordinate position and a temperature value. The coordinates of the nodes from FLUENT were firstly used to plot points in NASTRAN that describe the blade profile. These points were than converted to nodes and assigned their temperature values. This was done so as to represent the exact temperature profile in NASTRAN that was derived in FLUENT. The same procedure was applied for the cooling holes.

5.2.1.1 Mesh Development

Bohn mentions that one of the most difficult problems is the change in computational grids in the solid region from the aerodynamic to the thermal analysis. Grid independence however shows that the mesh can change provided that it is sufficiently fine enough. An unstructured quad mesh (Grid 1) was developed that consisted of 708 nodes on the blade surface and 17453 cells in total, as shown in Figure 5-1. A close up of the mesh can be seen in Figure 5-2.

To prove the model was grid independent, another mesh was developed (Grid 2) that had 354 nodes on the blade surface, which equates to half the amount of nodes present on Grid 1. Figure I-1 shows a close up Grid 2, which contains 9674 cells in total. A tri mesh was also developed (Grid 3) that consisted of 12248 cells in total with 354 nodes present on the blade surface, which can be seen in Figure I-2. Three meshes were created to investigate whether any changes in the temperature and stress profile occurred when different meshes were applied to the model.

The results of the temperature and stress contour plots for all three meshes were the same, no difference could be found across the three models. This was to be expected since Bohn only had a total of 3212 cells in the solid region. It was nonetheless important to investigate grid independence for the FEM model. The results presented hereafter in this chapter are all for Grid 1.

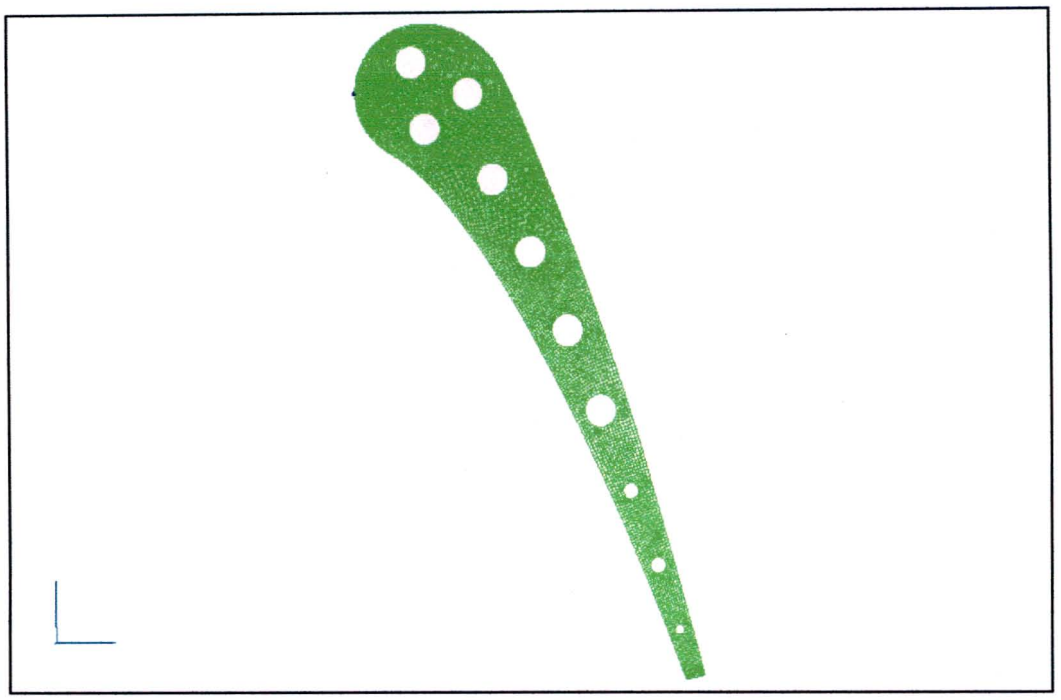

Figure 5-1: FEM computational quad mesh (Grid 1) with 708 nodes on the blade surface

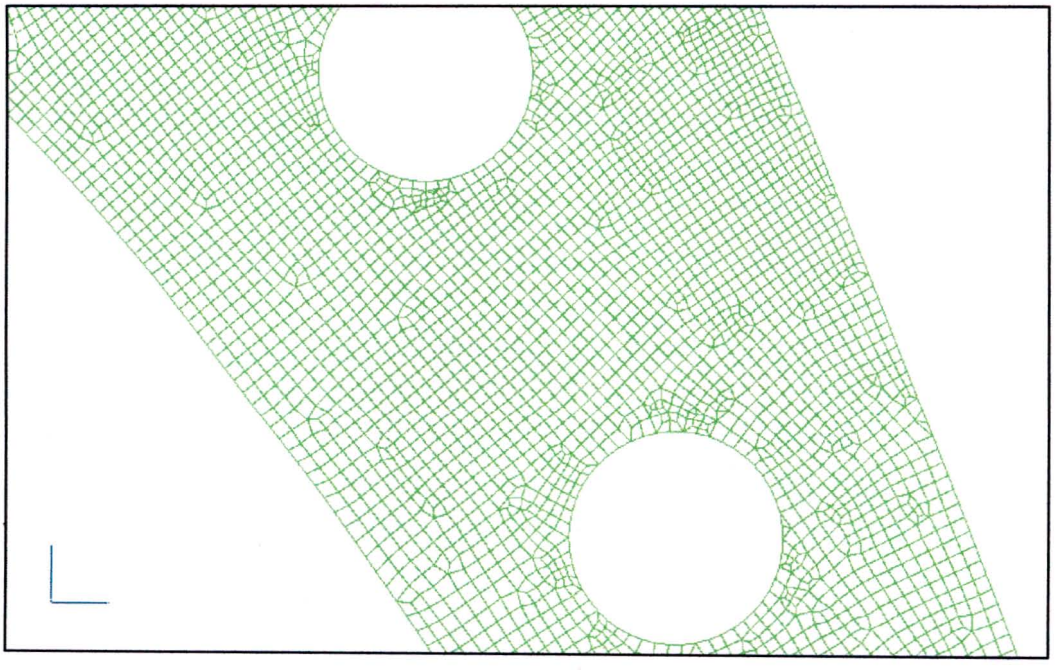

Figure 5-2: Close up of the FEM computational quad mesh (Grid 1) with 708 nodes on the blade surface

5.2.1.2 Model Specifications

Because the problem is only 2-D, and due to the material characteristics, the structural analysis in NASTRAN is modelled assuming isotropic linear elastic material behaviour. The solution strategy is based on a coupling of the equation systems for the thermal problem, the computational structural dynamics (CSD) and the dynamic mesh. The CSD applies the traction from the results of the thermal analysis (temperature distribution inside the blade) and uses the Updated Lagrangian formulation to solve the displacements of the structure.

An elastostatic model is used in the dynamic mesh to solve the mesh displacement. The governing elastodynamic equations for the CSD are the constitutive stress equations that have been modified to include thermal effects, which are solved together with the equilibrium condition for the problem. For the plain-strain condition, the equilibrium condition is shown below in Eq 5-1:

$$\sum \sigma_{zi} \cdot A_i = 0 \qquad \text{Eq 5-1}$$

Where the force in the z-direction, $\sigma_{z,}$, is zero. All the equations mentioned above are discretized by the Galerkin finite element procedure. The result is a system of non-linear, discrete matrix equations, which are solved in a sequential manner. The global matrix is decomposed into sub-matrices, each governing the nodal variables for one conservation equation. The sub-matrices are then solved in a sequential manner using the Gaussian Elimination method.

The thermal stress distribution due to the thermal loading in the blade, is modelled in the mid-span cross section using the plain-strain condition as described by Eq 5-2 below:

$$\varepsilon_z = \varepsilon_{xz} = \varepsilon_{yz} = 0 \qquad \text{Eq 5-2}$$

Where the strain in the z, xz and yz direction equals to zero. This then only allows for strain in x and y direction, with no movement of the cells in the z direction. Imposing the plain-strain condition onto the model means that the simulation represents a slice of a 3-D problem, in which the third dimension is much larger than the 2-D cross section. NASTRAN accounts for this condition by simplifying the elasticity tensor in the constitutive equation, while the thermal effects are taken into account by modifying the strain tensor.

It is vital to prescribe into NASTRAN the material properties as a function of temperature. All the thermal material properties used for the thermal analysis are given in Appendix D. The root cause of thermal stress in a material is the thermal expansion coefficient, α, which describes the change in length of a material with change in temperature. It is therefore important to model α as a function of temperature, since large temperature gradients are expected inside the blade.

The thermal conductivity, k, of ASTM 310 stainless steel is very low and as a result, large thermal stresses are expected in the blade. This material is not usually used for turbine blades, but due to its low k value it serves as a good example to demonstrate large stress distributions.

5.2.1.3 Results of the Thermal Analysis

For the thermal analysis the steady state conduction equation was solved in NASTRAN. The resulting temperature contour plot is shown in Figure I-3 and is compared to the analysis performed by Bohn in Figure I-4. From the contour plots it can be seen that the maximum temperature on the suction side is correctly predicted with a difference of 8 K (2 %) to that of Bohn's prediction. On the pressure side the maximum temperature differs to Bohn's data by 4 K (1 %). Bohn predicted a maximum temperature of 663 K at the trailing edge. The maximum temperature predicted by NASTRAN was 644 K and was also situated at the trailing edge. This difference of 19 K (3 %) also corresponds to the worst case for the entire blade.

The minimum temperature in the blade is predicted in between the second and third cooling holes, Bohn's data shows a value of 400 K while NASTRAN shows 412 K, equating to an over prediction of 3 %. The overall NASTRAN contour plot is exact to that of Bohn's, where the effect of the cooling holes can be seen as the temperature increases from the cooling holes to the blade surface. NASTRAN over predicts Bohn's data by an average of 2 % to 3 % for the entire blade.

The temperature along line AB (where line AB is shown in Figure I-6) is shown in Figure 5-3. The line AB represents the blade thickness in between the forth and fifth cooling holes. The exact position of the line is unknown and had to be estimated from Figure I-6. From Figure 5-3 it can be seen that the position of line AB was fairly accurately estimated, where the NASTRAN curve is slightly short of Bohn's curve.

The curve trend is correctly predicted through the blade, where the position at 0 meters corresponds to the temperature on the pressure surface and the position at 0.0161 m corresponds to the suction surface.

The NASTRAN curve over predicts Bohn's curve by an average of 2 %. From the plot it can be argued that the cooling on the pressure side is more efficient than on the suction side, this is evident from the steeper temperature gradient on the suction side. Ideally a uniform temperature distribution is desired inside the blade, this is because temperature gradients are known to be the cause of thermal stresses. From the plot, higher stresses can therefore be expected towards the suction side of the blade.

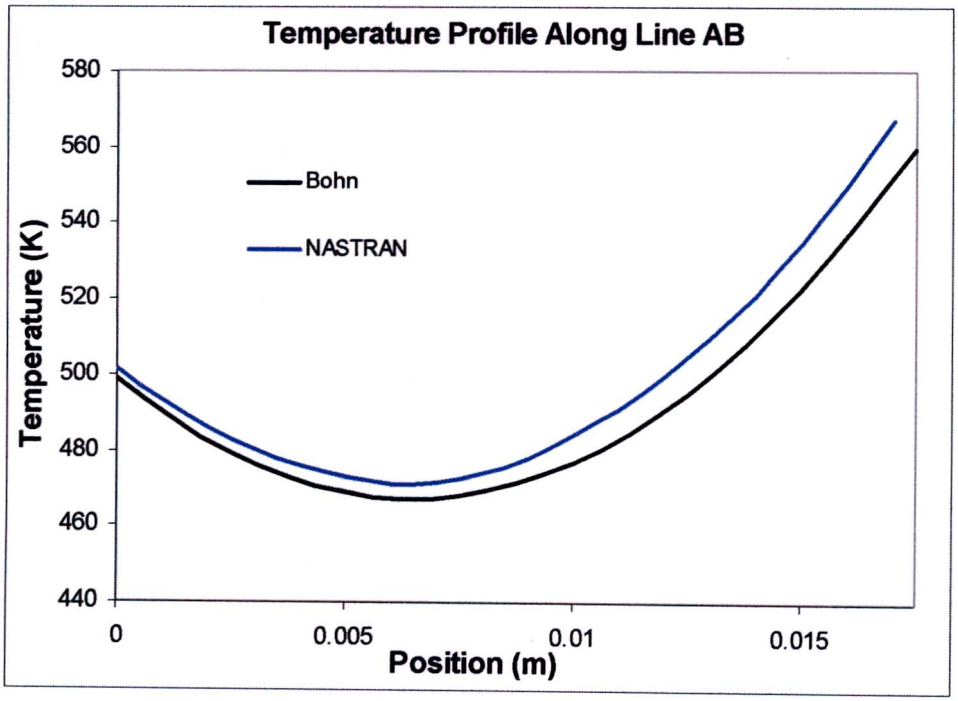

Figure 5-3: Temperature profile along line AB from the thermal analysis

5.2.2 Results of the Mechanical Analysis

The internal temperature distribution resulting from the thermal analysis was used as the boundary/loading condition for the mechanical analysis, where the resulting temperatures at all the nodes were prescribed as the loading condition. For the mechanical analysis, the grid, element and material properties were the same as those used in the thermal analysis.

The resulting contours of equivalent stress, σ_e, are shown in Figure I-5 and are compared to Bohn's contour plot in Figure I-6. As expected, the maximum stress in the blade occurs at the minimum temperature, which is located at the rim of the second cooling hole. NASTRAN predicts a σ_e of 354 MPa at this point whereas Bohn predicts 431 MPa, equating to a difference of 17.9 %.

The minimum stress inside the blade, which is located below the seventh cooling hole, is also correctly predicted. NASTRAN under predicts Bohn's value by 5 MPa. In between the second and third cooling hole, NASTRAN under predicts Bohn by 52 MPa, equating to a 17.7 % difference. Overall, the contour trends are the same as Bohn's with an average under prediction of 17 % for the entire blade.

The σ_e along line AB is shown below in Figure 5-4. The σ_e values are positive because of the definition of equivalent stress. Again an average under prediction of roughly 17 % is seen along the entire length. The trend here is the same as Bohn's and the two minimum stresses as well as the local maximum stress roughly at the centre of the line are correctly predicted. The initial suggestion that there might be a higher stress towards the suction side rather than the pressure side, due to the higher temperature gradient, has been confirmed.

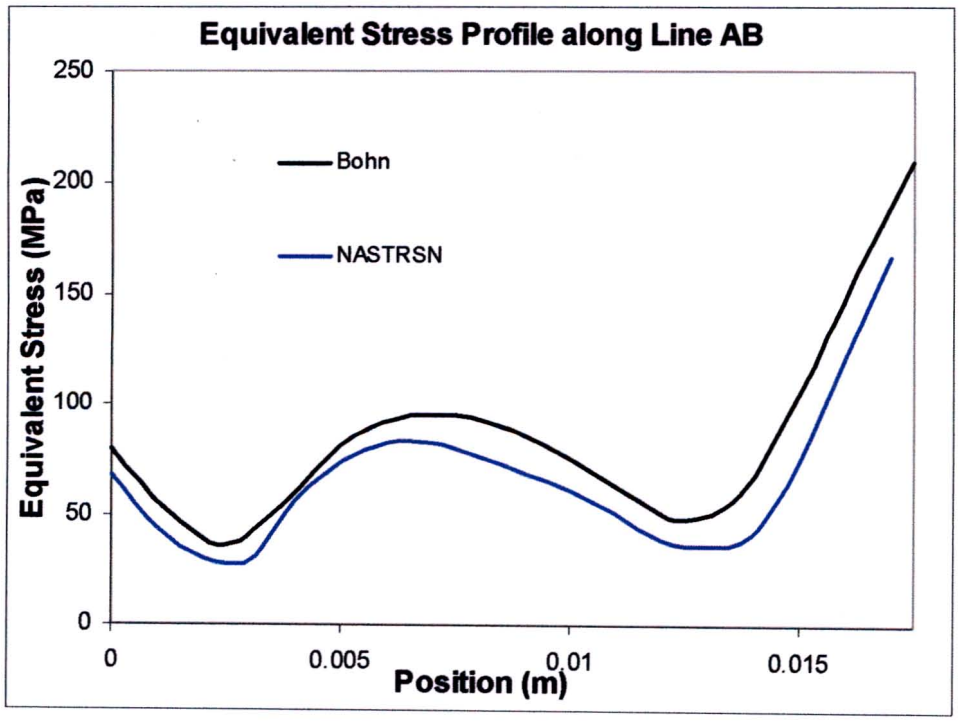

Figure 5-4: Equivalent stress profile along line AB from the mechanical analysis

The axial stress, σ_z, profile along line AB is show below in Figure 5-5. The NASTRAN curve tracks Bohn's curve identically with respect to the gradient, with only a slight under prediction. The previously noted Eq 5-1 describes the equilibrium condition for $\sigma_z = 0$. This condition is met when an initial stress free temperature is prescribed into the model. Bohn used a temperature of 488 K for this condition. It is not certain how Bohn obtained this temperature, however the same temperature was used in this analysis. The values for σ_z were obtained from Eq 5-3 below:

$$\sigma_z = \nu \cdot (\sigma_x + \sigma_y) - \alpha (T - T_{ref}) \cdot E \qquad \text{Eq 5-3}$$

Where ν is the Poisson's ratio, σ_x and σ_y are the stress components in the x and y direction, respectively, where these values were obtained from NASTRAN. α is the thermal expansion coefficient and E the Young's modulus. T_{ref} is the stress free temperature of 488 K. From Eq-3 it can be seen that $\sigma_z = 0$ when the temperature is 488 K, this can be seen from Figure 5-3 and 5-5. The stresses in the z direction occur as a result of temperatures above and below the stress free temperature.

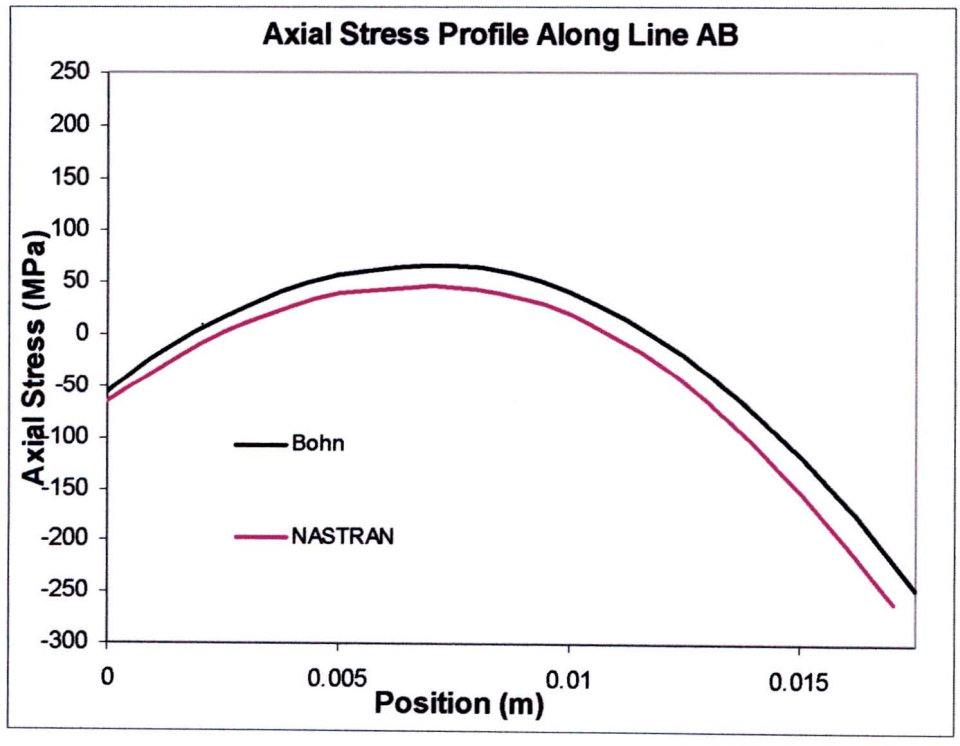

Figure 5-5: Axial stress profile along line AB from the mechanical analysis

The overall analysis compares very well with Bohn's prediction. The temperature and stress contours are accurately predicted over the entire blade, with a constant under prediction of the stress. There are two reasons for the constant under prediction of stress. The first reason being the slight 2 % to 3 % over prediction of the temperature in the blade, this however would only account for roughly 2 % to 3 % of the stress under prediction.

The second reason is simply the choice of solver used for the analysis. Bohn performed the analysis using a different code called MSC.MARC/Mentat. Both solvers solve the conduction heat equation for the thermal analysis, and the results between the two codes differ by only 2 % to 3 %. The result of the thermal analysis, which then forms the boundary condition for the mechanical analysis, was thus the same in both solvers. The 17 % difference between the two sets of data's was therefore put down to different codes being employed for the analysis. MSC.MARC/Mentat employs higher order isoparametric elements for plain-strain formulation, while MSC.NASTRAN does not. Isoparametric elements allow for an accurate modelling of the blade geometry. It is therefore believed that Bohn's results are more accurate.

5.3 Discussion of Results

The variation in the temperature and stress contours can be explained by the heat transfer and temperature distribution on the blade surface in Figures 4-35 and 4-32, respectively. On the suction surface from the stagnation point to 44 % axial chord, there is a steady decrease in temperature and heat transfer. The result can be seen in figure I-3, where the blade colour goes from a hot green colour at the stagnation point to a cooler blue region at 44 % axial chord. A steeper temperature gradient can be seen from inside the blade to the stagnation point, while at the minimum heat transfer value at 44 % axial chord a gentler temperature gradient can be seen from inside the blade to the surface.

This can be better explained by the temperature and stress profiles along line AB in Figures 5-3 and 5-4, respectively. Point A lies at roughly 40 % axial chord on the pressure surface and point B at roughly 68 % axial chord on the suction surface. The temperature profile along the line has a much steeper gradient towards the suction surface rather than the pressure surface. This can be attributed to the heat transfer coefficients at point B, which is twice as big as that at point A. The result of the steeper temperature gradient is a much higher stress towards the suction surface seen in Figure 5-4. It can be concluded that the temperature gradient is directly proportional to the stress.

From the temperature contour plot in Figure I-3, the temperature is seen to increase after the shock wave at 44 % axial chord on the suction surface. As a result of the shock wave, the heat transfer coefficient rises drastically. The temperature in the contour plot can be seen increasing after the shock wave and hence large temperature gradients are formed from the blade centre to the suction surface. The lower heat transfer coefficients on the pressure side result in gentler temperature gradients and hence smaller stresses.

It can thus be argued that the shock wave, which causes the steep increase in the heat transfer coefficient, is detrimental to the life of a blade. Ideally, there should be an even distribution of temperature inside the blade. Based on the entire analysis so far, it can be suggested that cooling holes 4 to 7 should be closer to the suction surface, this would then influence the cooling mechanism and result in cooler temperatures on the suction surface. There is also a large temperature gradient from the stagnation point to the blade centre, a cooling hole in this region might also be desired, or the second cooling hole could be moved closer to the stagnation point. This movement will also reduce the maximum stress, because the second cooling hole will be further away from the third cooling hole.

The CFD and FEM analysis thus prove to be a useful tool in the design of turbine blades. The high accuracy of both the CFD and FEM steady state models allows for transient thermal loading to now be calculated.

CHAPTER 6

THERMAL SHOCK AND TRANSIENT THERMAL STRESS

6.1 Introduction

With the steady state analysis complete and validated, and with good correlation to experimental data, the idea of the aerodynamic and thermal analysis can now be extended to transient cases. In all the test cases presented in this chapter, an unsteady TIT that varied with time was applied to the model. The goal was to simulate time varying stresses inside the NGV during a flight operation. Flight data for the T56 engine found on the C130 cargo plane (the 'jewel' of the SAAF) was acquired. The T56 mission profile TIT was used as the loading condition for the test cases.

The typical flight operation of the T56 engine is shown below in Figure 6-1, which shows the time varying TIT and compressor RPM. Not all engines operate like the T56, each have their own start-up curves. This engine is extremely inefficient from a combustion point of view during start up.

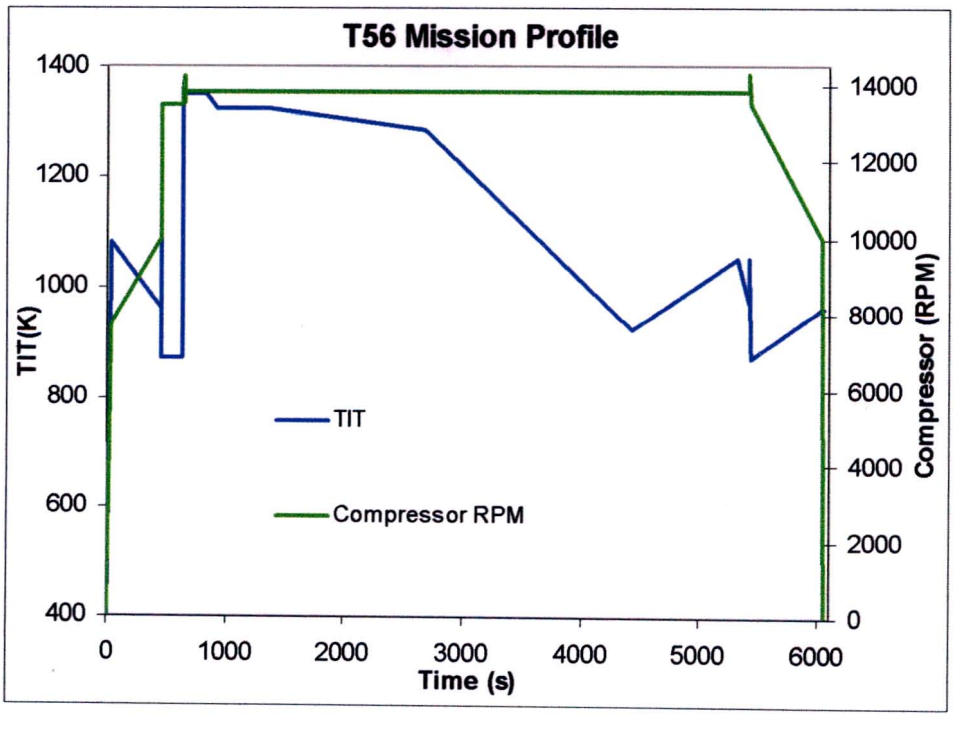

Figure 6-1: Typical mission profile for the T56 engine

The reason for the inefficiency is due to the bleed valves, which remain open until 94 % rpm, where after they are closed. During start up, over 60 % of all the air entering the compressor is bled and used for cooling, which results in less air entering the combustion chamber. After take off (first 30 seconds), from 30 to 450 seconds, the engine is stabilized by Low Speed Ground Idle (LSGI). This regime is used to taxi the aircraft into dusty conditions to minimize compressor blade erosion. At this setting, due to the inefficiency, the TIT remains high.

During High Speed Ground Idle (HSGI), from 450 to 638 seconds, the rpm is at 94 % and the bleed valves are closed, which results in the combustion being at its optimum and hence a lower TIT can be set. There after a climb setting is set, which results in a TIT spike. After the climb a cruise setting is set at 2672 seconds, while descent and landing is set at a lower temperature.

6.2 Model Specifications

There are two possible procedures that can be performed for a transient thermal stress analysis. For both cases, an unsteady aerodynamic analysis must be performed in order to acquire the unsteady turbine blade surface temperature distribution. The transient aerodynamic analysis would result in the temperature profile on the turbine blade surface varying non-linearly with respect to time and spatially along the blade surface. The resulting unsteady temperature along the surface can then be prescribed at each node in NASTRAN and a transient thermal analysis can be performed. That would result in a continuous stress plot for the entire mission profile.

This method is however extremely time consuming, due to data transfer between FLUENT and NASTRAN. There are many parts of the mission profile where the temperature gradient is unchanged for large periods of time. It is therefore only necessary to calculate an optimum amount of stress points in these parts. The method employed, was to take the temperature profile from the transient FLUENT simulation at certain times and, simulate the corresponding stress at that one time instant. The time steps chosen were dependent on the time range and steepness of the temperature changes.

A transient boundary profile was defined for all the test cases in FLUENT. The boundary profile (transient TIT) was set in the total temperature input at the pressure inlet boundary. All the time varying TIT boundary profiles are shown in Appendix J. For every test case,

two FLUENT simulations had to be performed, one for the Spalart-Allmaras model and another for the Laminar model. As before, the temperatures were combined at the transition points on the blade surface to acquire the correct temperature distribution. In all the cases below, the maximum stress inside the blade (found on the rim of the second cooling hole) was plotted against time.

The NGV suffers due to shock loading (abrupt changes in temperature) and thermal fatigue, which is as a result of thermal loading over a long period of time caused by many flights. It is therefore necessary to model and study simple shock loading, as well as an entire mission profile.

6.3 Simple Shock Load

At start up, the TIT rises from an ambient temperature to 1080 K in 30 s, this thermal shock hurts the NGV the most in the entire mission profile. A simple shock that represents this situation was simulated, as shown in Figure 6-2. The temperature increases from 308 K to 1200 K in 30 s and back down to 308 K in another 30 s. This also allows the author to observe how the stress inside blade behaves due to a simple shock load, before the mission profile was simulated.

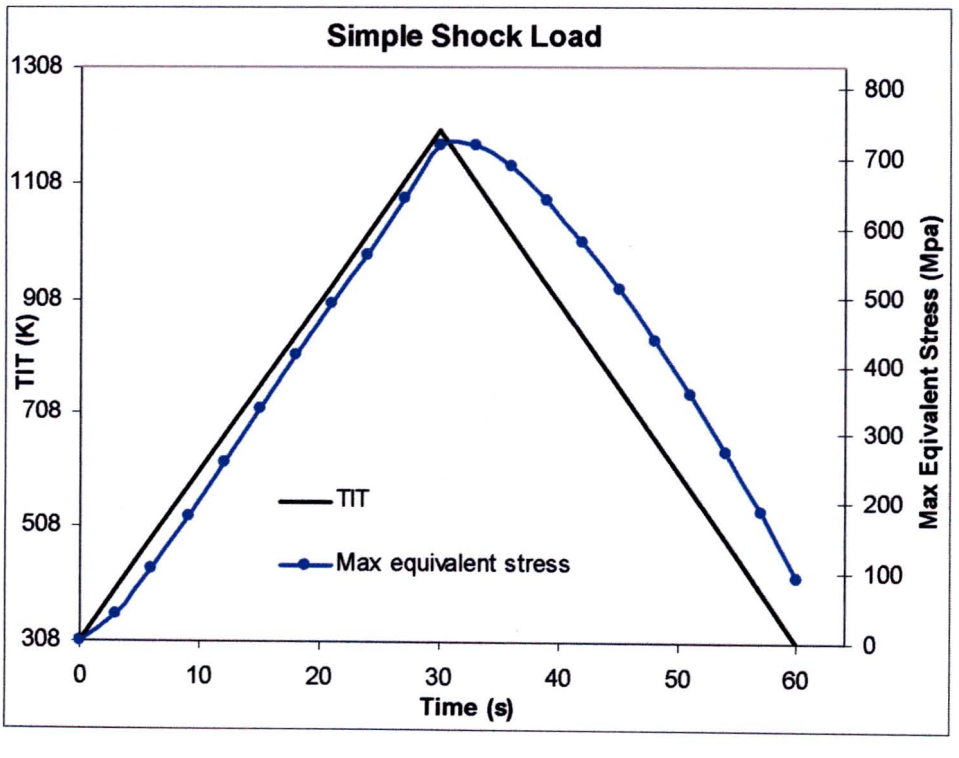

Figure 6-2: Time varying maximum equivalent stress for a simple shock load

A NASTRAN simulation was performed every 3 seconds, which proved to be sufficient for an accurate stress curve. From 0 to 3 s, the stress increases with a gentle slope by 37 MPa while the TIT increases to 410 K. From 3 s to the peak TIT, the stress increases proportionally to the TIT. The peak stress of 726 MPA occurs at 32 s. From 32 to 35 s the stress decreases with a gentle slope, where after the stress decreases with a constant gradient to a minimum of 93 MPa at 60 s.

The stress lags the TIT throughout the simulation, which is due to conduction through the blade. The stress is measured on the rim of the second cooling hole, in the centre of the blade. Had the stress near the blade surface been monitored, the conduction time would have been far less. The stress lags the TIT by 2 to 3 s for the first 30 s of the simulation. The lag then increases to between 6 and 8 s for the last 30 s of the simulation. The difference in the conduction lag between the first and last 30 s can easily be explained. The conduction lag in the first 30 s can be seen by the difference in time between when the maximum TIT and the maximum stress occur. From 30 s onwards the conduction lag 'out of the blade' adds onto the initial lag.

From the result of the analysis it can be seen that the physics of the problem have accurately been modelled, where the conduction through the blade is logical and has been demonstrated by the graph. When the TIT is 788 K the stress is 330 MPa. In the steady state analysis, the stress was 354 MPa for the same TIT. The difference of 24 MPa, is as result of the conduction lag. The Spalart-Allmaras simulation took 14 hours to complete and the Laminar model 6 hours.

6.4 Multiple Shock Loads

For this case, the simple shock load was repeated continuously six times. The idea was to observe whether the maximum stress varied for each single shock. The Spalart-Allmaras simulation took almost four days to complete, while the Laminar simulation took just under 36 hours. The stress simulations were only performed six times for every shock load as six points were enough to accurately represent the stress curve.

Figure 6-3 shows the varying stress through the six shock loads, a maximum stress through the peak stress points along with the minimum, are also shown. The stress curves are almost identical through all six shocks, with respect to the stress variance and lag due to conduction. The only difference is that from the second to the sixth shock, the maximum stress rises by roughly 10 MPa. The minimum stresses through the same shock loads are all around 63

MPa. It can be argued from the analysis that the stress does not vary enough between the shocks, so as to require an analysis of this type. For thermal fatigue calculations, a single shock is all that is necessary, where Figure 6-2 can simply be repeated to represent cyclic loading.

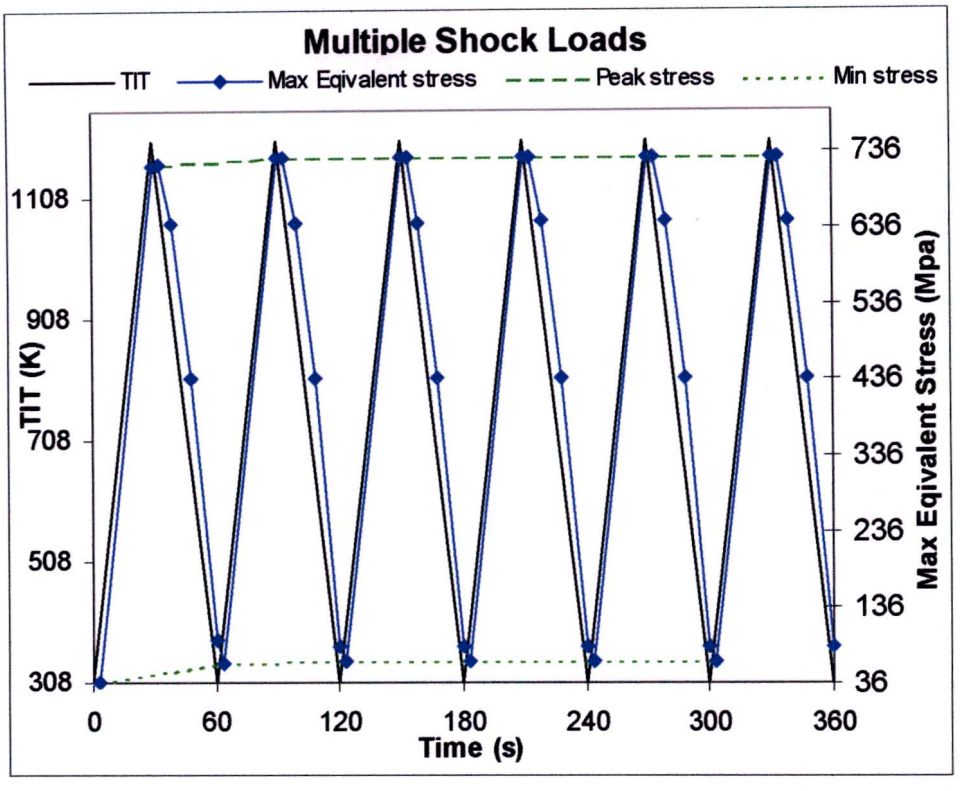

Figure 6-3: Time varying maximum equivalent stress for multiple shock loading

6.5 The Simplified Cycle

The mission profile was simplified to a temperature rise of 1349 K and fall to 308 K, equating to the maximum TIT found in the mission profile and the case spanned for 6047 s. The simplified cycle and the mission profile are shown in Figure 6-4, along with the stress for the Simplified cycle. The TIT rises slowly to a maximum in 638 s, hence the conduction lag is minimal and cannot even be seen in the figure. The stress rises to 944 MPa as the TIT reaches its maximum value of 1349 K and rises by only a further 5 MPa until the TIT starts decreasing again.

The minimal conduction lag was expected and therefore it was only necessary to perform 8 stress simulations to describe the stress profile. It can thus far be noted that stress is directly proportional to the TIT and is also dependent on the gradient of the TIT, where a gentler TIT

gradient is always preferred to a sharp TIT increase. Due to the simplification of the TIT, the Spalart-Allmaras model only took 64 hours to run while the Laminar model took 27 hours to complete.

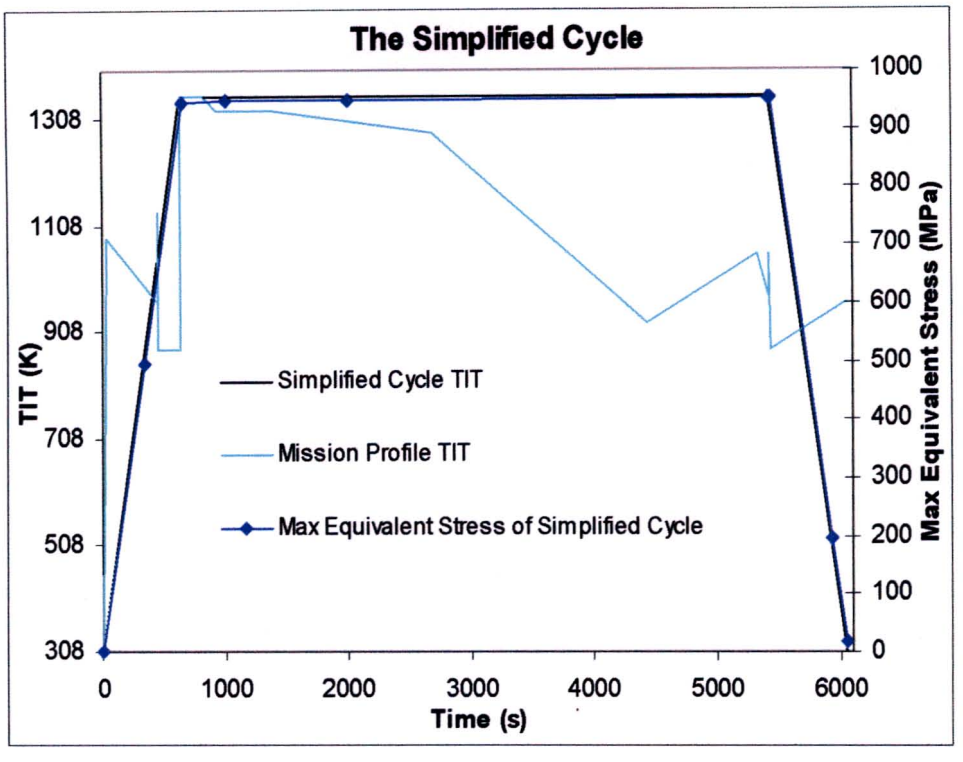

Figure 6-4: Time varying maximum equivalent stress for the Simplified cycle

6.6 Multiple Simplified Cycles

For this case the simplified cycle was repeated 3 consecutive times, with four stress simulations performed for each cycle, which was enough based on the previous simulation results shown in Figure 6-4. The maximum stress in the first cycle is again 949 MPa, this value only increases by 6 MPa for the second and third cycles. The stress at the end of the first cycle decreases to 16 MPa and to 5 MPa at the end of the second cycle, and again to 16 MPa at the end of the third cycle.

This cyclic behaviour is very small and would have little if no influence on thermal fatigue calculations. It is therefore unnecessary to perform multiple loading, as the result is no different to simply repeating the stress calculated for a single cycle. The computational effort is not justified. The Spalart-Allmaras model took 8 days to complete while the Laminar model took 3 and half days to complete.

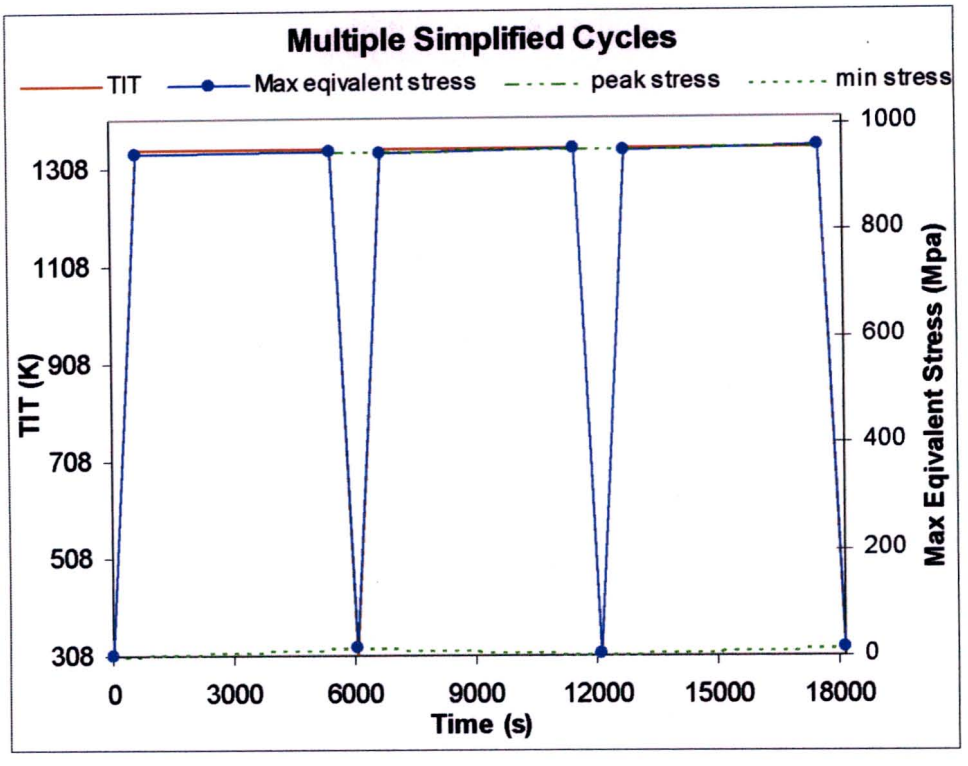

Figure 6-5: Maximum varying equivalent stress for multiple simplified cycles

6.7 The T56 Mission Profile

The previous four cases showed the behaviour of the stress curve due to a changing TIT profile, where three observations were made. The stress is proportional to the TIT, which is also dependent on the gradient of the TIT. A thermal shock results in a noticeable conduction lag while for a gentle TIT gradient, the stress curve hugs the TIT through out. From the results it can also be argued that simulating repeated cyclic loading is unnecessary, as the change in stress does not vary by more than 10 MPa.

At 636 s during the transient FLUENT simulation, the residuals would abruptly diverge and a fatal error would occur, when the simulation was attempted again, the same result occurred. After much deliberation it was thought that the steep temperature increase of 476 K from 636 to 638 s was the cause of the problem. After consulting the FLUENT manuals, it was found that FLUENT can perform Adaptive Time Stepping Control. The control was set up, which results in FLUENT decreasing the time step size when large changes in the boundary profiles occur. Permitting a constant supply of electricity to the processor, the Spalart-Allmaras model took 13 days to complete while the Laminar model took just under 6 days to complete.

30 stress simulations were performed for the entire mission profile, where the simulations were clustered around steep temperature changes. The result of the simulations is shown in Figure 6-6. Due to the large time span of 6047 s for the simulation, the stress profile is unclear from the figure. Figures 6-7, 6-8 and 6-9 show a close up view of the important regions in mission profile.

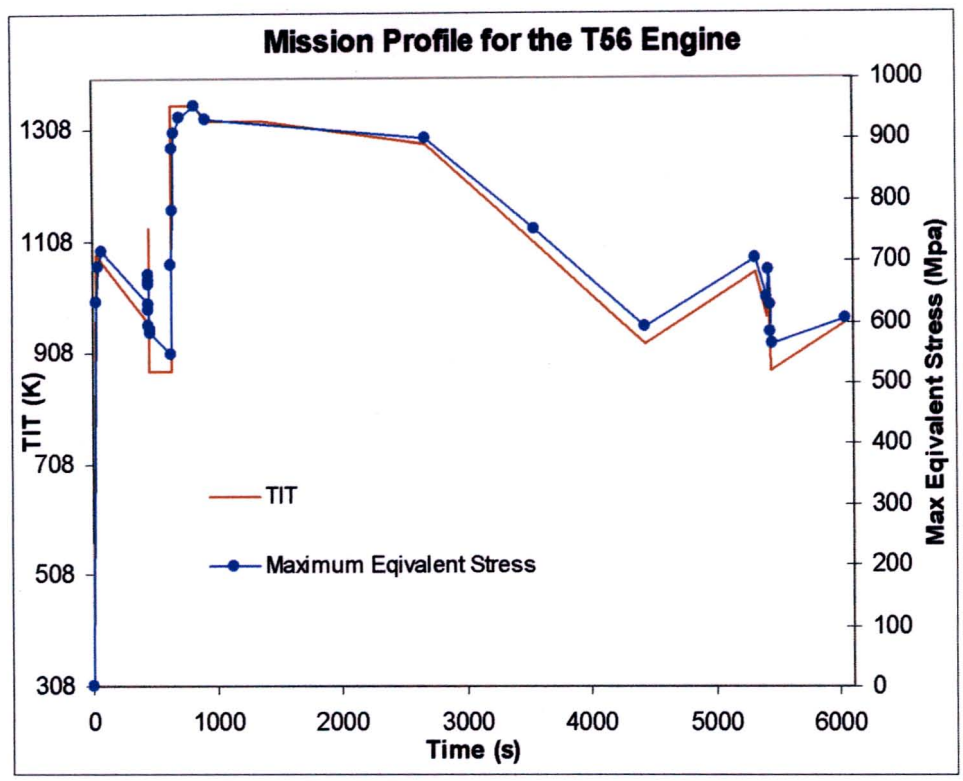

Figure 6-6: Maximum varying equivalent stress for the T56 mission profile

Figure 6-7 shows the first 300 s of the simulation. At start up, the spike in TIT reaches a maximum temperature of 1070 K in 30 s. At this part, the engine fuel pumps pump in series where after the start up a leaner fuel mixture is required and they switch to pumping in parallel. The conduction lag observed here was similar to that observed for the Simple shock case. The maximum stress reached, as a result of the spike, is 716 MPa. Due to the gentle TIT slope after 30 s, the stress curve takes a while to even out, where after 70 s it declines at a constant gradient relative to the TIT gradient.

Figure 6-8 shows the area between 430 and 730 s, which encompasses two temperature spikes. The TIT gradient is constant from 30 to 450 s, for which the stress variation was previously explained. At 450 s there is a small temperature increase of 170 K that results in a small stress increase of 40 MPa.

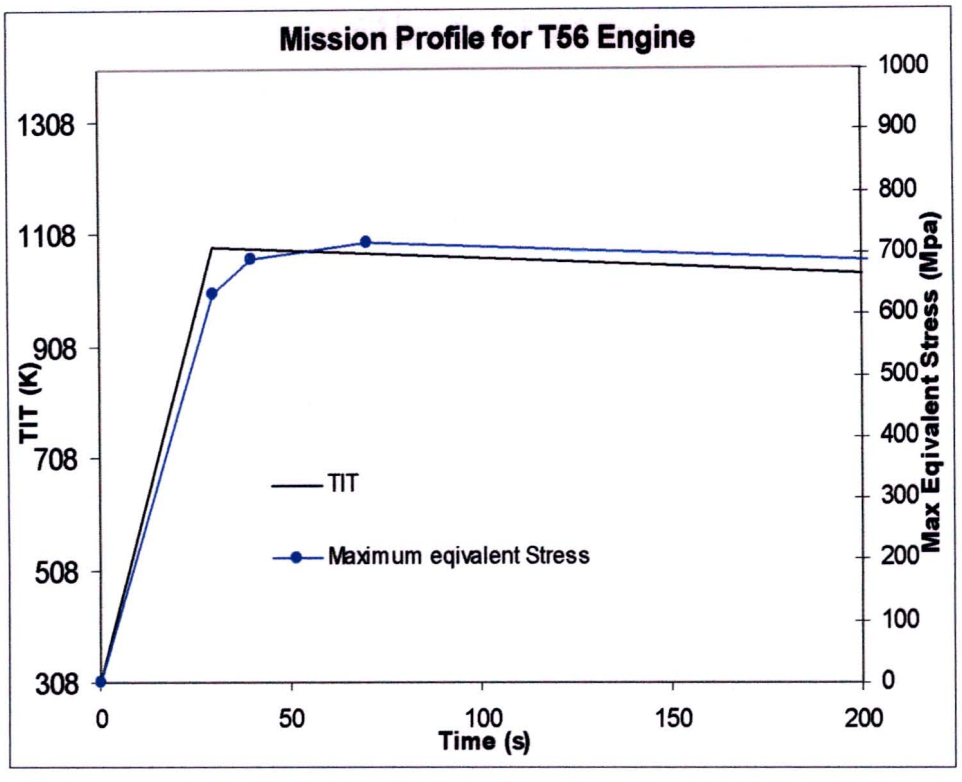

Figure 6-7: Maximum varying equivalent stress for the T56 mission profile, showing the first 300 seconds

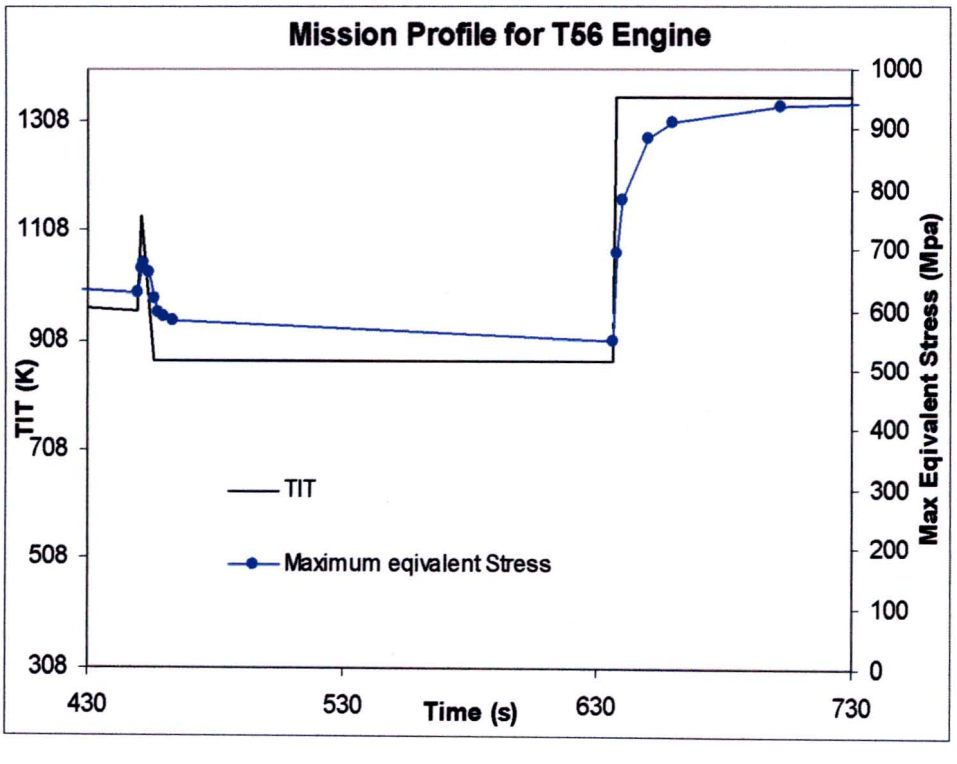

Figure 6-8: Maximum varying equivalent stress for the T56 mission profile, showing the time range between 430 and 730 seconds

From 464 to 636 s the stress curve declines with a very gentle gradient to 583 MPa. At 636 s there is an abrupt increase in the TIT of 476 K, which initially results in a sharp rise of the stress curve. Then, as the TIT becomes constant, the stress rise becomes more and more horizontal up to 702 s where the stress is 938 MPa. From 702 to 826 s the stress rises by another 16 MPa to a value of 954 MPa, which corresponds to the maximum stress in the entire mission profile.

From 826 to 5322 s during the climb and cruise setting, the TIT remains stable with a few minor changes to the gradient. In this part the stress curve hugs the TIT throughout. Figure 6-9 shows the time period between 5300 and 5900 s (the descent) where the last temperature spike occurs at 5414 s. The temperature only increases by 80 K, which results in a stress increase of 47 MPa. The TIT decreases to 873 K after the spike at 5439 s, where the stress curve follows suit, down to 565 MPa. From 5439 s to the end of the mission at 6047 s, the TIT increases with a gentle gradient to 963 K, where at touch down the final stress in the NGV is 605 MPa.

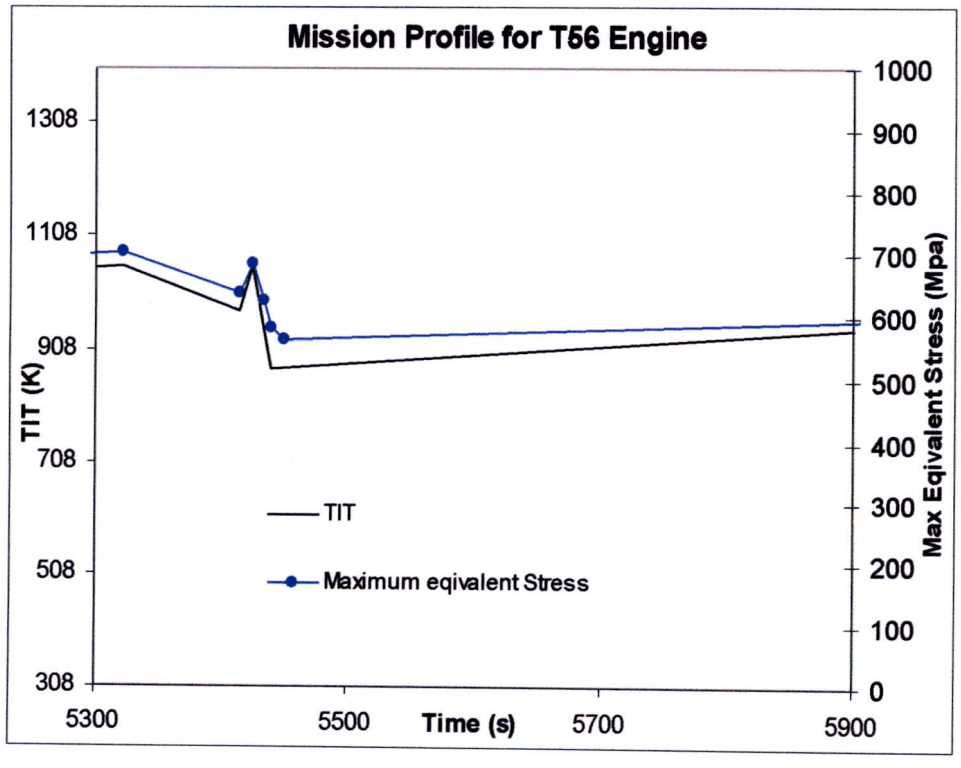

Figure 6-9: Maximum varying equivalent stress for the T56 mission profile, showing the time range between 5300 and 5900 seconds

6.8 Discussion

The modelling procedure for calculating stress for various transient thermal loading conditions was demonstrated. Most importantly, the behaviour of the stress relative to the changing TIT was also shown. The results of the mission profile stress analysis can now be used as an input into thermal fatigue calculations. The first possible calculation should be a total life calculation, in which the time to failure is calculated, not considering the way in which failure is reached.

The second more accurate and more suitable calculation would be a crack growth calculation. Crack growth calculations accept the presence of material defects and aim to monitor crack growth and remove the blade before the crack becomes unstable. In the aircraft industry, it is desirable to make use of a single NGV for as long as possible, due to the high costs associated with maintenance and new components. Crack growth calculations perform a local analysis, using stress profiles at very specific locations, this being the location of crack initiation. From the analysis on the MARK II NGV it can be argued that the location of crack growth initiation would be at the rim of the second cooling hole, where the maximum stress occurs. Crack growth on a blade or any component is also influenced by oxidation. This leads to more support of the crack growth initiation position, because the cooling air could possibly aid in the occurrence oxidation.

All the transient test cases performed monitored the maximum stress in the blade at the second cooling hole, where crack growth initiation is believed to occur. All the boundary conditions necessary to perform crack growth calculations have been presented throughout the entire analysis. Another important criteria in turbine blade life assessment are the thermal shock calculations. The results of the thermal shock simulations can be used to calculate a materials ability to withstand abrupt changes in temperature without fracturing. De Guire (2003) gives an equation to calculate the Thermal Shock Resistance (TSR) of a material, based on the materials thermal and mechanical properties, Equation 6-1 below shows the TSR:

$$TSR = \frac{\sigma_f k}{E\alpha} \qquad \text{Eq 6-1}$$

Where k and α are the thermal expansion coefficient and the thermal conductivity, respectively, and E is the materials Young's modulus. σ_f is the material fracture stress. The

fracture stress of ASTM 310 stainless steel could not be found, however the yield stress, which is 230 MPa was known. Although σ_f is larger than the yield stress, for a stainless steel that is not ductile the two values are very close, and hence the yield stress was used in place of σ_f. This also shows a more conservative approach. Figure 6-10 shows the TSR of the material used in all the analyses in this dissertation.

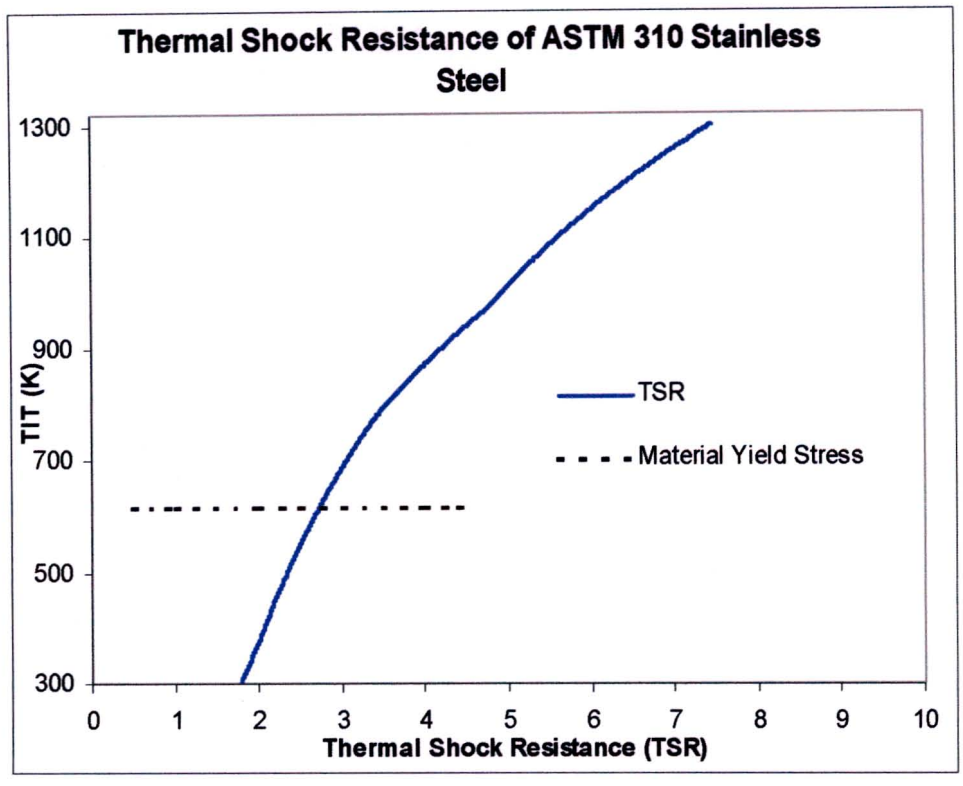

Figure 6-10: The Thermal Shock Resistance (TSR) of ASTM 310 stainless steel

As mentioned before, ASTM 310 stainless steel is not usually used for turbine blades. Bohn however chose this material for the steady state experiments. The yield stress of the material is 230 MPa, which occurs when a TIT of 616 K is reached. Figure 6-10 shows that the maximum TSR is 2.73 when the yield stress is reached at 616 K.

This graph is the basis for thermal shock calculations, and can be used to calculate any material's TSR. From Eq 6-1, it can be shown that a decrease in α would result in smaller strain gradients and hence an increase in the TSR. An increase in k will reduce internal temperature gradients in the material and also result in an increase in the TSR. The k is the most important material property in the design of cooled turbine blades, which experience immense temperature gradients.

6.9 Sources of Error

The accuracy of the thermal fatigue calculations depend on the accuracy of the thermal stresses employed in the calculations. The overall accuracy of the transient stress analysis is dependent on the separate models integrated into the transient analysis. The critical aerodynamic analysis deviated by 1 % from the experimental measurements, while the thermal analysis deviated by 2 to 3 % from another analysis performed by Bohn. As there is no direct experimental method to calculate thermal stresses in turbine blades, the accuracy of the mechanical analysis is purely solver related (assuming the aerodynamic and thermal analysis accuracy is good).

For the transient analysis, the most important boundary condition is the TIT, which has been modelled. The transient pressure boundary condition was however unavailable, which resulted in the inlet and exit Mach numbers being constant throughout the transient analysis. The flow features were therefore relatively unchanged. The biggest concern with not modelling unsteady pressure, is the possibility that the shock wave on the suction surface could cause transition from laminar to turbulent flow elsewhere on the surface. The correct modelling of the shock wave is enormously vital as it greatly increases the heat transfer to the blade, as shown in the steady state analysis.

The transient stress simulations were performed for an exit Mach number of 0.98, which relates to a pressure ratio $P_{in}/P_{out} = 2$. In order to quantify the effect different pressure ratios have on the blade surface pressure distribution, four simulations were performed, each at a different exit Mach number. The idea was to simulate the different possible pressure scenarios that occur in a transient pressure profile. Figure 6-11 shows the pressure distribution for Mexit = 0.37, 0.58, 0.75 and 1.04. It was shown in Chapter 4 that the pressure results correlated extremely well with experimental data and hence the results presented in Figure 6-11 can be presumed accurate.

From the figure, the pressure effect appears to be largely reflected as a shift in general pressure level rather than in pressure distribution. The sharp rise in the pressure on the suction surface occurs at essentially a fixed surface location, implying that the pressure rise is strongly independent of the exit Mach number. This gives further evidence (from Chapter 4) that the steep rise in pressure is strongly dependent on the blade surface Mach number distribution (which is also fixed due to the throat area) rather than Reynold's number level.

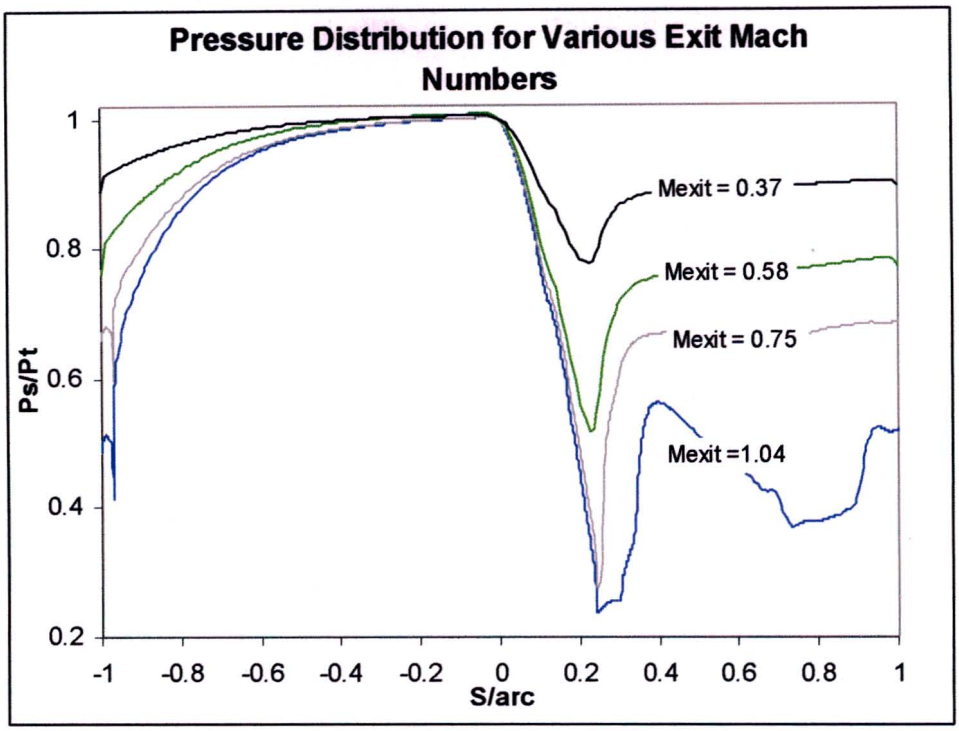

Figure 6-11: Pressure distribution for a varying exit Mach number, simulated using the Spalart-Allmaras turbulence model

Performing the transient stress analysis with a transient pressure boundary profile would undoubtedly increase the accuracy of the results. However, the results shown in Figure 6-11 would suggest that different pressure ratios have a small effect on the blade surface temperature distribution, compared to the effect that a transient TIT would have. The procedure to calculate transient thermal stresses has been successfully demonstrated. Employing the modelling procedure presented, one could vary the different boundary conditions to study the effect on the thermal stresses, and also predict the turbine blade life in order to ultimately perform on-condition maintenance.

CHAPTER 7

CONCLUSION

The ultimate Gas-Turbine-Life-Model would be one that could predict the life of every component in the engine, based on current engine performance. Thus, during a flight, the mechanical life of all the components could be monitored. This implies that all the necessary calculations would have to be performed in real-time. There is no such model available at present.

The models that do exist, are those that obtain engine performance history from in-flight monitored engine parameters and flight conditions. The data is then downloaded for processing after the completion of a flight. ARMSCOR, along with universities in South Africa, is currently developing a gas turbine life model. The goal of the research presented in this dissertation, was to demonstrate a modelling procedure for the calculation of realistic transient thermal stresses. This, in turn, provides quality input data for thermal fatigue calculations, for the most critical component in the engine, namely the NGV.

Computing the thermal stresses inside a turbine blade is no small task. Simulating turbine blade thermal stresses requires both flow and structural analysis for the blade. The flow and structural analysis have to be performed separately, due to each employing different formulations for the governing equations. FLUENT, which uses the Finite Volume formulation, was used to resolve the flow field while NASTRAN, which uses Finite Element formulation, was used for the structural analysis.

The understanding of thermal stress behaviour begins with performing a steady state analysis. The CFD model must be validated against experimental data, while choosing a suitable code for the FEM model, is vital. This is due to the limitations of performing experimental stress measurements. Only once the steady state model has been validated can transient simulations be performed. For the transient models, the choice of boundary conditions is important. The unsteady TIT, being the root cause of thermal stresses, must be modelled correctly in order to accurately model the corresponding unsteady thermal stresses. The transient simulations were performed for cases with abrupt temperature changes, which result in thermal shocks, and cases that represent typical operational flight data, which can be used for thermal fatigue and crack growth calculations.

The results of the steady state aerodynamic analysis were in excellent agreement with the experimental data of Nealy et. al. (1984) and Bohn et. al. (1995). The flow field was accurately resolved, which resulted in the surface pressure prediction being exact with that of Nealy's experimental data. All three turbulence models investigated gave the same excellent prediction. Grid independent solutions were easily achieved with all the mesh models producing the same results.

The results of the surface temperature distribution were far more difficult to achieve. Grid independent solutions were only achieved when a total decomposition of the flow field was performed, along with continuous mesh refining in regions where high pressure and temperature gradients were found. All three turbulence models performed exceptionally well in the turbulent regions of the blade, where the Spalart-Allmaras model over predicted Bohn's experimental data by roughly 1 %. All the turbulence models showed an over prediction in excess of 10 % in the Laminar region. It was thus shown that none of the FLUENT turbulence models could accurately predict the heat load to the blade, where this finding is strongly emphasised throughout the open literature.

After the extensive effort of predicting the temperature distribution using the most established turbulence models, a Laminar model was used for the analysis. It was discovered, that the Laminar model could highly accurately predict the surface temperature distribution. The model over predicted Bohn's experimental data by a mere 1 % in the laminar regions of the blade. The results of the Spalart-Allmaras and Laminar model were combined, which resulted in the validation of the CFD model.

The results of the steady state FEM analysis were compared to the predicted results of Bohn. The thermal analysis resulted in the internal blade temperature profile, which over predicted Bohn's data by 2 % - 3 %. The mechanical analysis predicted the correct thermal stress contour trends, but under predicted the stress magnitudes by an average of 17 % for the entire blade. The reason for the under prediction is believed to be due to different solvers used for the two predictions, as explained in chapter 5. For the FEM analysis, the mesh used is not nearly as important as it is for the CFD analysis. The correct material and element characterisation and accurate results form the aerodynamic analysis are most vital to the accuracy of the stress prediction.

Transient stress profiles were calculated for the T56 engine, where the stress curve is primarily dependent on the changes in TIT. From the stress plots it can be argued that based on the stress behaviour as explained in chapter 6, the model is accurate and represents a

realistic analysis. The thermal shock during start up was modelled and showed that the resulting stress rose tremendously, which causes the most damage to the component. The minimum and maximum stresses are presented and can be used as boundary conditions to calculate the critical number of cycles to failure.

The success of the transient thermal stress plots is mainly due to the discovery of the Laminar model. The accuracy of the aerodynamic analysis is the heart of the work presented in this dissertation. The combination of the Spalart-Allmaras and Laminar model for the aerodynamic analysis proves to be an accurate tool, for predicting the heat load as well as the corresponding thermal stresses. This combination thus proves to be a solution to the temperature prediction dilemmas discussed in the literature review.

CHAPTER 8

FUTURE WORK RECOMMENDATIONS

There are two possible paths to take in the continuation of the research presented in this dissertation. Firstly, a review of the combined aerodynamic and thermal analysis could be performed. The temperature distribution inside the blade causes the blade to deform slightly, it is not possible to represent this in FLUENT. The small strains can however be modelled in the FEM analysis. The slightly deformed blade could then be re-simulated in FLUENT, as the change in curvature of the blade would undoubtedly affect the aerodynamic conditions (such as transition) on the blade surface. This presents a coupled analysis where the temperatures and displacements are a function of each other.

The FEM analysis performed in this dissertation was one where the material behaviour was linear elastic. This implies that the material deformed along the straight-line portion of the stress-strain curve and therefore no plasticity or failure occurred. In this type of analysis, highly localised stress concentrations are permitted, such as on the rim of the second cooling hole. Bohn modelled the material with isotropic linear elastic behaviour and hence, for comparison and validation, the same type of analysis was performed.

Secondly, the work performed can be used as the basis to move forward in a number of ways. A comprehensive study of available thermal fatigue and crack growth models should be performed, in order to choose the most suitable model. The stress plots presented in this dissertation, should then be used in a thermal fatigue model. This, in turn, would result in the first complete NGV lifing model. The lifing model could then be improved in many ways. The CFD analysis should be extended to 3-D, in order to quantify the difference in the temperature prediction between 2-D and 3-D. The FEM analysis should also be performed for a 3-D case and again, compared to the results of the 2-D study. After the 3-D blade analysis, the hub should also be included in the model. Once the complete stator row has been modelled and analysed, the rotor section should be included, which undoubtedly influences heat transfer to the stator (NGV) blades.

The most daunting task is experimental stress measurements. The FEM stress predictions must be validated. There is one possible procedure to measure stress indirectly. The NGV can be instrumented with high-temperature (k-type) strain gauges, at the mid-span of the NGV. The resulting surface strains can be converted to the corresponding stresses. The

resolution of the surface strain would be dependent on the amount of strain gauges on the surface. A larger scaled blade would therefore have to be used. The main limitation of this experimental technique is simply cost. High temperature strain gauges are extremely expensive and can only be used once. The relationship between strain and stress for the experimental work as well as, the relationship between temperature and stress for the prediction, do however present a possible way of validating thermal stresses.

APPENDIX A

Study of the Open Brayton Cycle.

A schematic of the Brayton cycle is shown in figure 1-3. The cycle is described by four basic processes:

Process 1: Between points 2 and 3 – Isentropic compression
Process 2: Between points 3 and 4 – Reversible constant pressure heat addition
Process 3: Between points 4 and 5 – Isentropic expansion
Process 4: Between points 5 and 6 – Constant pressure heat rejection

Figure A-1 shows the four processes of the ideal Brayton cycle on a T-s diagram.

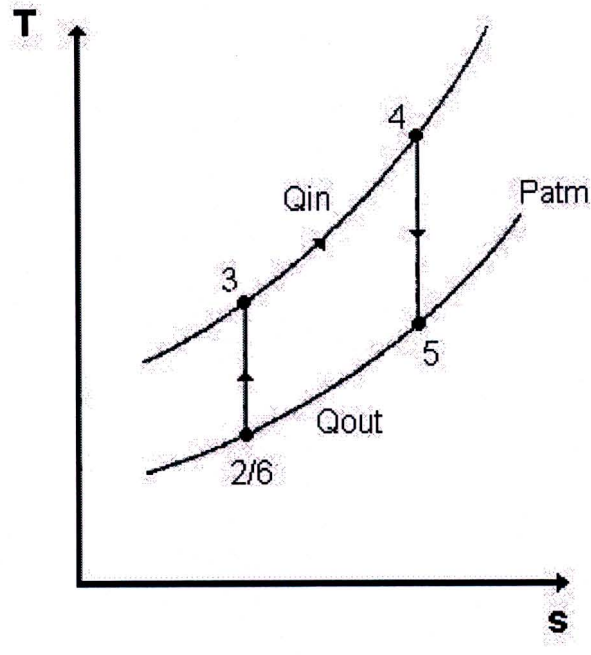

Figure A-1: The ideal Brayton cycle.

To analyse the model, one needs to use the air standard model where the working fluid air, is treated as an ideal gas and performing the thermodynamic analysis one needs to consider each component individually.

Compressor:

Ideally there is no heat transfer from the compressor to the surroundings and assuming steady state, the governing equation can be written as:

$$\dot{H}_2 + \dot{W}_{in} = \dot{H}_3 \qquad \text{Eq A-1}$$

Considering that there is one inflow and one outflow, the mass flow must be conserved; a more specific form of the above equation can be written as:

$$\dot{m} h_2 + \dot{m} w_{in} = \dot{m} h_3 \qquad \text{Eq A-2}$$

Rearranging and grouping related terms:

$$w_{in} = h_3 - h_2 \qquad \text{Eq A-3}$$

Because the fluid is assumed to be an ideal gas, the enthalpies can be represented in terms of temperatures by using the appropriate equation:

$$dh = c_p dT \qquad \text{Eq A-4}$$

Assuming a constant specific heat:

$$w_{in} = c_p \left(T_3 - T_2\right) \qquad \text{Eq A-5}$$

Introducing the compressor efficiency:

$$\eta_{comp} = \frac{w_{in,is}}{w_{in,ac}} = \frac{h_{3,is} - h_2}{h_{3,ac} - h_2} \qquad \text{Eq A-6}$$

For a perfect gas the above equation is reduced to:

$$\eta_{comp} = \frac{T_{3,is} - T_2}{T_{3,ac} - T_2} \qquad \text{Eq A-7}$$

Combustor:

Again, assuming steady state, the governing equation can be written as:

$$\dot{H}_3 + \dot{Q}_{in} = \dot{H}_4 \qquad \text{Eq A-8}$$

The mass flow in the combustor is again conserved:

$$\dot{m} h_3 + \dot{m} q_{in} = \dot{m} h_4 \qquad \text{Eq A-9}$$

Rearranging and grouping related terms:

$$q_{in} = h_4 - h_3 \qquad \text{Eq A-10}$$

Assuming an ideal gas and constant specific heat:

$$q_{in} = c_p \left(T_4 - T_3\right) \qquad \text{Eq A-11}$$

Turbine:

Ideally there is no heat transfer from the turbine to the surroundings and assuming steady state, the governing equation can be written as:

$$\dot{H}_4 - \dot{W}_{out} = \dot{H}_5 \qquad \text{Eq A-12}$$

The mass flow in the turbine is again conserved:

$$\dot{m} h_4 + \dot{m} w_{out} = \dot{m} h_5 \qquad \text{Eq A-13}$$

Rearranging and grouping related terms:

$$-w_{out} = h_5 - h_4 \qquad \text{Eq A-14}$$

Assuming an ideal gas and constant specific heat:

$$-w_{out} = c_p (T_5 - T_4) \qquad \text{Eq A-15}$$

Introducing the turbine efficiency:

$$\eta_{turb} = \frac{w_{out,is}}{w_{out,ac}} = \frac{h_{5,is} - h_4}{h_{5,ac} - h_4} \qquad \text{Eq A-16}$$

For a perfect gas the above equation is reduced to:

$$\eta_{turb} = \frac{T_{5,is} - T_4}{T_{5,ac} - T_4} \qquad \text{Eq A-17}$$

The overall cycle efficiency can be written as:

$$\eta_{cycle} = 1 - \frac{c_p (T_5 - T_2)}{c_p (T_4 - T_3)} \qquad \text{Eq A-18}$$

From equation A-18 it can be seen that an increase in T_4, the TIT, will result in an increase in overall cycle efficiency.

Symbols

$\dot{m}$	Mass flow rate
h	Enthalpy
w	Work
dh	Change in enthalpy
dT	Change in temperature
c_p	Specific heat
T	Temperature
η	Efficiency
Q	Heat

Subscripts

2 to 6	Refer to figure 1-3
in	Input
is	Isentropic
ac	Actual
out	Output

APPENDIX B

Mark II NGV Data

Node	X co-ord (cm)	Y co-ord (cm)	Pressure (Pa)	Temperature (K)	Heat Flux (W/m^2)	Heat Transfer Coefficient ($W/m^2/K$)
1	6.8475	-10.8677	167091	605.02	28484	89.876
2	6.8403	-10.8401	167020	600.72	27814	88.358
3	6.8328	-10.8113	166740	595.76	29540	94.515
4	6.8251	-10.7814	166259	589.50	30674	98.892
5	6.8170	-10.7503	165928	582.20	30673	99.705
6	6.8085	-10.7180	165810	574.64	30467	99.914
7	6.7973	-10.6752	165853	566.64	31593	104.866
8	6.7860	-10.6322	165932	557.99	34134	114.682
9	6.7745	-10.5891	165824	548.50	37333	127.001
10	6.7629	-10.5457	165340	538.16	41200	141.968
11	6.7512	-10.5022	164372	527.82	45606	159.246
12	6.7393	-10.4584	162801	519.64	50321	178.159
13	6.7272	-10.4145	160566	515.60	55335	198.779
14	6.7149	-10.3704	157718	514.53	60673	221.319
15	6.7025	-10.3261	154611	513.98	66187	245.383
16	6.6898	-10.2816	152284	512.73	71664	270.328
17	6.6770	-10.2370	151675	510.52	76720	294.792
18	6.6640	-10.1921	151382	507.41	80638	315.997
19	6.6508	-10.1471	150942	503.38	83523	334.171
20	6.6376	-10.1018	150429	498.32	85832	350.788
21	6.6242	-10.0563	149863	492.14	87038	363.198
22	6.6107	-10.0106	149184	485.02	87089	370.400
23	6.5971	-9.9647	148405	477.70	86148	372.135
24	6.5834	-9.9186	147620	472.01	83702	365.570
25	6.5697	-9.8722	146819	470.24	79799	350.826
26	6.5560	-9.8256	145953	472.43	74908	330.405
27	6.5422	-9.7787	144997	476.41	69218	305.760
28	6.5284	-9.7316	143947	480.27	62790	277.648
29	6.5146	-9.6843	142878	483.11	55953	247.763
30	6.5007	-9.6367	141800	484.62	49424	219.333
31	6.4867	-9.5888	140692	484.69	43317	192.858
32	6.4727	-9.5407	139600	483.38	37577	168.036
33	6.4587	-9.4924	138568	480.80	32785	147.414
34	6.4445	-9.4438	137642	477.17	29377	132.960
35	6.4303	-9.3950	136884	472.92	27288	124.447
36	6.4160	-9.3460	136319	468.85	26181	120.445
37	6.4016	-9.2967	135903	466.12	25718	119.495
38	6.3871	-9.2472	135443	465.57	25692	120.725

Node	X co-ord (cm)	Y co-ord (cm)	Pressure (Pa)	Temperature (K)	Heat Flux (W/m^2)	Heat Transfer Coefficient ($W/m^2/K$)
39	6.3726	-9.1974	134796	466.94	25939	123.437
40	6.3579	-9.1474	133853	469.05	26333	127.102
41	6.3432	-9.0971	132817	470.79	26771	131.260
42	6.3284	-9.0466	132576	471.49	27164	135.488
43	6.3135	-8.9958	133798	470.83	27460	139.505
44	6.2986	-8.9448	136857	468.69	27610	142.966
45	6.2836	-8.8935	141291	465.01	27586	145.553
46	6.2685	-8.8420	145293	459.83	27290	146.458
47	6.2533	-8.7902	148197	453.59	26587	144.602
48	6.2381	-8.7381	149770	447.46	25453	139.549
49	6.2227	-8.6858	150643	443.45	23997	131.808
50	6.2074	-8.6332	151460	442.96	22498	123.097
51	6.1919	-8.5804	152539	445.90	21321	115.725
52	6.1763	-8.5273	154121	450.98	20693	111.155
53	6.1607	-8.4739	155949	456.54	20561	109.230
54	6.1450	-8.4203	157739	461.51	20748	109.054
55	6.1292	-8.3664	159357	465.31	21207	110.396
56	6.1133	-8.3122	160753	467.73	21871	112.921
57	6.0973	-8.2578	161840	468.87	22636	116.114
58	6.0813	-8.2031	163010	469.47	23496	119.955
59	6.0651	-8.1481	164259	469.91	24418	124.296
60	6.0489	-8.0929	165607	470.60	25264	128.461
61	6.0326	-8.0373	167026	471.96	26056	132.588
62	6.0163	-7.9815	168492	474.37	26953	137.496
63	5.9998	-7.9254	169952	477.99	27972	143.301
64	5.9833	-7.8690	171404	482.69	29131	150.121
65	5.9667	-7.8124	172849	488.12	30457	158.132
66	5.9500	-7.7555	174323	493.89	31991	167.581
67	5.9332	-7.6982	175783	499.61	33798	178.859
68	5.9163	-7.6407	177262	504.93	35903	192.125
69	5.8993	-7.5830	178599	509.45	38274	207.213
70	5.8822	-7.5249	179904	513.14	40844	223.698
71	5.8650	-7.4665	181139	516.19	43579	241.238
72	5.8477	-7.4079	182270	518.66	46323	258.708
73	5.8303	-7.3490	183307	520.67	48880	274.697
74	5.8127	-7.2898	184171	522.36	51070	287.899
75	5.7951	-7.2303	184848	523.86	52801	297.632
76	5.7775	-7.1704	185259	525.31	54130	304.261
77	5.7598	-7.1103	185293	526.79	55113	308.298
78	5.7420	-7.0499	184867	528.24	55789	310.272
79	5.7243	-6.9891	183976	529.66	56244	310.958
80	5.7065	-6.9280	182603	531.07	56718	311.910
81	5.6888	-6.8666	180728	532.47	57457	314.634
82	5.6710	-6.8048	178457	533.81	58457	319.217

Node	X co-ord (cm)	Y co-ord (cm)	Pressure (Pa)	Temperature (K)	Heat Flux (W/m^2)	Heat Transfer Coefficient ($W/m^2/K$)
83	5.6530	-6.7428	175770	535.04	59575	324.983
84	5.6349	-6.6805	172711	536.08	60820	332.044
85	5.6164	-6.6179	169523	536.93	62241	340.757
86	5.5976	-6.5551	166184	537.69	63843	351.226
87	5.5783	-6.4921	162490	538.28	65617	363.517
88	5.5585	-6.4289	158207	538.46	67549	377.677
89	5.5382	-6.3655	153157	537.91	69444	392.749
90	5.5174	-6.3020	147513	536.22	70880	406.418
91	5.4962	-6.2382	141887	533.18	71670	417.568
92	5.4747	-6.1741	137664	529.37	71879	426.331
93	5.4530	-6.1098	135901	526.03	71434	431.865
94	5.4310	-6.0452	135359	523.46	70255	433.064
95	5.4090	-5.9803	134949	521.28	69135	434.052
96	5.3869	-5.9150	134485	519.24	69859	445.354
97	5.3648	-5.8494	134031	517.30	72412	466.382
98	5.3425	-5.7835	133646	515.49	75205	486.555
99	5.3201	-5.7172	133361	513.87	77616	501.433
100	5.2976	-5.6506	133169	512.48	79582	510.524
101	5.2749	-5.5837	133045	511.36	80901	512.954
102	5.2519	-5.5165	132970	510.50	81563	509.477
103	5.2287	-5.4490	132936	509.92	81636	501.518
104	5.2052	-5.3813	132944	509.63	81190	490.333
105	5.1815	-5.3132	132997	509.63	80474	478.039
106	5.1575	-5.2449	133091	509.95	79652	465.945
107	5.1333	-5.1762	133219	510.60	78878	455.117
108	5.1089	-5.1072	133371	511.64	78249	446.164
109	5.0843	-5.0379	133560	513.06	77935	439.999
110	5.0596	-4.9683	133701	514.69	77978	436.779
111	5.0347	-4.8983	133524	516.22	78365	436.309
112	5.0159	-4.8456	132595	517.17	79082	438.797
113	4.9970	-4.7928	130580	516.97	80114	443.382
114	4.9782	-4.7401	127868	515.58	81209	448.599
115	4.9593	-4.6874	125145	513.44	82424	454.666
116	4.9403	-4.6347	123091	511.26	83823	461.828
117	4.9213	-4.5820	122186	509.69	85302	469.390
118	4.9023	-4.5293	122309	509.33	86831	477.047
119	4.8832	-4.4767	121635	509.94	88352	484.343
120	4.8640	-4.4241	118196	509.62	89842	490.982
121	4.8448	-4.3715	115904	508.42	91253	496.548
122	4.8256	-4.3189	116483	508.67	92563	500.790
123	4.8063	-4.2663	112483	508.41	93752	503.535
124	4.7870	-4.2137	110135	507.96	94729	504.284
125	4.7676	-4.1612	104790	507.30	95535	503.329
126	4.7482	-4.1086	98548	506.26	96289	501.411

Node	X co-ord (cm)	Y co-ord (cm)	Pressure (Pa)	Temperature (K)	Heat Flux (W/m^2)	Heat Transfer Coefficient ($W/m^2/K$)
127	4.7287	-4.0561	90404	504.94	96968	498.555
128	4.7092	-4.0036	85447	503.91	97469	494.400
129	4.6897	-3.9511	83813	503.66	97826	489.312
130	4.6701	-3.8987	83136	504.05	98136	483.932
131	4.6505	-3.8462	82616	504.86	98516	478.955
132	4.6308	-3.7938	82080	506.01	98895	474.137
133	4.6111	-3.7414	81514	507.42	99211	469.289
134	4.5913	-3.6890	80984	509.07	99506	464.691
135	4.5715	-3.6366	80656	510.91	99832	460.629
136	4.5517	-3.5842	80726	512.88	100113	456.781
137	4.5336	-3.5365	99440	514.68	100574	454.548
138	4.5156	-3.4892	105193	515.99	101294	453.851
139	4.4977	-3.4425	110298	517.43	101998	453.427
140	4.4800	-3.3962	115306	518.89	102772	453.648
141	4.4625	-3.3504	120298	520.31	103772	455.159
142	4.4451	-3.3051	125306	521.70	104898	457.490
143	4.4278	-3.2603	130340	523.02	106071	460.262
144	4.4107	-3.2159	135351	524.28	107451	464.128
145	4.3937	-3.1719	140377	525.46	109174	469.629
146	4.3769	-3.1285	145372	526.57	111148	476.324
147	4.3601	-3.0854	150350	527.59	113255	483.674
148	4.3436	-3.0428	155285	528.53	115627	492.196
149	4.3272	-3.0007	160173	529.38	118333	502.138
150	4.3109	-2.9589	165015	530.15	121428	513.693
151	4.2947	-2.9176	169765	530.84	125274	528.328
152	4.2787	-2.8767	174308	531.45	129934	546.265
153	4.2628	-2.8363	178347	531.98	134709	564.583
154	4.2471	-2.7962	181715	532.45	139010	580.835
155	4.2314	-2.7566	189859	532.78	142866	595.160
156	4.2160	-2.7174	195121	532.78	146482	608.411
157	4.2006	-2.6785	199575	532.76	149563	619.389
158	4.1853	-2.6401	203635	532.74	152270	628.757
159	4.1702	-2.6021	207436	532.71	155255	639.191
160	4.1552	-2.5645	211049	532.69	157971	648.483
161	4.1404	-2.5272	214492	532.68	160104	655.372
162	4.1256	-2.4903	217799	532.70	162141	661.863
163	4.1110	-2.4538	220978	532.76	164286	668.803
164	4.0965	-2.4177	224025	532.87	166297	675.239
165	4.0822	-2.3820	226945	533.06	167937	680.253
166	4.0679	-2.3466	229718	533.34	169201	683.859
167	4.0538	-2.3116	232343	533.74	170040	685.876
168	4.0398	-2.2769	234786	534.26	170418	686.170
169	4.0259	-2.2426	236978	534.92	171022	687.464
170	4.0122	-2.2086	238780	535.74	172856	693.743

Node	X co-ord (cm)	Y co-ord (cm)	Pressure (Pa)	Temperature (K)	Heat Flux (W/m^2)	Heat Transfer Coefficient ($W/m^2/K$)
171	3.9985	-2.1750	239830	536.73	176006	705.338
172	3.9850	-2.1417	240785	537.95	180262	721.438
173	3.9716	-2.1088	244423	539.49	185347	741.015
174	3.9583	-2.0762	248012	541.19	191021	763.205
175	3.9451	-2.0440	251804	543.03	196902	786.633
176	3.9321	-2.0120	255696	545.00	202399	809.118
177	3.9192	-1.9804	259623	547.08	206839	828.165
178	3.9063	-1.9492	263542	549.23	208939	838.834
179	3.8936	-1.9182	267406	551.44	206913	834.044
180	3.8810	-1.8875	271195	553.68	199075	806.811
181	3.8685	-1.8572	274885	555.91	184202	751.568
182	3.8561	-1.8272	278456	558.12	164009	674.314
183	3.8438	-1.7975	281893	560.31	143351	594.059
184	3.8317	-1.7681	285194	562.44	126887	529.790
185	3.8196	-1.7390	288386	564.53	116394	489.232
186	3.8076	-1.7101	291460	566.54	110734	468.154
187	3.7957	-1.6813	294409	568.47	107852	458.341
188	3.7837	-1.6525	297234	570.31	106077	452.960
189	3.7717	-1.6237	299935	572.06	104476	448.155
190	3.7596	-1.5950	302508	573.70	102523	441.726
191	3.7476	-1.5662	304956	575.25	100114	433.221
192	3.7355	-1.5374	307280	576.69	97385	423.211
193	3.7235	-1.5086	309483	578.03	94462	412.226
194	3.7114	-1.4799	311567	579.27	91504	400.937
195	3.6993	-1.4511	313533	580.40	88627	389.844
196	3.6872	-1.4224	315386	581.42	85903	379.258
197	3.6751	-1.3936	317128	582.33	83359	369.304
198	3.6629	-1.3649	318762	583.13	80951	359.789
199	3.6508	-1.3361	320291	583.82	78620	350.459
200	3.6386	-1.3074	321719	584.40	76379	341.380
201	3.6265	-1.2787	323048	584.87	74199	332.423
202	3.6143	-1.2500	324281	585.23	72041	323.430
203	3.6021	-1.2212	325423	585.48	69960	314.648
204	3.5899	-1.1925	326475	585.63	67999	306.283
205	3.5777	-1.1638	327441	585.67	66173	298.404
206	3.5655	-1.1351	328323	585.61	64531	291.245
207	3.5532	-1.1064	329152	585.46	63110	284.976
208	3.5410	-1.0777	330027	585.17	61916	279.633
209	3.5287	-1.0490	330791	584.73	61014	275.514
210	3.5164	-1.0203	331472	584.17	60452	272.830
211	3.5042	-0.9917	332070	583.45	60225	271.565
212	3.4919	-0.9630	332585	582.58	60428	272.132
213	3.4795	-0.9343	333017	581.55	61208	275.190
214	3.4672	-0.9057	333369	580.33	62897	282.194

Node	X co-ord (cm)	Y co-ord (cm)	Pressure (Pa)	Temperature (K)	Heat Flux (W/m^2)	Heat Transfer Coefficient ($W/m^2/K$)
215	3.4549	-0.8770	333641	578.94	66242	296.439
216	3.4425	-0.8484	333838	577.34	71774	320.232
217	3.4301	-0.8198	333962	575.51	79325	352.740
218	3.4177	-0.7911	334020	573.41	88664	392.857
219	3.4053	-0.7625	334030	571.07	99798	440.580
220	3.3929	-0.7339	334008	568.58	112531	495.031
221	3.3804	-0.7053	333941	565.81	126615	555.196
222	3.3680	-0.6767	333829	562.70	140747	615.587
223	3.3555	-0.6481	333682	559.28	152566	666.240
224	3.3430	-0.6195	333512	555.51	160020	698.585
225	3.3305	-0.5909	333330	551.39	162221	708.957
226	3.3180	-0.5624	333151	546.91	159281	697.778
227	3.3054	-0.5338	332991	542.07	151636	666.652
228	3.2929	-0.5052	332867	536.90	140312	619.604
229	3.2803	-0.4767	332800	531.33	126682	562.182
230	3.2678	-0.4481	332850	525.18	112509	501.809
231	3.2552	-0.4195	332884	519.13	99449	445.665
232	3.2426	-0.3910	332884	513.81	88432	397.909
233	3.2300	-0.3624	332871	509.34	80206	362.011
234	3.2175	-0.3339	332850	505.74	77819	351.846
235	3.2049	-0.3053	332823	503.01	87054	393.583
236	3.1923	-0.2768	332793	501.06	108076	487.942
237	3.1818	-0.2504	332759	499.78	128771	580.606
238	3.1711	-0.2241	332720	499.03	139631	629.443
239	3.1603	-0.1978	332676	498.68	131573	594.034
240	3.1493	-0.1716	332626	498.58	108966	493.361
241	3.1382	-0.1454	332552	498.52	88654	402.456
242	3.1270	-0.1193	332484	498.52	93263	423.552
243	3.1156	-0.0933	332420	498.55	124372	563.937
244	3.1041	-0.0673	332357	498.59	143365	649.746
245	3.0924	-0.0414	332293	498.61	126599	574.665
246	3.0806	-0.0155	332229	498.61	111933	509.140
247	3.0687	0.0103	332164	498.61	130075	591.754
248	3.0566	0.0360	332098	498.63	139699	636.027
249	3.0444	0.0617	332029	498.70	128931	588.305
250	3.0320	0.0873	331960	498.88	126320	577.705
251	3.0195	0.1128	331920	499.36	122070	559.641
252	3.0069	0.1382	331784	499.94	111397	512.265
253	2.9941	0.1636	331619	500.30	99974	461.122
254	2.9812	0.1890	331480	500.62	87626	405.293
255	2.9682	0.2142	331354	500.87	79218	367.157
256	2.9550	0.2394	331237	501.00	75607	350.788
257	2.9417	0.2645	331126	500.95	74933	347.713
258	2.9282	0.2895	331024	500.67	75580	350.513

Node	X co-ord (cm)	Y co-ord (cm)	Pressure (Pa)	Temperature (K)	Heat Flux (W/m^2)	Heat Transfer Coefficient ($W/m^2/K$)
259	2.9146	0.3145	330933	500.14	76701	355.291
260	2.9009	0.3394	330859	499.41	77957	360.505
261	2.8871	0.3642	330875	498.69	79180	365.397
262	2.8731	0.3889	330635	497.05	80342	369.841
263	2.8590	0.4136	330457	495.09	81469	373.983
264	2.8447	0.4382	330299	493.09	82534	377.698
265	2.8303	0.4627	330140	491.30	83567	381.135
266	2.8158	0.4871	329963	489.88	84630	384.587
267	2.8011	0.5115	329774	488.95	85772	388.281
268	2.7863	0.5357	329575	488.53	87018	392.326
269	2.7714	0.5599	329370	488.54	88416	396.951
270	2.7564	0.5840	329164	488.77	90047	402.514
271	2.7412	0.6081	328956	488.96	92121	409.942
272	2.7259	0.6320	328740	488.86	101255	448.513
273	2.7085	0.6545	328514	488.20	102059	450.609
274	2.6907	0.6766	328276	486.83	93568	411.956
275	2.6725	0.6985	328031	484.65	91967	403.685
276	2.6540	0.7200	327774	481.68	91844	401.887
277	2.6351	0.7413	327511	478.00	92154	401.963
278	2.6158	0.7622	327243	473.86	92499	402.188
279	2.5962	0.7827	326963	469.62	92858	402.481
280	2.5762	0.8030	326669	465.73	93205	402.731
281	2.5560	0.8229	326346	462.59	93486	402.711
282	2.5353	0.8424	325994	460.48	93770	402.722
283	2.5144	0.8616	325634	459.51	94041	402.703
284	2.4931	0.8805	325285	459.47	94292	402.622
285	2.4715	0.8989	324987	460.08	94569	402.678
286	2.4495	0.9170	324728	461.00	94843	402.752
287	2.4273	0.9348	324466	461.83	95054	402.590
288	2.4048	0.9521	324157	462.20	95271	402.484
289	2.3820	0.9691	323720	461.73	95543	402.641
290	2.3589	0.9856	323188	460.23	95806	402.793
291	2.3355	1.0018	322599	457.66	96056	402.927
292	2.3119	1.0176	322008	454.14	96307	403.096
293	2.2880	1.0330	321499	450.01	96574	403.368
294	2.2638	1.0479	321035	445.85	96867	403.783
295	2.2394	1.0625	320572	442.41	97177	404.303
296	2.2148	1.0766	320057	440.57	97508	404.941
297	2.1899	1.0903	319302	441.94	97847	405.649
298	2.1647	1.1036	318460	446.49	98216	406.509
299	2.1394	1.1165	317593	452.67	98629	407.586
300	2.1138	1.1289	316747	459.06	99077	408.840
301	2.0881	1.1409	315902	464.74	99556	410.251
302	2.0621	1.1525	315014	469.22	100085	411.901

Node	X co-ord (cm)	Y co-ord (cm)	Pressure (Pa)	Temperature (K)	Heat Flux (W/m^2)	Heat Transfer Coefficient ($W/m^2/K$)
303	2.0359	1.1636	314063	472.25	100663	413.779
304	2.0096	1.1743	313034	473.73	101287	415.871
305	1.9831	1.1845	311955	473.68	101997	418.347
306	1.9564	1.1942	310858	472.41	102915	421.695
307	1.9295	1.2035	309737	470.62	104307	427.003
308	1.9025	1.2124	308564	469.64	109055	446.031
309	1.8783	1.2195	307328	470.93	109957	449.527
310	1.8541	1.2263	305999	474.74	106453	435.183
311	1.8298	1.2327	304606	479.94	104896	428.825
312	1.8053	1.2388	303166	485.19	103979	425.091
313	1.7808	1.2446	301694	489.69	103542	423.326
314	1.7562	1.2500	300181	493.10	103442	422.940
315	1.7316	1.2551	298649	495.28	103556	423.431
316	1.7069	1.2598	297030	496.14	103803	424.466
317	1.6821	1.2642	295335	495.67	104146	425.889
318	1.6572	1.2683	293578	493.92	104571	427.649
319	1.6323	1.2720	291736	491.09	105076	429.732
320	1.6074	1.2754	289867	487.79	105617	431.958
321	1.5824	1.2784	287940	485.32	106183	434.273
322	1.5573	1.2811	285960	485.49	106791	436.751
323	1.5323	1.2835	283895	488.91	107401	439.222
324	1.5072	1.2855	281724	494.28	108040	441.792
325	1.4821	1.2871	279399	500.03	108715	444.486
326	1.4569	1.2884	276983	505.30	109379	447.111
327	1.4318	1.2894	274492	509.70	110032	449.658
328	1.4066	1.2900	271932	513.07	110690	452.189
329	1.3814	1.2903	269319	515.33	111374	454.789
330	1.3562	1.2902	266634	516.44	112061	457.355
331	1.3311	1.2898	263850	516.36	112716	459.740
332	1.3059	1.2890	260893	515.21	113369	462.060
333	1.2808	1.2879	257810	513.67	114032	464.364
334	1.2556	1.2864	254549	513.74	114705	466.640
335	1.2305	1.2846	251192	518.22	115371	468.818
336	1.2054	1.2825	247520	528.13	115986	470.715
337	1.1804	1.2800	243111	540.32	116549	472.329
338	1.1554	1.2771	238606	551.37	117076	473.715
339	1.1304	1.2740	234104	561.00	117513	474.661
340	1.1055	1.2704	229457	569.40	117750	474.718
341	1.0806	1.2666	224343	576.79	117788	473.888
342	1.0558	1.2624	218851	583.36	117843	473.031
343	1.0310	1.2578	212462	589.27	119876	479.970
344	1.0019	1.2516	204228	594.63	122110	487.413
345	0.9731	1.2449	192969	599.53	122378	486.939
346	0.9446	1.2374	105670	601.69	123040	487.958

Node	X co-ord (cm)	Y co-ord (cm)	Pressure (Pa)	Temperature (K)	Heat Flux (W/m^2)	Heat Transfer Coefficient ($W/m^2/K$)
347	0.9164	1.2294	143819	602.66	123662	488.739
348	0.8886	1.2208	159923	603.39	124213	489.170
349	0.8611	1.2116	167412	603.52	124712	489.327
350	0.8339	1.2018	169968	604.31	125189	489.337
351	0.8071	1.1915	171256	605.52	125616	489.097
352	0.7807	1.1806	169605	606.11	126028	488.748
353	0.7546	1.1692	168056	606.48	126417	488.270
354	0.7290	1.1573	166219	606.65	126776	487.641

Table B-1: Mark II NGV surface data from the aerodynamic analysis.

Hole Number	X coordinate of centroid (cm)	Y coordinate of centroid (cm)	Diameter (mm)
1	1.104	0.581	6.3
2	1.372	-0.68	6.3
3	2.231	-0.01	6.3
4	2.711	-1.628	6.3
5	3.449	-2.9845	6.3
6	4.173	-4.448	6.3
7	4.819	-5.941	6.3
8	5.408	-7.447	3.1
9	5.942	-8.842	3.1
10	6.367	-10.041	1.98

Table B-2: Mark II NGV cooling hole dimensions.

APPENDIX C

Boundary Conditions for the Aerodynamic Analysis

Hole Number	Heat Transfer Coefficient ($W/m^2/K$)	T_{cool} (K)
1	1943.67	336.39
2	1881.45	326.27
3	1893.49	332.68
4	1960.62	338.86
5	1850.77	318.95
6	1813.36	315.58
7	1871.88	326.26
8	2643.07	359.83
9	1809.89	360.89
10	3056.69	414.85

Table C-1: Boundary conditions for the Mark II NGV cooling holes.

	Total Pressure (Pa)	Total Temperature (K)	α	Mach Number
Inlet	334000	788	90	0.19
Outlet	167000			0.98

Table C-2: Boundary conditions for the main flow passage.

In table C-2, α denotes the angle of the flow with respect to the inlet of the flow passage.

APPENDIX D

Properties of ASTM 310 for the Aerodynamic and Thermal Analysis

Property	Symbol	Constant Value / Function of Temperature
Density	ρ	8000 (kg/m^3)
Specific Heat	Cp	500 (J/kgK)
Thermal Expansion Coefficient	α	$5.008E\text{-}12T^2 - 3.4142E\text{-}9T + 1.6477E\text{-}5$ (m/mK)
Young's Modulus	E	-9.5588E-2T + 2.4301E2 (GPa)
Poisson's Ratio	v	0.3

Table D-1: Properties of ASTM 310 stainless steel

Temperature (K)	Thermal Conductivity Coefficient (W/m^2K)
20	12
100	13
300	15
500	17
700	20

Table D-2: Thermal Conductivity coefficient (k) of ASTM 310 stainless steel as a function of temperature

APPENDIX E

Problem With the Trailing Edge Boundary Layer Mesh

The highly skewed elements in the boundary layer mesh can be seen in Figure E-1. The problem arose when a BL mesh was implemented on the trailing edge (TE) of the blade. Most NGV profiles have a trailing edge radius. With a curvature on the TE, applying a BL mesh creates no problems (as is the case with applying a BL mesh on the leading edge). The BL elements on the TE corners could simply not handle the sharp corners and as a result overlapped onto each other. This caused major computational errors and it was impossible to run a simulation.

One solution to this was to increase the first cell size in the BL as well as the Growth rate of the rows. Only when the first cell size was increased to 0.001 or the growth rate (GR) to 1.72, would the simulation run. This was however unacceptable as a first cell size of 0.000314 was needed to achieve the desired y^+ values at the wall, and a GR of 1.2 is the maximum that should be used for adjacent cells in order not to compromise on accuracy.

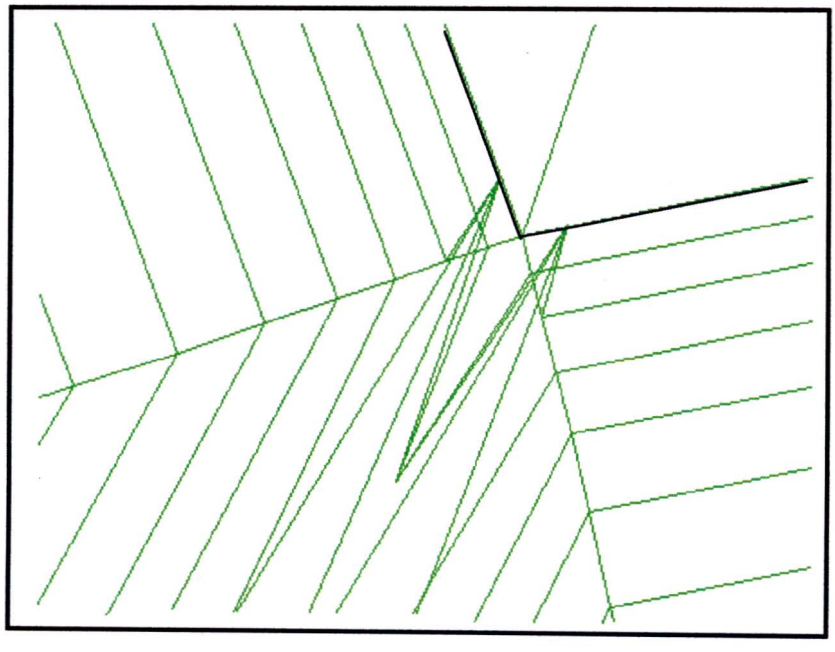

Figure E-1: Extreme close up of the highly skewed elements in the boundary layer mesh on the trailing edge

Another solution was though of, which entailed totally changing the trailing edge boundary layer mesh. By default, the boundary layer mesh in GAMBIT projects the nodes

perpendicularly from the blade surface, this is to insure perfectly orthogonal cells. It was thought to change the angle at which the BL mesh grew away from the wall, so that the mesh from either side of the TE corner could join-up, as is shown by the solution to the problem below in Figure E-2. This had to be isolated to the BL mesh at the corners only. The Angle_Smooth_Factor setting was adjusted in the default settings to allow for non-perpendicular projections. This was then restricted to the two vertices at the corners of the trailing edge.

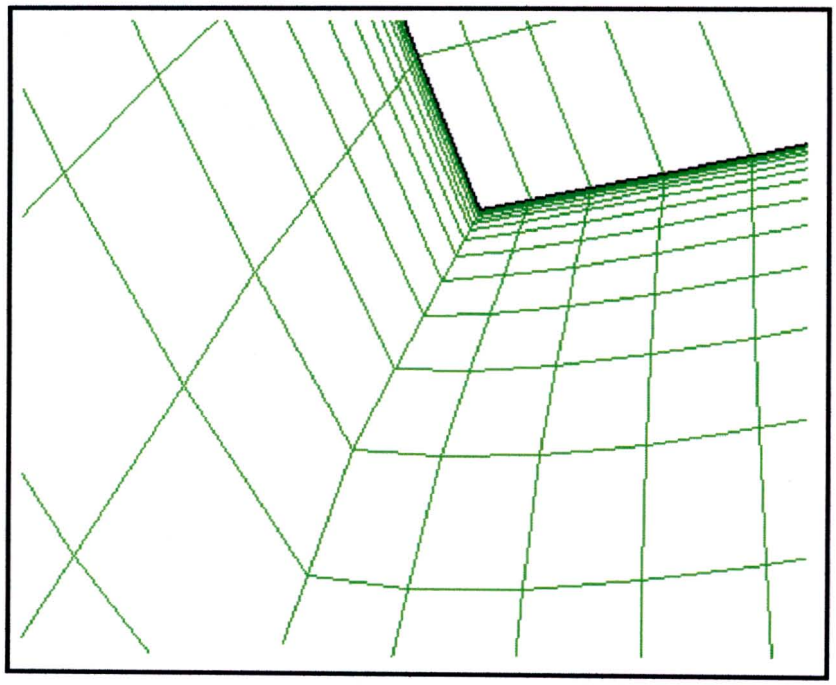

Figure E-2: The boundary layer mesh growing away non-perpendicularly from the wall

The following Journal file was written to achieve the desired result shown in Figure E-2:

```
graphics pause
undo begingroup
blayer attach "b_layer.1" face "flow" "flow" "flow" "flow" "flow" "flow" \
  "flow" "flow" "flow" "flow" edge "edge.73" "edge.72" "edge.70" "edge.66" \
  "edge.64" "edge.65" "edge.67" "edge.68" "edge.69" "edge.71"
blayer modify "b_layer.1" block
undo endgroup
graphics resume
default set "MESH.BLAYER.ANGLE_SMOOTH_FACTOR" numeric 0.9
```

```
face modify "flow" side "vertex.134"
face modify "flow" side "vertex.135"
```

Where, edges 64 to 73 are the edges that have the boundary layer attached and, vertex 134 and 135 are the vertices at the corners of the trailing edge.

APPENDIX F

CFD Contours of Static Pressure and Temperature

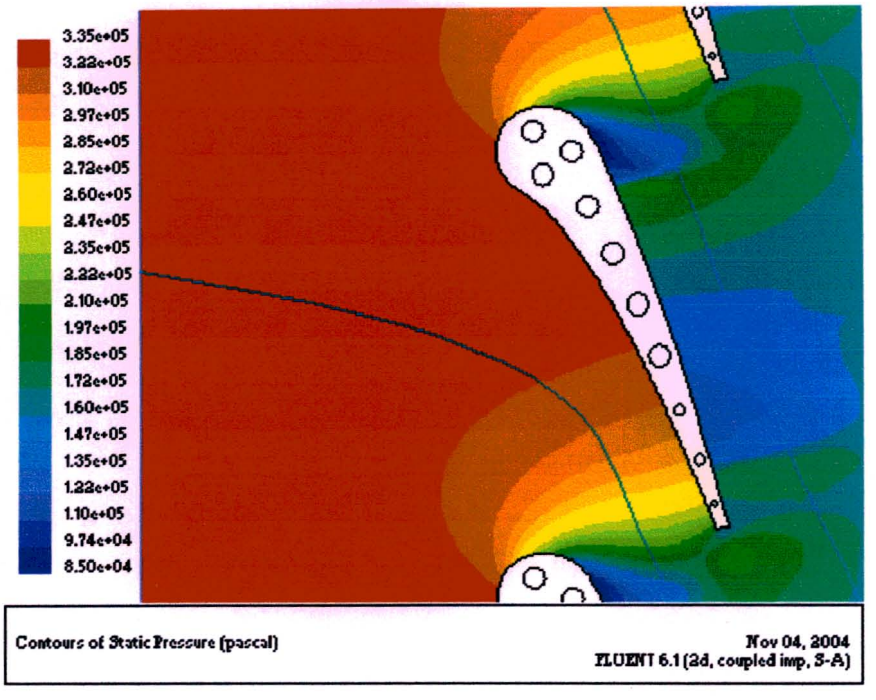

Figure F-1: Contours of static pressure for Grid 1 using the Spalart-Allmaras turbulence model without a boundary layer mesh

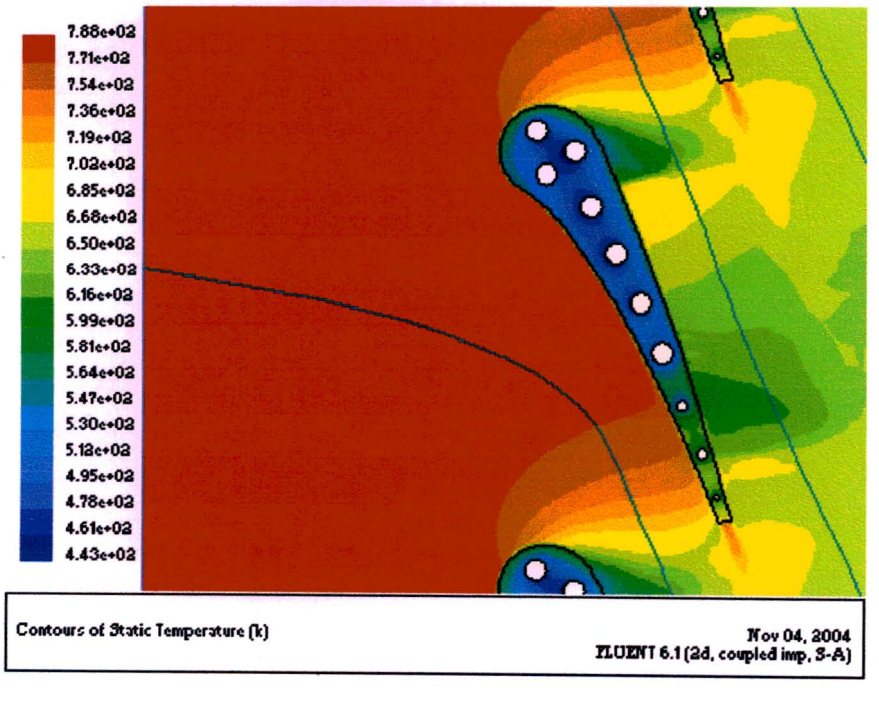

Figure F-2: Contours of static temperature for Grid 1 using the Spalart-Allmaras turbulence model without a boundary layer mesh

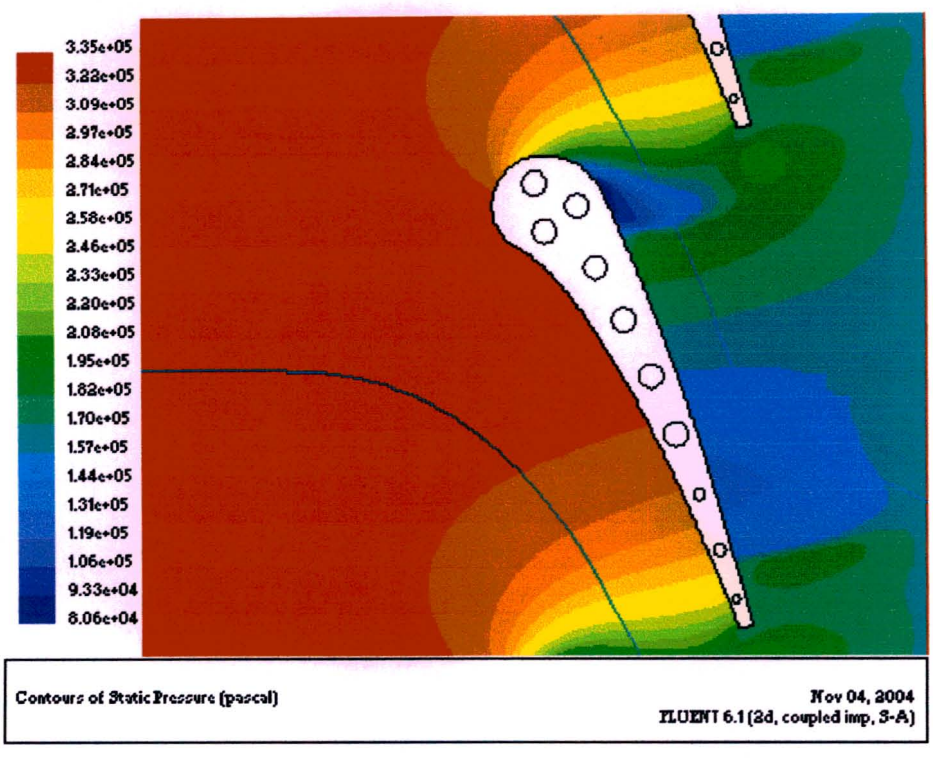

Figure F-3: Contours of static pressure for Grid 1 with a boundary layer mesh using the Spalart-Allmaras turbulence model

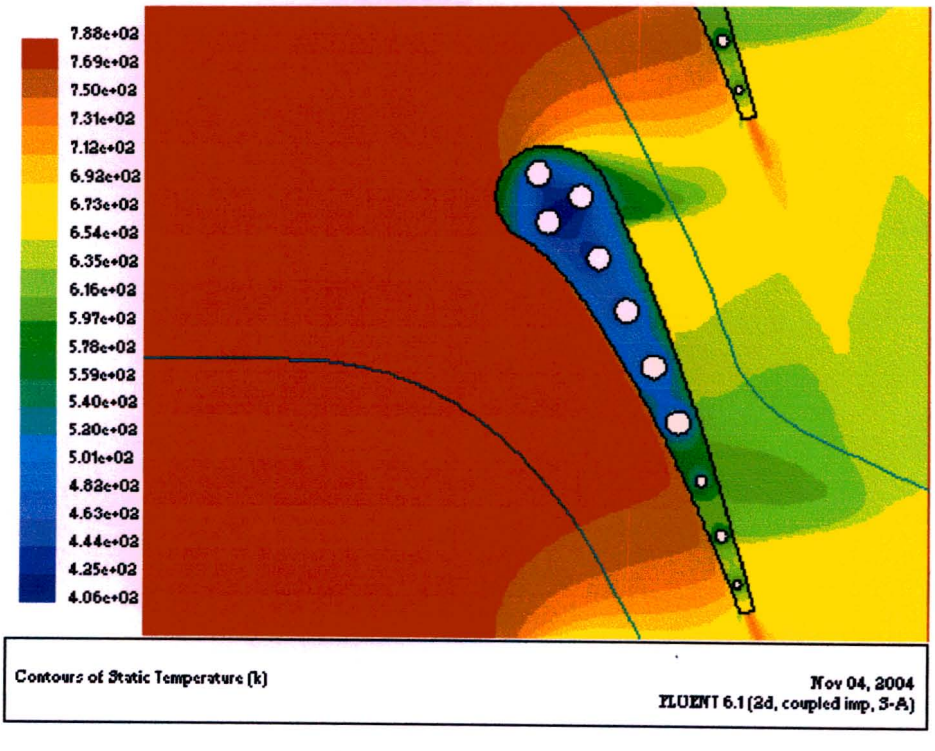

Figure F-4: Contours of static temperature for Grid 1 with a boundary layer mesh using the Spalart-Allmaras turbulence model

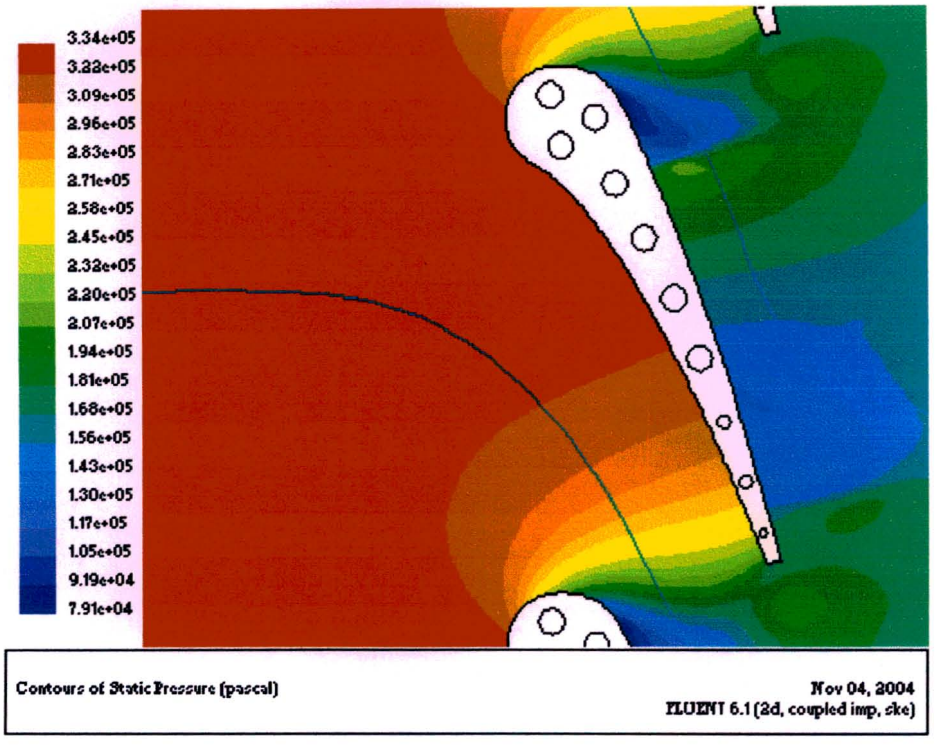

Figure F-5: Contours of static pressure for Grid 1 with a boundary layer mesh using the Standard $k - e$ turbulence model with enhanced wall treatment

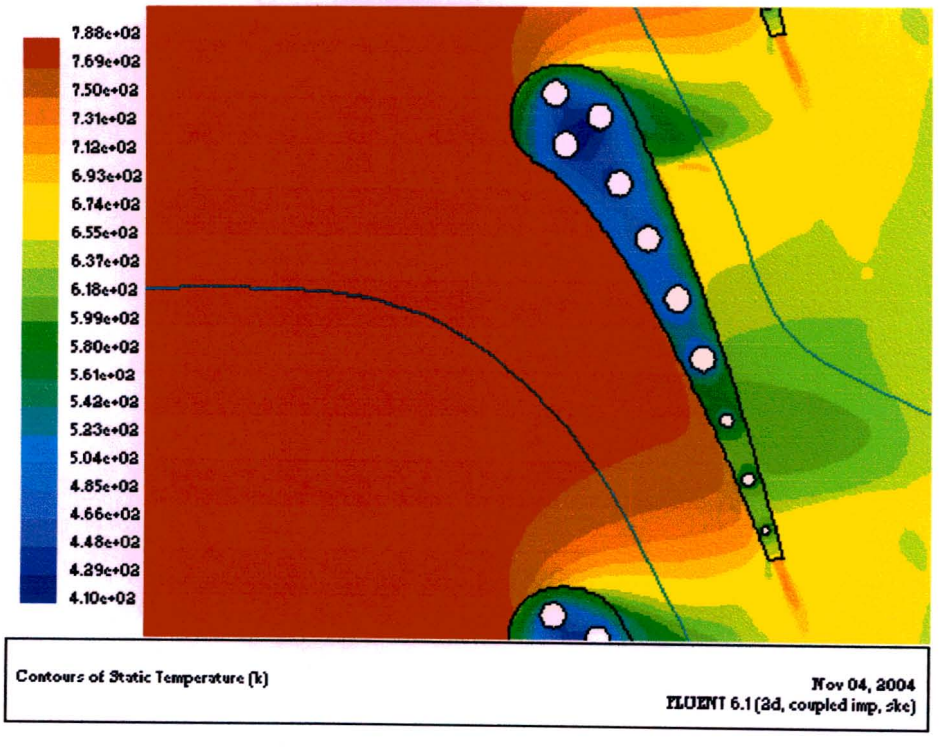

Figure F-6: Contours of static temperature for Grid 1 with a boundary layer mesh using the Standard k – e turbulence model with enhanced wall treatment

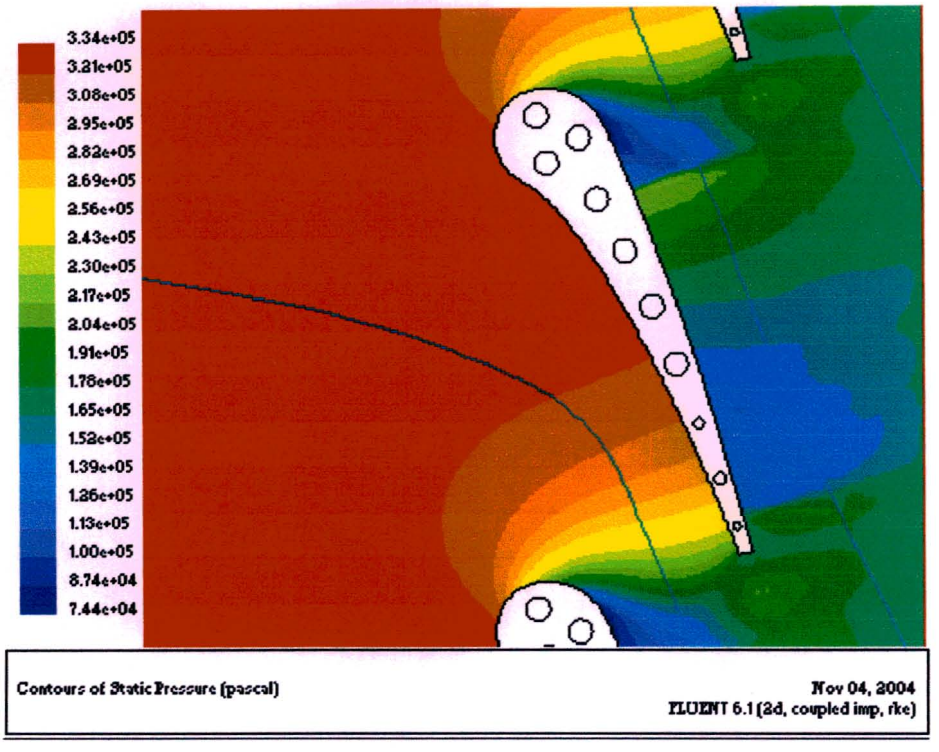

Figure F-7: Contours of static pressure for Grid 1 with a boundary layer mesh using the Realizable $k-e$ turbulence model with enhanced wall treatment

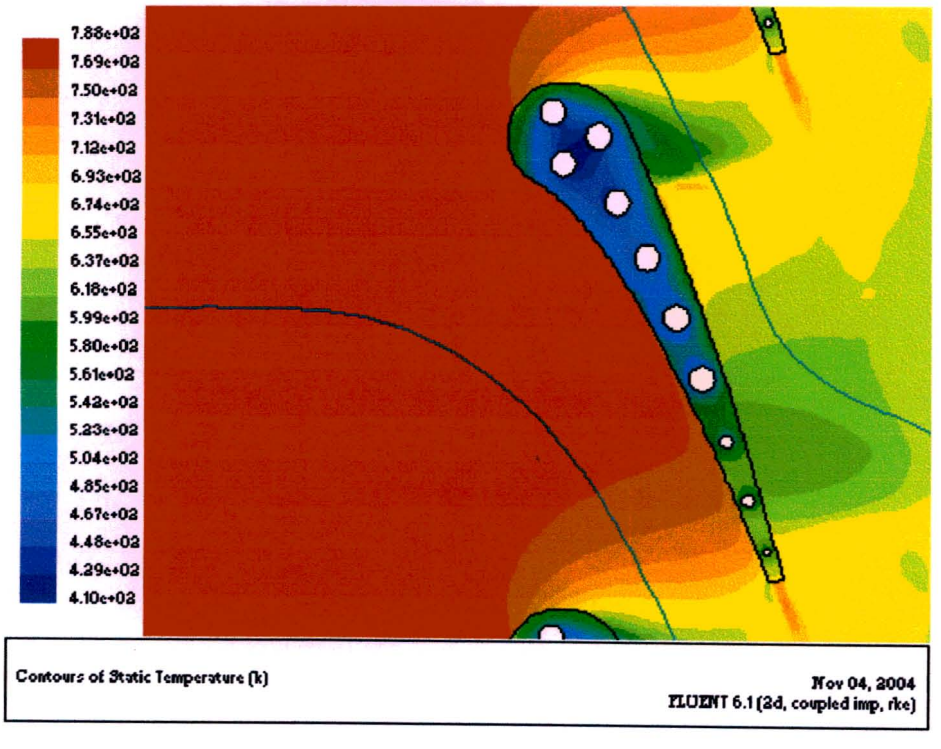

Figure F-8: Contours of static temperature for Grid 1 with a boundary layer mesh using the Realizable $k-$ e turbulence model with enhanced wall treatment

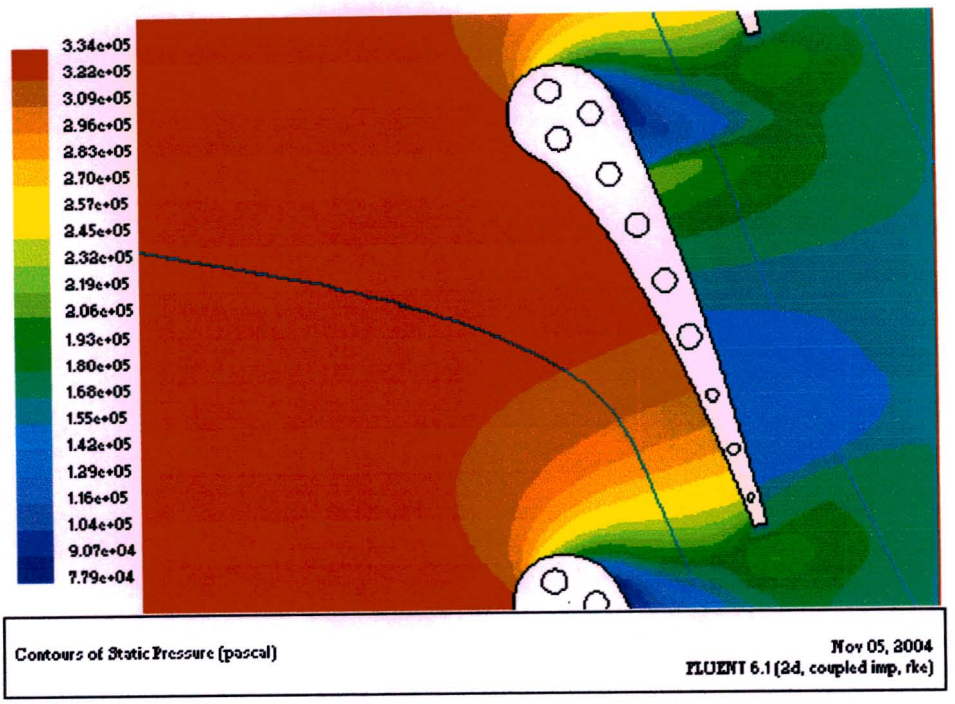

Figure F-9: Contours of static pressure for Grid 2 with a boundary layer mesh using the Realizable $k-e$ turbulence model with enhanced wall treatment

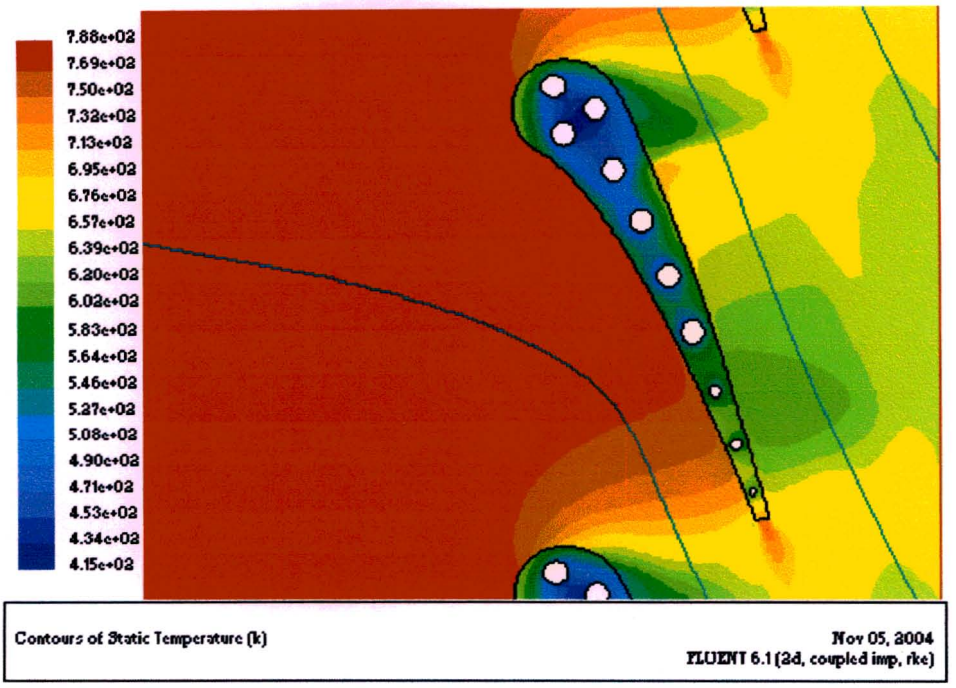

Figure F-10: Contours of static temperature for Grid 2 with a boundary layer mesh using the Realizable $k-$ e turbulence model with enhanced wall treatment

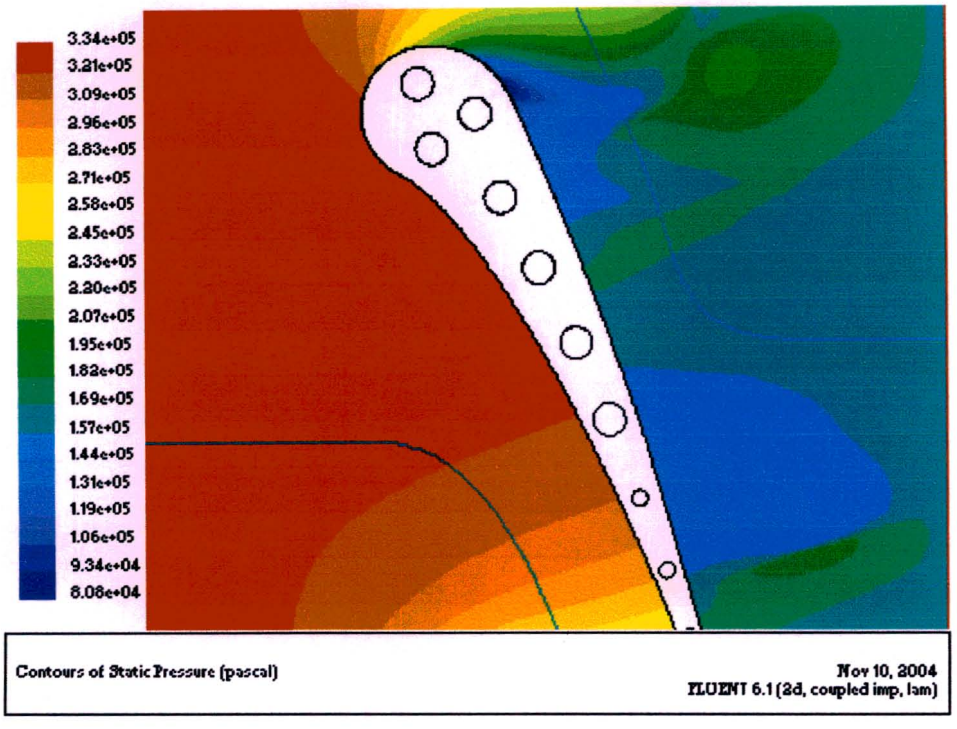

Figure F-11: Contours of static pressure for Grid 3 using the Laminar model

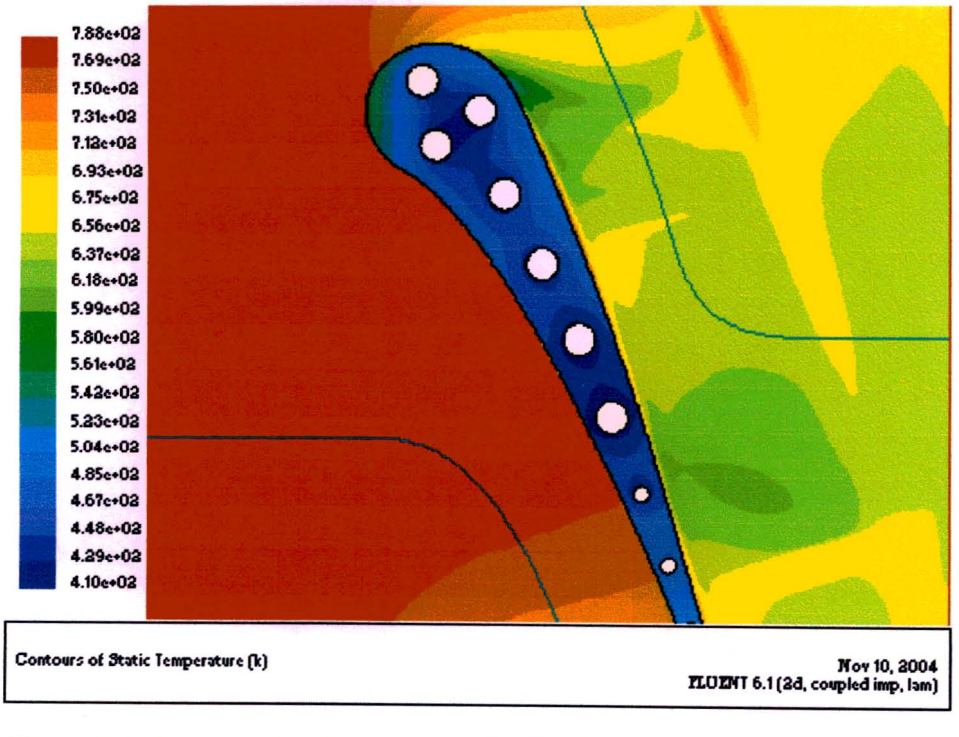

Figure F-12: Contours of static temperature for Grid 3 using the Laminar model, it can be seen that there is no shock wave present on the suction surface as the model is clearly incapable of predicting transition

APPENDIX G

Detailed Figures of the Decomposed Mesh (Grid 3)

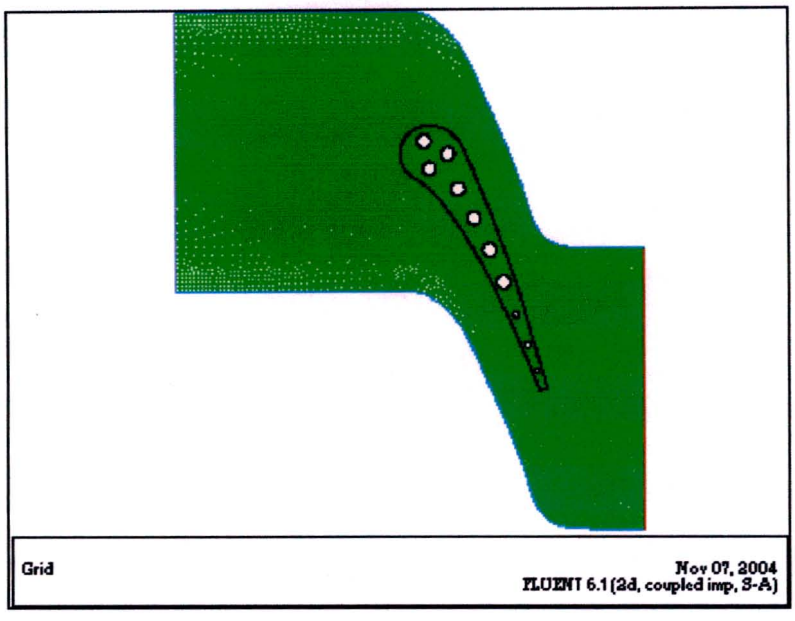

Figure G-1: The final flow field showing the solid and decomposed main flow mesh

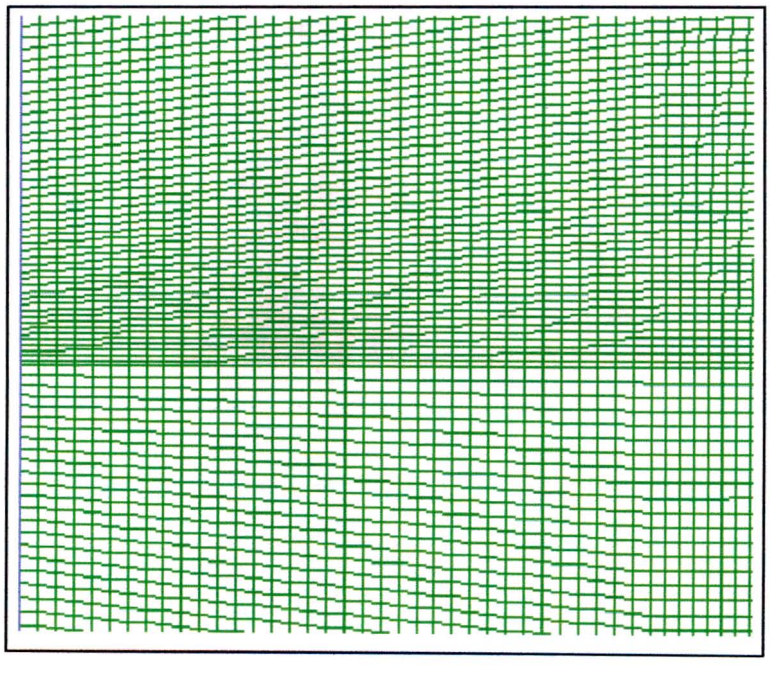

Figure G-2: Close up of the decomposed main flow mesh at the PRESSURE INLET boundary

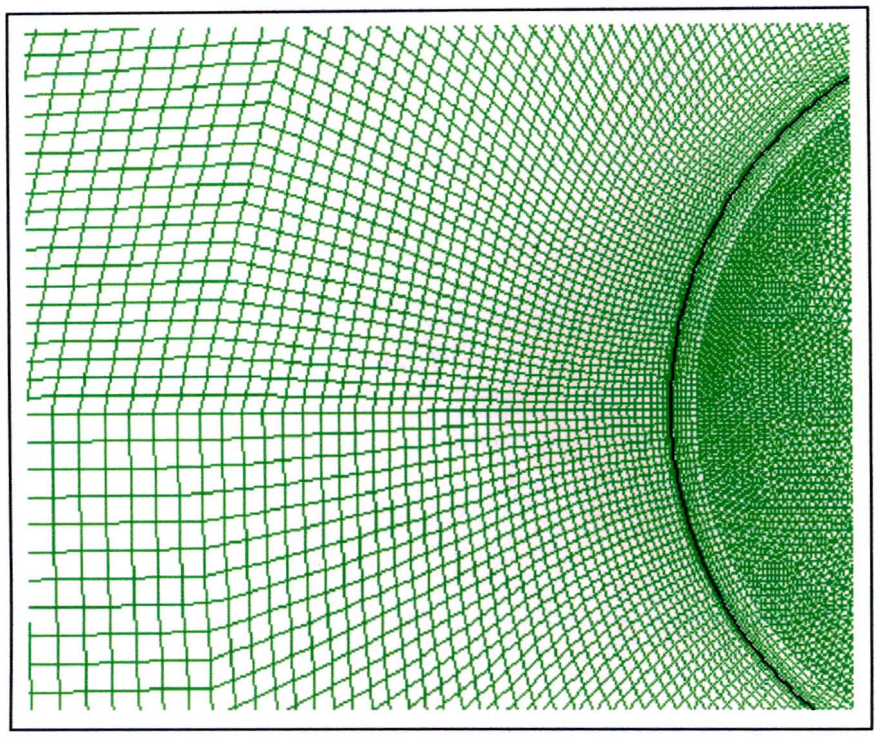

Figure G-3: Close up of the decomposed main flow mesh at the leading edge

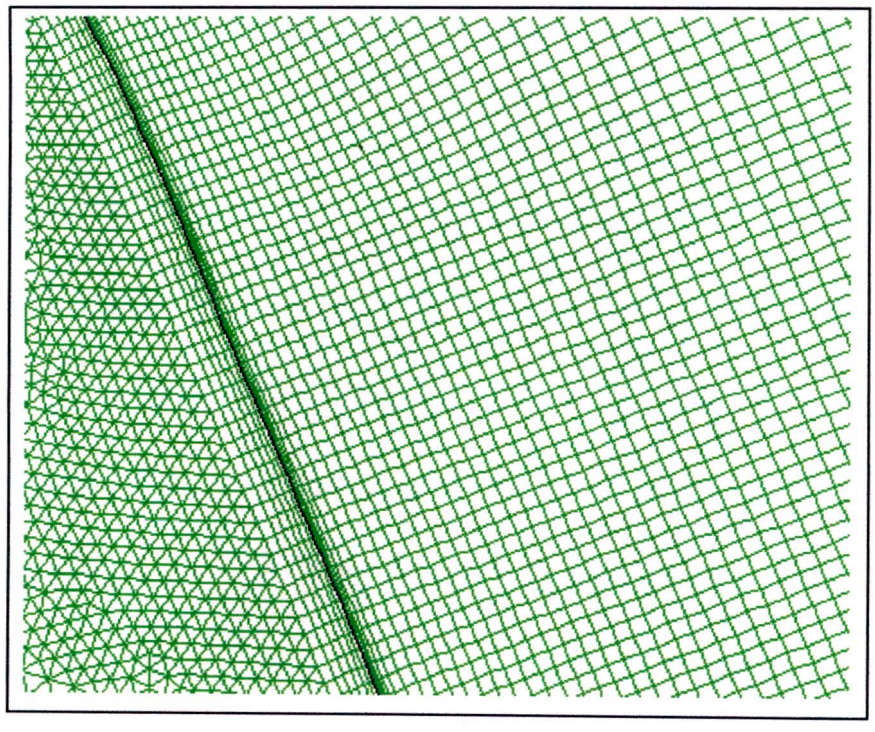

Figure G-4: Close up of the decomposed main flow mesh on the suction side, also showing the boundary layer mesh inside the blade

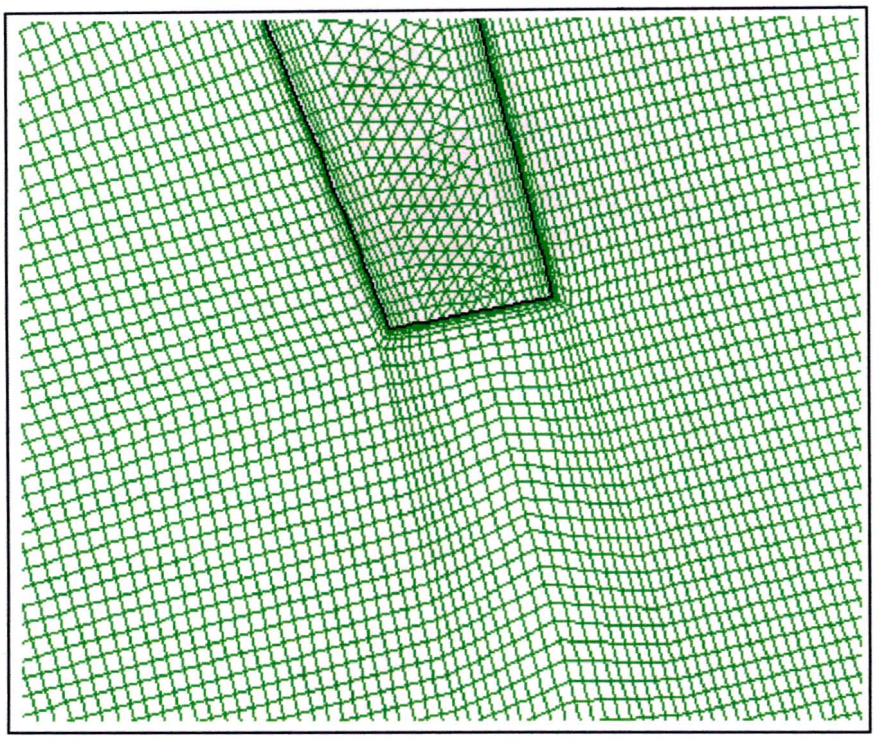

Figure G-5: Close up of the decomposed main flow mesh at the trailing edge, also showing the boundary layer mesh inside the blade

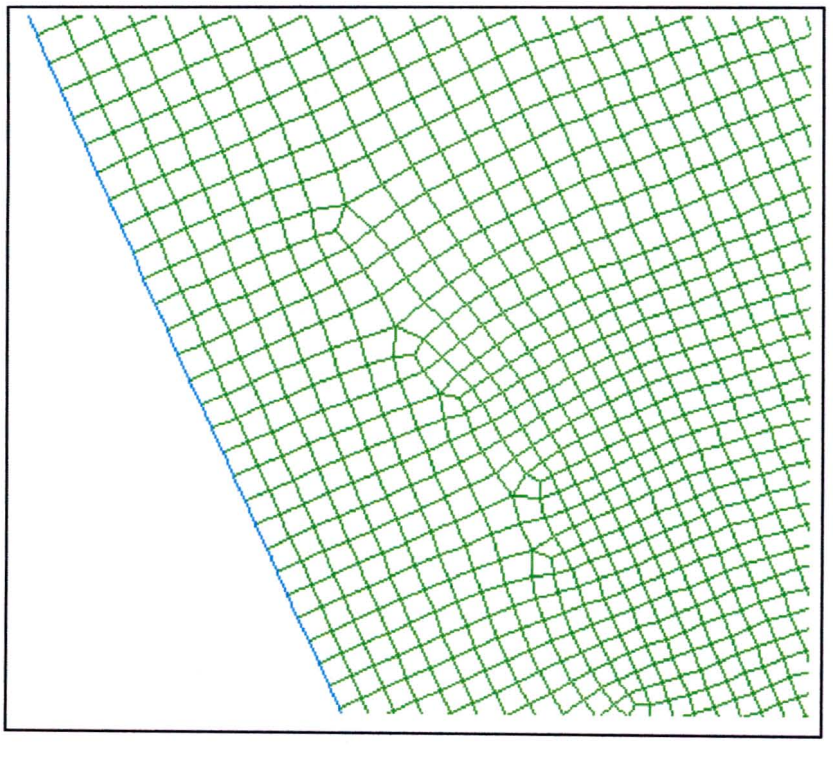

Figure G-6: Close up of the decomposed main flow mesh on the bottom PERIODIC boundary, showing the unstructured quad mesh

APPENDIX H

Flow Features Using the Decomposed Mesh (Grid 3) in Chapter 4

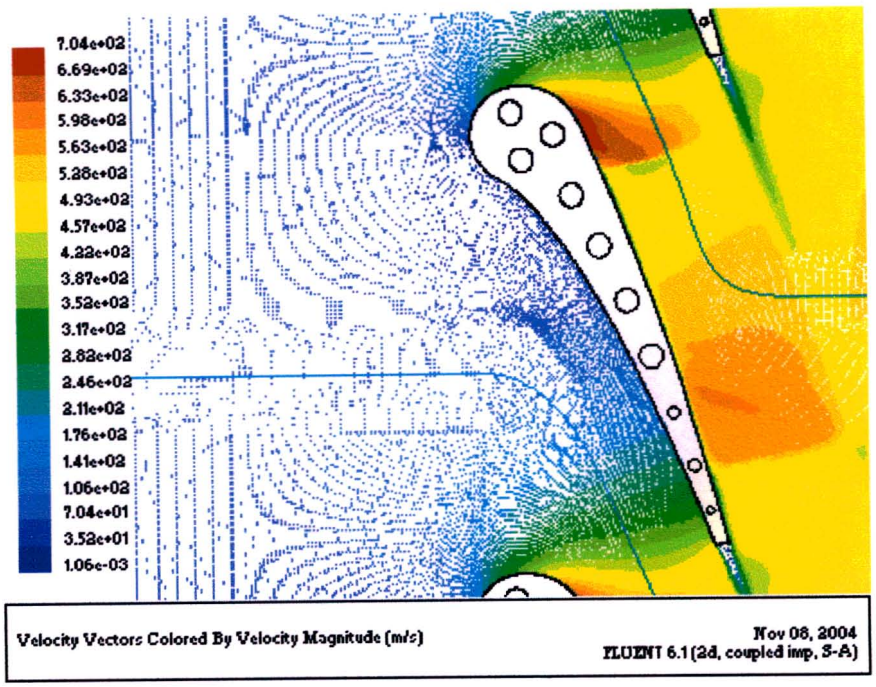

Figure H-1: Velocity vectors through the flow field

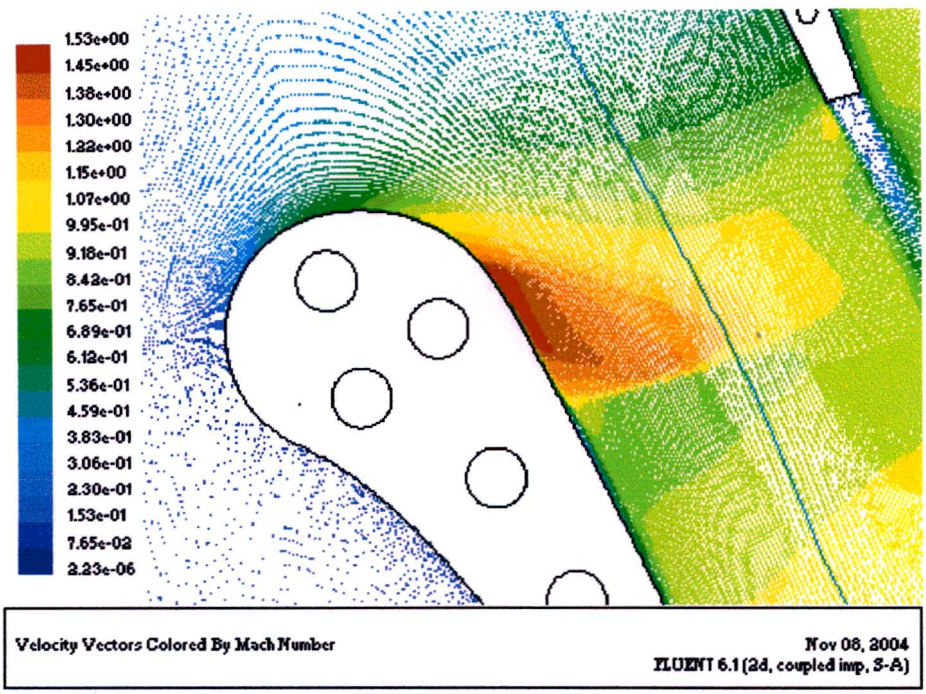

Figure H-2: Velocity vectors coloured by Mach number showing the shock wave at 44 % axial chord

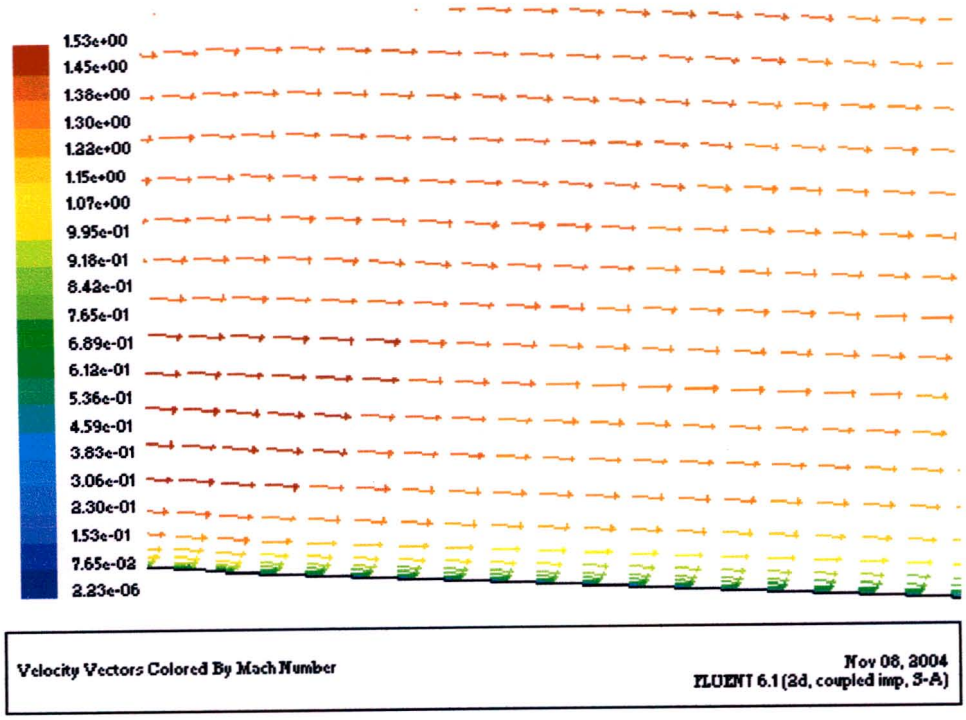

Figure H-3: Close up of the velocity vectors coloured by Mach number before the shock wave at 44 % axial chord

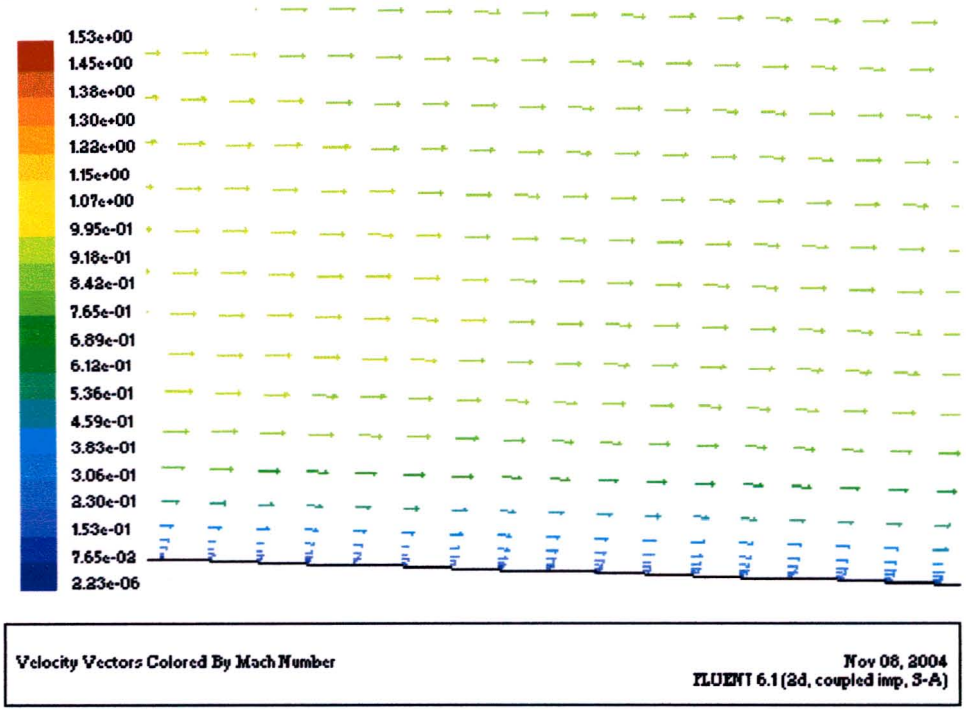

Figure H-4: Close up of the velocity vectors coloured by Mach number after the shock wave at 44 % axial chord

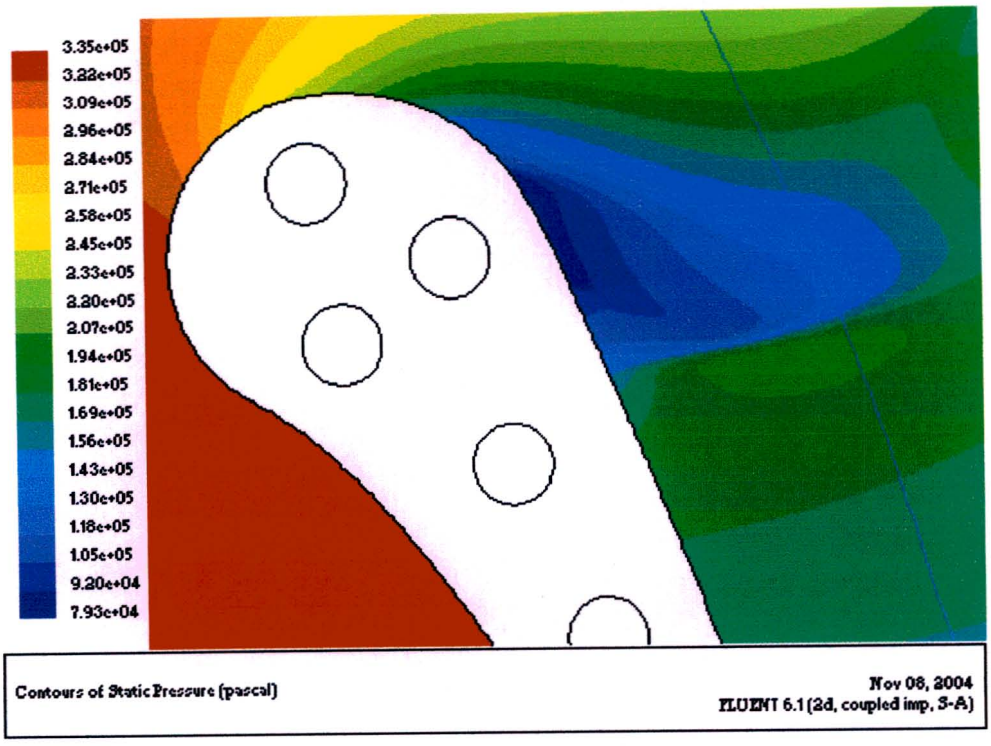

Figure H-5: Contours of static pressure showing the sharp increase in pressure at 44 % axial chord due to the shock wave

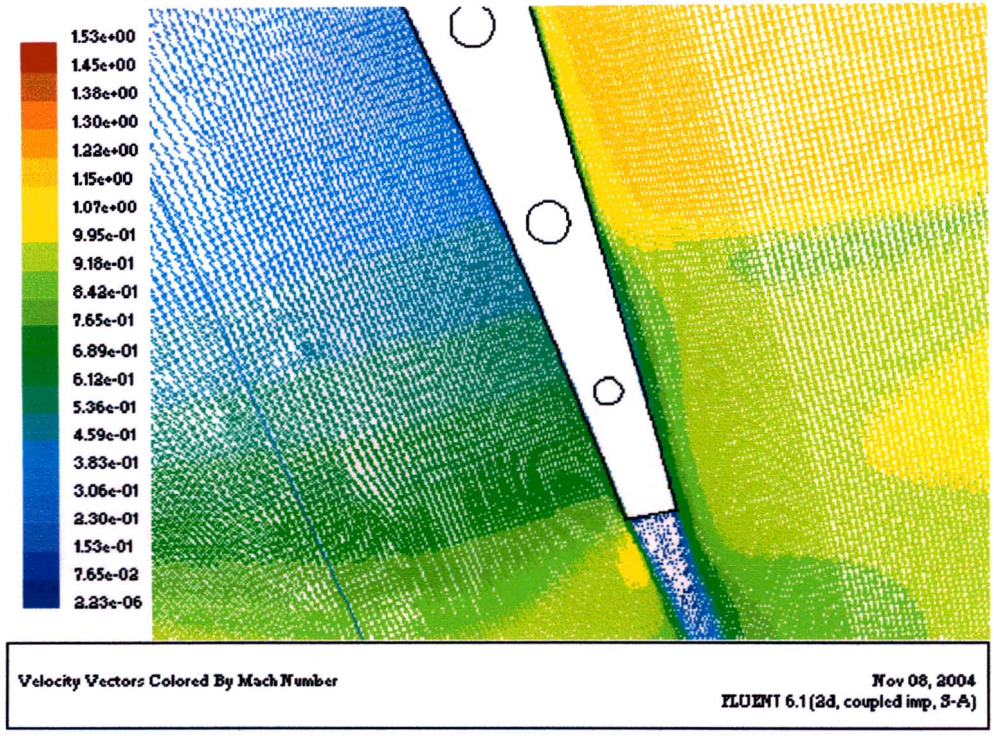

Figure H-6: Velocity vectors coloured by Mach number showing the weak shock wave on the suction side, prior to the trailing edge

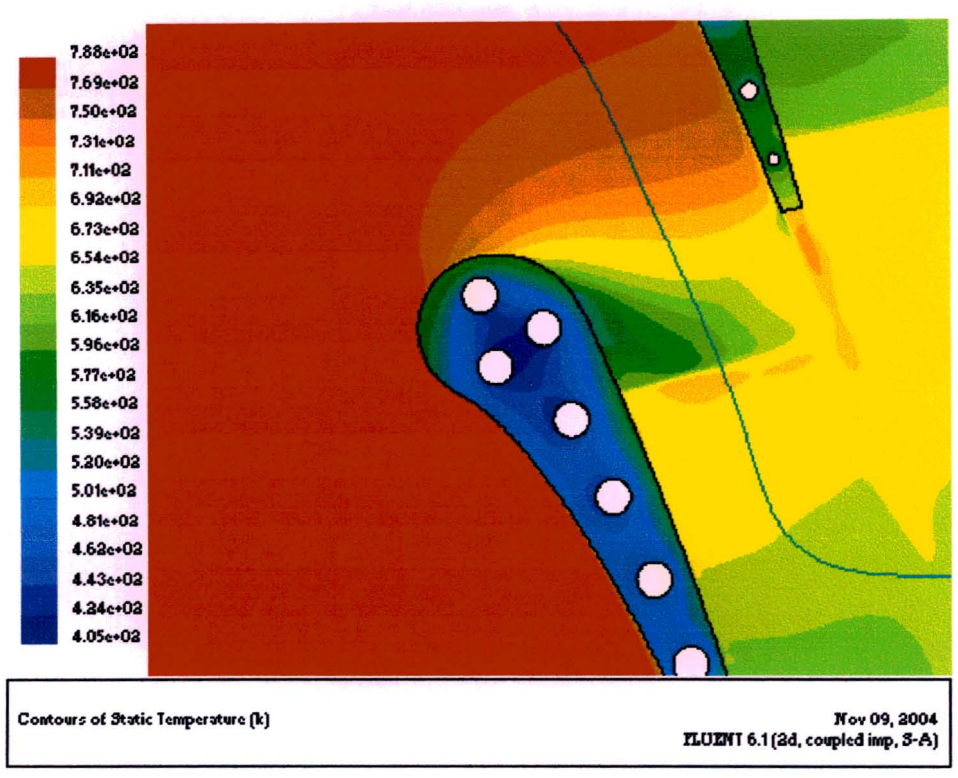

Figure H-7: Contours of static temperature showing the decrease in temperature through the flow channel.

APPENDIX I

Grid and Contour Plots for the FEM Analysis in Chapter 5

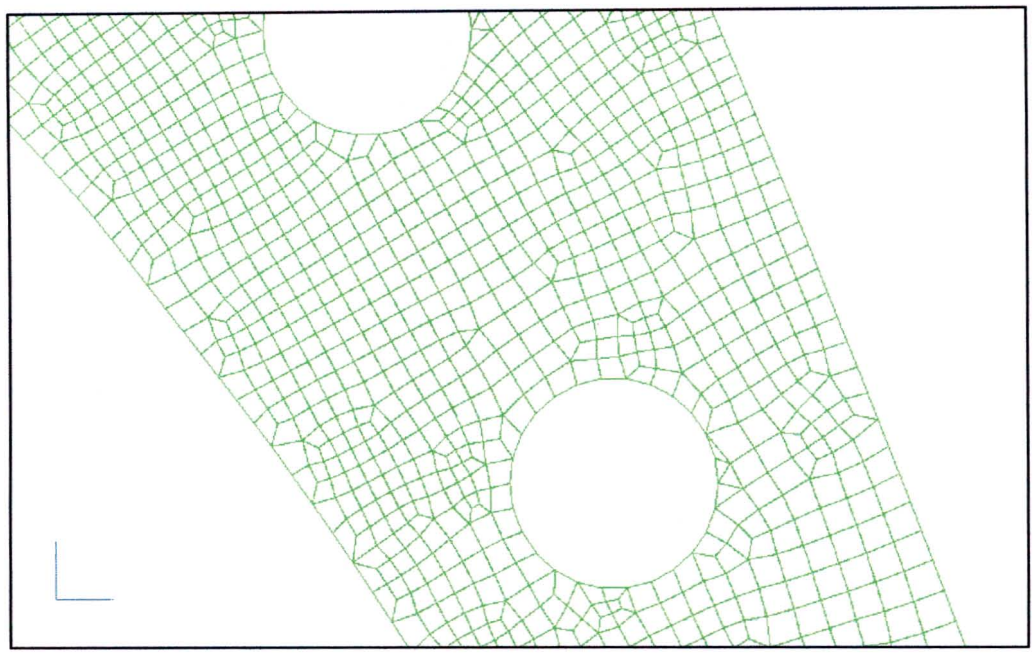

Figure I-1: Close up of Grid 2, which consists of 9674 cells in total with 354 nodes on the blade surface

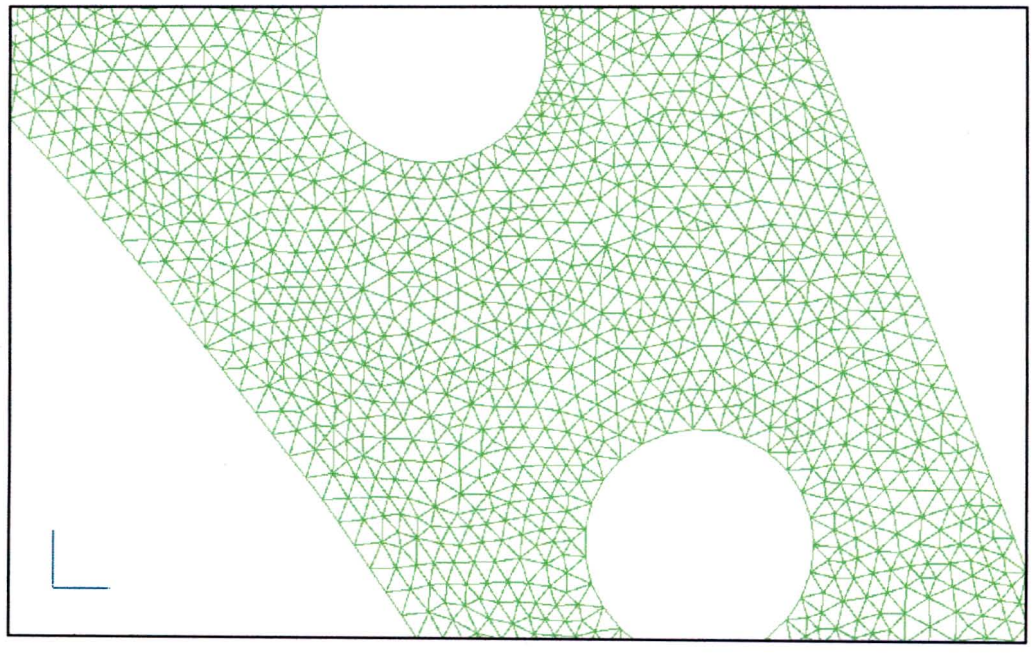

Figure I-2: Close up of Grid 3, which consists of 12248 cells in total with 354 nodes present on the blade surface

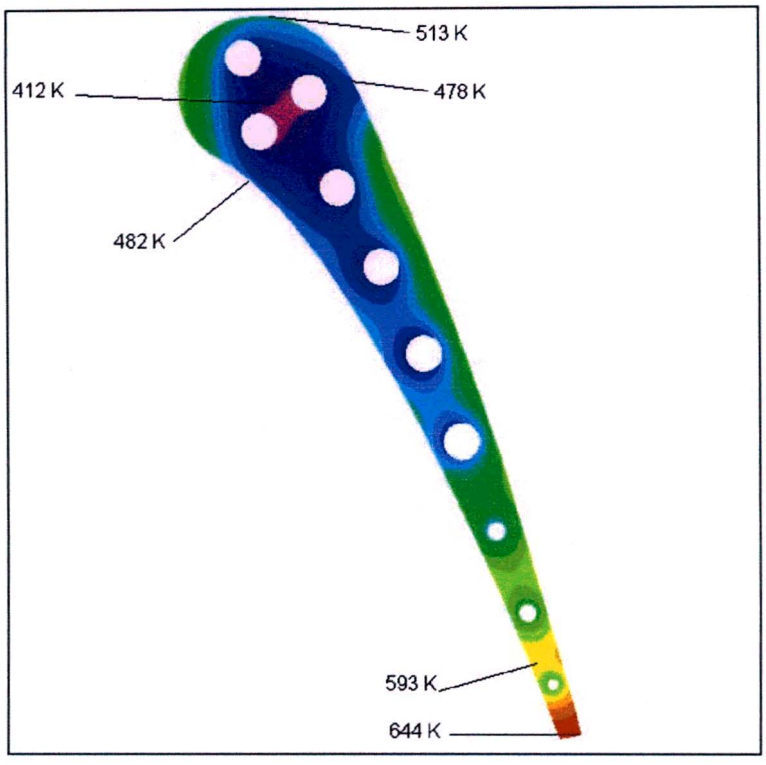

Figure I-3: Contours of temperature from the thermal analysis

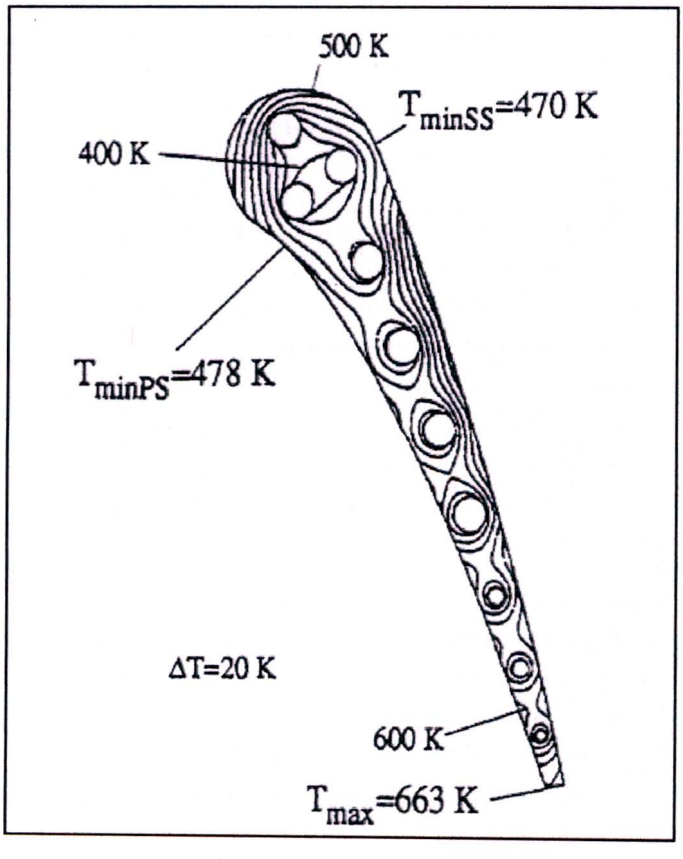

Figure I-4: Contours of temperature reproduced from Bohn et. al. (1995)

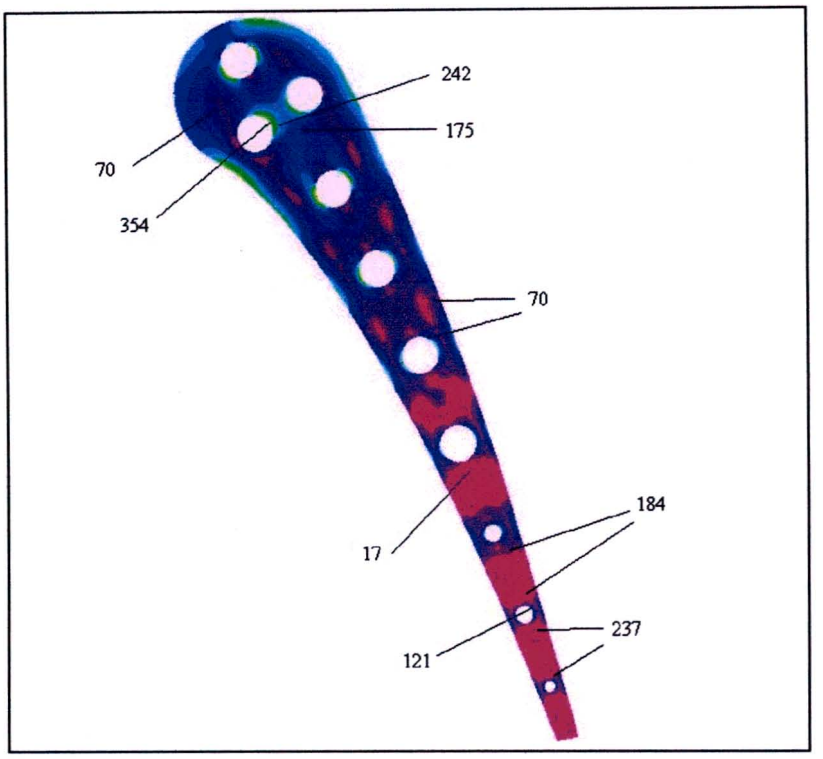

Figure I-5: Contours of Von-Mises stresses from the mechanical analysis

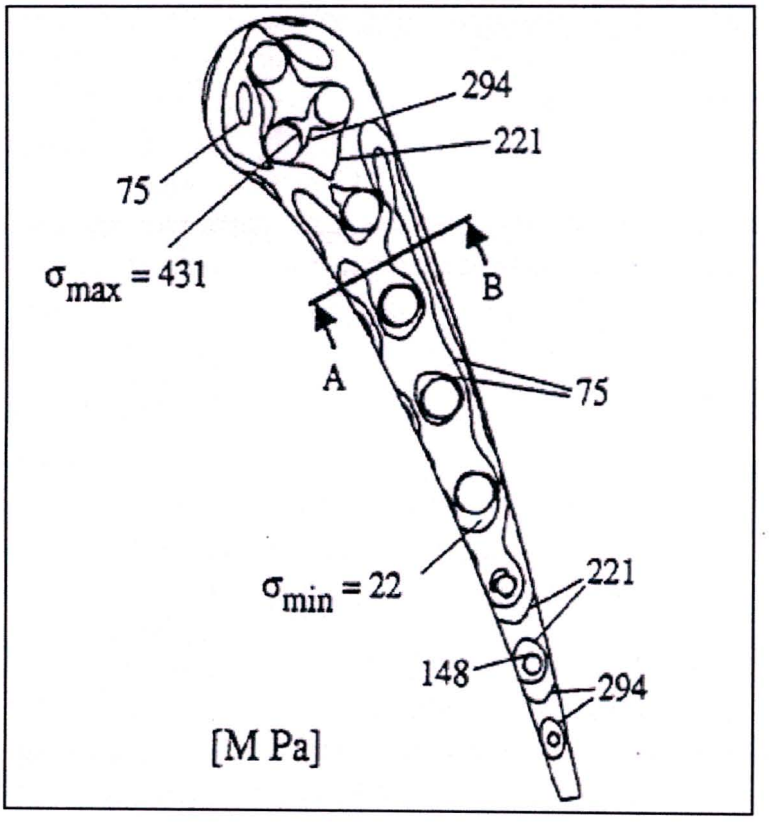

Figure I-6: Contours of Von-Mises stresses reproduced from Bohn et. al. (1995)

APPENDIX J

Temperature Boundary Profiles for the Transient Simulations in Chapter 6

Simple shock profile:

```
((simpleshock transient 3 0))
(time
0
30
60
)
(total-temperature
308.15
1200
308.15
)
)
```

Multiple shocks profile:

```
((multipleshock transient 3 1)
(time
0
30
60
)
(total-temperature
308.15
1200
308.15
)
)
```

Simplified cycle profile:

((simplecycle transient 4 0)
(time
0
638
5425
6047
)
(total-temperature
308.15
1349
1349
308.15
)
)

Multiple simplified cycles profile:

((multiplecycles transient 4 1)
(time
0
638
5425
6047
)
(total-temperature
308.15
1349
308.15
)
)

T56 mission profile:

((missionprofile transient 18 0)
(time
0
30
450
451
456
636
638
822
922
1372
2672
4427
5322
5414
5424
5439
6039
6047
)
(total-temperature
308.15
1083.15
963.15
1133.15
873.15
1349.9
1349.9
1322
1322
1283.15
923.15
1053.15
973.15

1053.15

873.15

963.15

963.15

)

)

REFERENCES

Adamczyk J. J., Aerodynamic Analysis of Multistage Turbomachinary Flows in Support of Aerodynamic Design, Journal of Turbomachinary, ASME, Vol. 122, 2000. pp 189-216.

Adamczyk J. J., Celestina M. L., Beach T. A. and Barnett M., Simulation of Three Dimensional Viscous Flow within a Multistage Turbine, Journal of Turbomachinary, ASME, Vol. 112, 1990. pp 370-376.

Blair M. F., An Experimental Study of Heat Transfer and Film Cooling on Large Scale Turbine Endwalls, Journal of Heat Transfer, ASME, November, 1974.

Bohn D., Lang G., Schronerborn H. and Bonhoff B., Determination of Thermal Stress and Strain Based on a Combined Aerodynamic and Thermal Analysis for a Turbine Nozzle Guide Vane, ASME Cogen-Turbo Power Conference, Vienna, Austria, 23-25 August 1995.

Brown A. and Burton R. C., The Effect of Free-Stream Turbulence Intensity and Velocity Distribution on Heat Transfer to Curved Surfaces, Journal of Engineering for Power, ASME, Vol. 100, 1978, pp 159-168.

Cebeci T. and Smith A. M. O., Analysis of Boundary Layers, Academic Press, 1974.

Chima R. V., Development of and Explicit Multigrid algorithm for Quasi-Three-Dimensional Flows in Turbomachinary, AIAA Paper no. 86-0032. 1986.

Crawford M. E. and Kays W. M., STAN 5 – A Program for Numerical computation of Two-Dimensional Internal and External Boundary Layer Flows, NASA CR 2742, 1974.

Daniels L. C., Film Cooling of Gas Turbine Blades, PhD Thesis, Department of Engineering Science, University of Oxford, England, 1978.

Daniels L. D. and Browne W. B., Calculation of Heat Transfer Rates to Gas Turbine Blades, International Journal of Heat and Mass Transfer, Vol. 24, no. 5, 1981, pp 871-879.

De Guire M. R., Introduction to Materials Science & Engineering, EMSE 201, 2003.

De Villiers J. E., Measurement and Numerical Validation of the Flow and Heat Transfer on a Transonic Turbine Blade, MScEng Final Report, Department of Mechanical Engineering, University of Natal, South Africa, 2002.

Dorney D. J. and Davis R. L., Navier-Stokes Analysis of Turbine Blade Heat Transfer and Performance, Journal of Turbomachinary, ASME, Vol. 114, 1992, pp 795-806.

Dunn M. G. and Stoddard F. J., Measurements of Heat Transfer Rate to a Gas Turbine Stator, Journal of Engineering for Power, ASME, Vol. 101, 1979, pp 275-280.

Dunn M. G. and Hause A., Measurement of Heat Flux and Pressure in a Turbine Stage, Journal of Engineering for Power, ASME, Vol. 104, 1982, pp 215-223

Dunn M. G., Rae W. J. and Holt J. L., Measurement and Analysis of Heat Flux Data in a Turbine Stage: Part 1 – Description of Apparatus and Data Analysis, Journal of Engineering for Power, ASME, Vol. 106, 1984, pp 229-233.

Dunn M. G., Rae W. J. and Holt J. L., Measurement and Analysis of Heat Flux Data in a Turbine Stage: Part II – Discussion of Results and Comparison with Predictions, Journal of Engineering for Power, ASME, Vol. 106, 1984, pp 234-240.

Dunn M. G., Bennet W. A., Delaney R. A. and Rao K. V., Investigation of Unsteady Flow Through a Transonic Turbine Stage: Data / Prediction Comparison for Time Averaged and Phase Resolved Pressure Data, Journal of Turbomachinary, ASME, Vol. 114, 1992, pp 91-99.

Dunn M. G., Kim J., Civinskas K. C. and Boyle R. J., Time-Averaged Heat Transfer and Pressure Measurements and Comparison with Predictions for a Two Stage Turbine, Journal of Turbomachinary, ASME, Vol. 116, 1994, pp 14-22.

Dunn M. G., Convective Heat Transfer and Aerodynamics in Axial Flow Turbines, ASME Turbo Expo, New Orleans, Louisiana, USA, 4-7 June 2001.

Ganga P. D., Thermal shock and CFD Stress Simulation for a Turbine Blade, MScEng Final Report, Department of Mechanical Engineering, University of Natal, South Africa, 2002.

Gauler R. E., Some Modifications to, and Operating Experiences with Two-Dimensional Finite Difference, Boundary Layer Code Stan 5, ASME Paper no. 81-GT-89, 1981.

Graziani R. A., Blair M. F., Taylor J. R. and Mayle R. E., An Experimental Study of Endwall and Airfoil Surface Heat Transfer in a Large Scale Blade Cascade, Journal of Engineering for Power, ASME, Vol. 102, 1980, pp 257-267.

Hah C., A Navier-Stokes Analysis of Three-Dimensional Turbulent Flows Inside Turbine Blade Rows at Design and Off Design Conditions, Journal of Engineering for Gas Turbines and Power, Vol. 106, 1984, pp 421-429.

Hodson H. P., Boundary Layer Separation Near the Leading Edge of a High-Speed Turbine Blade, Journal of Engineering for Gas Turbines and Power, Vol. 107, 1985, pp 127-134.

Hylton L. D., Milhec M. S., Turner E. R., Nealy D. A. and York R. E., Analytical and Experimental Evaluation of the Heat Transfer Distribution Over the Surfaces of Turbine Vanes, NASA CR 168015, 1983.

Incropera F.P and De Witt D.P., Fundamentals of Heat and Mass Transfer, 4th Ed., Wiley and Sons, 1996.

Ibrahim A., Combustion Turbine Failure Prediction, SE-ACE Innovations inc. Revised 6th April 2000.

Joslyn D. and Dring R., Three Dimensional Flow in an Axial Turbine: Part I – Aerodynamic Mechanisms, Journal of Turbomachinary, Vol. 114, 1992, pp 61-70.

Joslyn D. and Dring R., Three Dimensional Flow in an Axial Turbine: Part II – Profile Attenuation, Journal of Turbomachinary, Vol. 114, 1992 pp 71-78.

Kays W. M., Convective HEAT and MASS transfer, McGraw-Hill, 1966.

Lam C. K. G. and Bremhorst K., A Modified Form of the k-ε Turbulence Model for Predicting Wall Turbulence, Journal of Fluids Engineering, ASME, Vol. 103, 1981, pp 456-460.

Langston L. S., Nice M. L. and Hooper R. M., Three-Dimensional Flow within a Turbine Cascade, Journal of Fluids Engineering, ASME, Vol. 99, 1977, pp 21-28.

Maya T., Katsumata I. and Itoh M., The Study of Thermal Fatigue Life Prediction of Air-Cooled Turbine Blades, ASME paper no. 78-GT-58, 1978.

Mayle R. E., The Role of Laminar-Turbulent Transition in Gas Turbine Engines, Journal of Turbomachinary, ASME, Vol.113, 1991, pp 509-537.

Nealy D. A., Milhec M. S., Hylton L. D. and Gladden H. J., Measurements of Heat Transfer Distribution Over the Surfaces of Highly Loaded Turbine Nozzle Guide Vanes, Journal of Engineering for Power, ASME, Vol. 106, 1984, pp 149-158.

Patankar S. V., and Spalding D. B., Heat and Mass Transfer in Boundary Layers, 2nd Ed., Intertext, London, 1970.

Rai M. M., Unsteady Three-Dimensional Navier-Stokes Simulations of Turbine Rotor-Stator Interaction Including Tip Effects, AIAA Paper no. 87-2058, 1987

Rodi W. and Scheuerer G., Calculation of Heat Transfer to Convection-Cooled Turbine Blades, Journal of Engineering for Gas Turbines and Power, ASME, Vol. 107, 1985, pp 620-627.

Rao K. V. and Delaney R. A., Investigation of Unsteady Flow Through a Transonic Stage, Part I – Analysis, AIAA Paper no. 90-2408, 1990.

Singh R., Managing Gas Turbine Availability, Performance and Life Usage via Advanced Diagnostics, 44th Gas Turbine Users Association Annual Conference, Dubai, UAE, 9-14 May, 1999.

Swaminathan V.P. and Allen J.M., Surface Degradation and Cracking in Gas Turbine Blade Cooling Passages, 124th annual Meeting and Exposition, TSM, Las Vegas, Nevada, 1995.

T. Tinga, W.P.J. Visser and W.B. de Wolf., Integrated lifing analysis for gas turbine components, USAF Aircraft Structural Program Annual Conference, Texas, USA, 5-7 December 2000.

T. Tinga, W.P.J. Visser, W.B. de Wolf and M.J Broomhead., Integrated lifing analysis tool for gas turbine components, ASME Turbo Expo, Munich, Germany, 8-11 May 2000.

Turner A. B., Local Heat Transfer Measurements on a Gas Turbine Blade, Journal of Mechanical Engineering Science, Vol. 13, 1971, pp 1-12.

Wang J. H., Jen F. H. and Hartel O. E., Airfoil Heat Transfer Calculation Using a Low Reynold's Number version of a Two-Equation Turbulence Model, Journal of Engineering for Gas Turbines and Power, ASME, Vol. 107, 1985, pp 60-67.

Wilcox D. C., Turbulence Model Transition Predictions, AIAA Journal, Vol. 13, no. 2, 1975, pp 241-243.